Solar Canvas

NANOSCALE LIGHT MANAGEMENT
FOR ULTRA-THIN, SEMI-TRANSPARENT
AND COLOURFUL SOLAR CELLS

Nasim Tavakoli

Solar Canvas

Nanoscale Light Management for Ultra-thin, Semi-transparent, and Colourful Solar Cells

Ph.D. Thesis, University of Amsterdam, July 2021

Solar Canvas — Nanoscale Light Management for Ultra-thin, Semi-transparent, and Colourful Solar Cells
Nasim Tavakoli

Cover image: Designed and painted by Nasim Tavakoli.
Edited by Lukas Helmbrecht.

ISBN:978-94-92323-58-3

The work described in this thesis was performed at
AMOLF, Science Park 104, 1098 XG, Amsterdam, The Netherlands.

This work is part of the Dutch Research Council (NWO). It is also funded by LMPV program at AMOLF.

This thesis was produced on FSC® certified materials.
A digital version of this thesis can be downloaded from
http://ir.amolf.nl and https://dare.uva.nl/

Solar Canvas

Nanoscale Light Management for Ultra-thin, Semi-transparent, and Colourful Solar Cells

ACADEMISCH PROEFSCHRIFT

ter verkrijging van de graad van doctor
aan de Universiteit van Amsterdam
op gezag van de Rector Magnificus
prof. dr. ir. K.I.J. Maex
ten overstaan van een door het College voor Promoties ingestelde commissie,
in het openbaar te verdedigen in de Agnietenkapel
op donderdag 14 oktober 2021, te 10.00 uur

door Nasim Tavakoli
geboren te Tehran

Promotiecommissie

Promotor:	prof. dr. A. Polman	Universiteit van Amsterdam
Copromotor:	dr. E. Alarcón Lladó	AMOLF
Overige leden:	prof. dr. H. Zhang	Universiteit van Amsterdam
	prof. dr. W.C. Sinke	Universiteit van Amsterdam
	prof. dr. E.C. Garnett	Universiteit van Amsterdam
	prof. dr. M.A. Loi	Rijksuniversiteit Groningen
	prof. dr. A. Fontcuberta i Morral	École Polytechnique Fédérale de Lausanne

Faculteit der Natuurwetenschappen, Wiskunde en Informatica

تا در طلب گوهر کانی، کانی
تا در هوس لقمهٔ نانی، نانی
این نکتهٔ رمز اگر بدانی دانی
هر چیز که در جستن آنی، آنی

مولانا

You are a treasure, if the gems are your aim
No more than a grain, if a loaf is your claim
Recall this secret, when you play this game
Whatever you pursued- is what you became.
–Rumi

تقدیم به پدر و مادر عزیزتر از جانم

To my parents,
for always loving and supporting me.

Contents

CHAPTER 1

Introduction

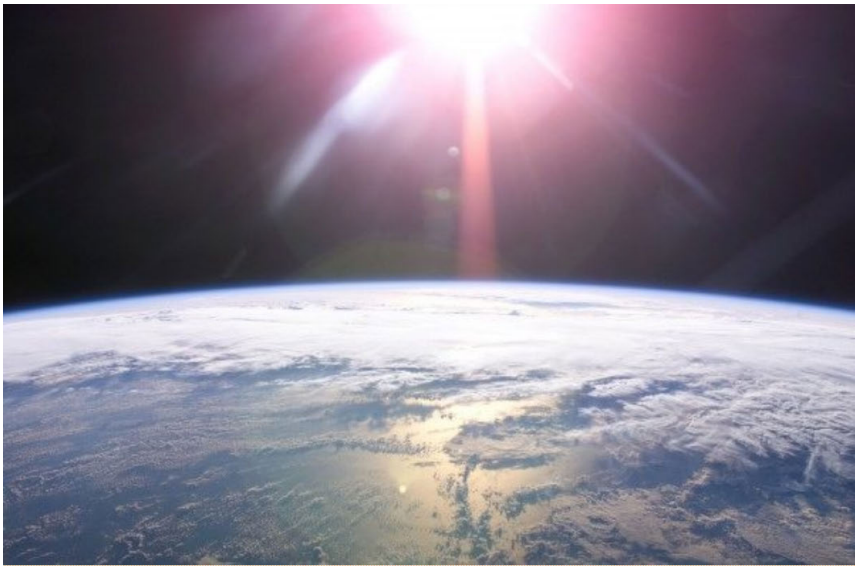

FIGURE 1.1: Earth and Sun via ISS Expedition 13 by NASA.

Despite the sun is the most abundant energy source and could be the sole supplier of our energy needs, solar -and more generally speaking, renewable- energy is still a surprisingly controversial topic. Scientists and environmentalists see it as the solution to save the world from the threat of climate change, the economists discuss the price comparison with the alternative energy sources and the politicians take their stand for or against renewables as if it is a moral choice. Prof. Bruce Usher (Columbia Business School) argues that the energy transition from fossil fuels to renewables is inevitable, and in continuation of other energy transitions in the history (from wood to coal for heat, and from animal feed to oil for transportation, see figure 1.2a). Similar to all the other energy transitions, the cost competition is the key driving force. And aside from the cost, energy transitions are

slow also due to obsolete regulations and the intrinsic uncertainty about new technologies. Regardless, Prof. Usher believes that this transition is certain and the leading countries and companies will benefit most from it [1]. On the other hand, Dr. Varun Sivaram, physicist and clean energy technology expert, believes the recent momentum in solar technology does not guarantee this transition. He describes two possible scenarios in 2050: One that renewable energy has a dramatic growth—solar, being the linchpin of this clean energy revolution- and the world is equipped to address various global challenges. In the other scenario the development of PV reaches a halt, similar to how nuclear energy—which was once a great hope for clean and cheap energy—peaked its share in global energy demand in 1990s but then declined since then. He sees innovation in solar technologies and energy systems together with innovations in financing and business models crucial for solar to reach its potential instead of hitting a ceiling [4]. What these two views —the energy transition being inevitable or still in danger of not happening— have in common is the absolute necessity of this transition from fossil fuels to renewables, especially solar, and the too slow pace of its happening at this point.

The evolution of PV installations in the past 20 years has experienced an exponential growth (figure 1.2b). In 2019, the total cumulative installed capacity of the world added up to 627 GW. China is leading with a cumulative capacity of 204.7 GW, followed by the European Union with 131.3 GW and the US with 75.9 GW [2]. In addition to the global exponential growth in PV installations, there are many impressive local examples that show the potential of clean energy playing the main role in the world's energy consumption demand. For instance, Great Britain crossed a threshold on April 21st, 2017, when the country went a day without burning any coal after four hundred years of constant use [1]. Or this year, the Australian town Onslow was fully powered by solar PV and battery for a total of 80 minutes during a successful demonstration of the Onslow Distributed Energy Resource (DER) Project [5].

However, despite the global exponential growth and impressive local examples, the current global share of solar energy in our energy consumption is still very low. Based on the theoretical calculations from the International Energy Agency for Photovoltaic Systems (IEA PVPS) less than about 6% of the electricity in Europe and less than 4% in the world comes from

photovoltaic systems (figure 1.2c). This number is even lower (less than 1%) when we also take heat and fuel needs into account [3]. In order to produce half of our energy need by PV by 2050 we need to increase our worldwide PV capacity almost 100 times. In order to get there we need our PV installed capacity to grow 14 times faster than our current fixed rate growth (see figure 1.2d). This means not only faster production of PV modules is needed but also more installations are necessary. Having said that, incorporating PV fields in homogeneously populated countries like the Netherlands can be very challenging. The area needed for 50% of the energy of the whole Netherlands to be produced by PV is 10% of the land area. This means that, in addition to solar fields, it is necessary to also incorporate solar cells into already built areas (like the roof or other facades of the buildings) or in functional spaces (like parking lots, parks, etc.). Making use of the façade area is shown to be very beneficial, especially for office buildings for which the time-frame of electricity production and consumption match very well. Based on a study at the Center for Solar Energy and Hydrogen Research Baden-Württemberg in Germany, 40% of the total energy need of a standard office building can be produced by on-site solar panels when no battery storage is installed (assuming a typical 5-floor office building in which one third of the rooftop and one fourth of the entire façade are covered with CIGS PV modules). In their study, facades alone provided 29% of the electricity consumed over a period of one year [6].

To integrate solar cells into residential areas it is important to make them more "integrable" into the buildings' architecture. Aesthetically pleasing solar cells, including semi-transparent (ST), colourful and/or flexible solar cells increase public's acceptance and inspire architects and designers to incorporate state-of-the-art PV into their designs. In the next section we take a look at some of the existing aesthetically pleasing PV solutions.

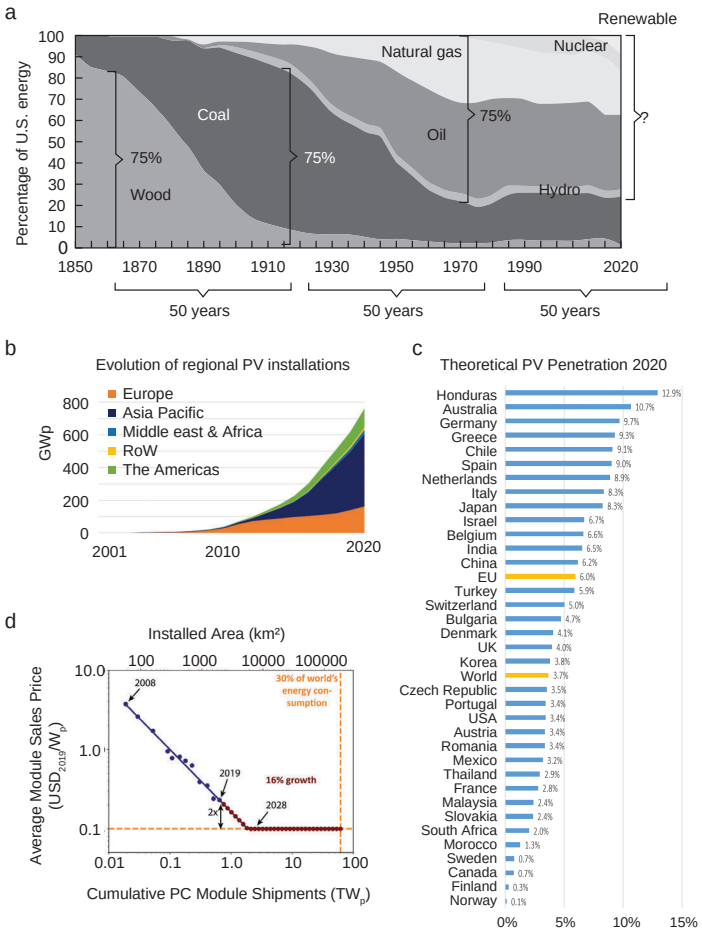

FIGURE 1.2: a) Energy transitions in the history (from wood to coal for heat, and from animal feed to oil for transportation) [1]. b)Evolution of regional PV installations from 2001 to 2020 [2]. c) Theoretical PV penetration in 2020. The theoretical electricity production from PV per country estimates what the PV production could be based on the cumulative PV capacity at the end of 2019, close to optimum siting, orientation and long-term average weather conditions [2]. d) Average sales price of Si solar modules normalized by the generated power under standardized conditions (Wp) as a function of total installed capacity since 2008. For red data points it is assumed that module prices will saturate at a price of 0.1 US$/Wp and then extrapolations of the 22% annual cost reduction at a yearly 16% growth of installed capacity is shown [3]

.

1.1 State-of-the-Art

1.1.1 Integrable Commercial PV Solutions

There are still a relatively small number of companies working on colourful and ST solar cells despite the relevance of this topic in our society, nonetheless the growth in their number is promising. The majority of the existing companies produce colourful films or glass that is added to the solar cells either during the fabrication process or later on as an add-on. Figure 1.3 shows a few examples from different projects featuring these products. There are also companies making fashionable and beautiful poly-crystalline silicon PV, organic PV, dye-sensitized solar cells, and luminescent solar concentrator solar cells (LSCs), a few examples of which are shown in figure 1.4.

1.1.2 PV and Artistic Expressions

As discussed earlier, the necessity of energy transition from fossil fuels to renewables and the current rapid growth in renewable wind and solar is not a secret. Yet most people are surprisingly unaware of what is happening in the energy sector. Bill Ritter, the former governor of Colorado, describes the source of the problem: "People have misconceptions about the cost of renewable energy largely because the public conversation about these resources has been in the form of TV campaign ads and campaign debates, where the truth is, at best, elusive." [1]. Relying on politicians' views and stands towards renewable energies to shape public knowledge and education is a big problem which can be tackled by independent approaches like collaborations between science and art. Artistic exhibitions, for instance, can form an unbiased and reliable bridge between the energy sector and the society.

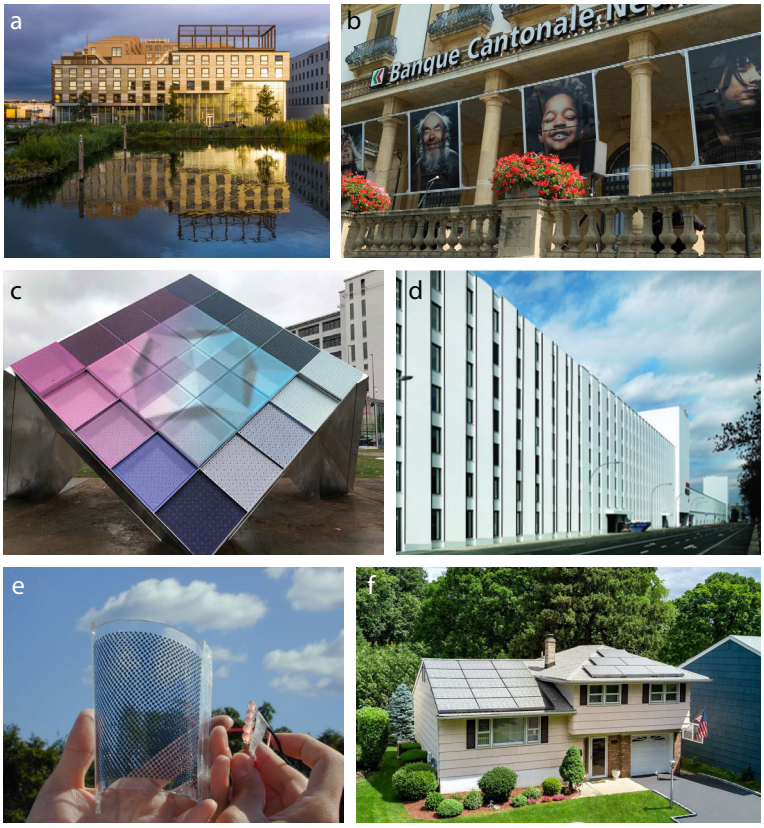

FIGURE 1.3: Coloured and/or semi-transparent solar cells by: a) SolarLab using Kromatix technology (developed by EPFL Solar Energy and Building Physics Laboratory) for the Student Experience Amsterdam Minerva, b) KALEO project by BCN and the CSEM, as a solar cell photo exhibition in the gardens of the BCN in Neuchâtel in 2017, c) Solar Visuals from UNStudio at Dutch Design Week, 2018, d) SOLAXESS white panels at Stücki-Einkaufszentrum in Basel, e) Sphelar, sphere-shaped solar cells with 1-2 mm in diameter, embedded in a transparent carrier, and f) SolarSkin by Sistine solar Bergenfield, NJ. Installed Dec 2017.
Copyright note: a) solarlab.ch b) kaleo-solar.ch c) solarvisuals.nl d) solaxess.ch e) sphelarpower.com f) sistinesolar.com

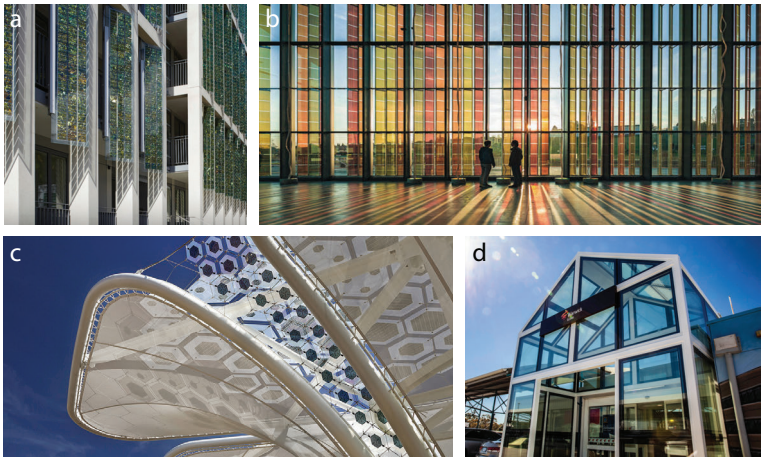

FIGURE 1.4: Colourful and/or semi-transparent Solar cells by: a) Poly-crystalline Si PV by LOF Solar in Hsinchu, Taiwan, 2014, b) Solaronix, Dye-sensitized solar cell façade at SwissTech convention center at EPFL, c) Organic PV by OPVIUS, source of image: Schmidhuber/Milla & Partner, and d) LSCs by ClearVue, Warwick Shopping Centre Atrium, Warwick WA, 2019.
Copyright note:a) lofsolar.com b) solaronix.com c) opvius.com d) clearvuepv.com

FIGURE 1.5: Pictures of two winner designs from LAGI design competition that incorporate solar technology into art [7].

Free competitions and exhibitions encourage artists and designers to come up with creative and futuristic ways of applying state-of-the-art solar technologies into their designs, and at the same time form a tribune to keep the public up-to-date about the fast-growing renewable energy sector and the cost evolution. This can greatly help bridging the information gap between the scientists and the society. One example in this field is Land Art Generator organization [7], which organizes free and open LAGI international design competition, which –as they describe- "provides an opportunity for creative minds around the world to reflect on the nature of energy infrastructures and what they can aspire to be in their built form. How can they integrate themselves into our cities in ways that enhance public space, educate, and inspire?". A couple of their winner designs from recent years are shown in figure 1.5.

1.2 Next Generation Integrable PV

Alongside with public's acceptance of new technologies, as argued previously, cost is one of the key driving factors in energy transitions. In PV technology, the mass manufacturing of the PV –alongside with the improvement in conversion efficiency as a result of research and technological progress– has reduced the cost of PV panels by consistent rate of 40% for every doubling of PV capacity. However, as discussed in [3], the cost of PV modules cannot go down to less than half of its current price. That is when the price will saturate due to other system costs that cannot be eliminated. When the cost of PV will hit this inevitable wall, the only way to further reduce the cost of PV per produced energy would be increasing the conversion efficiency. This shows the undeniable importance of minimizing the compromise of high conversion efficiency for aesthetics in solar cells, which is the motivation behind this thesis.

As mentioned already, there are different commercial approaches to tackle the integration and aesthetics of the solar cells, and in all of them there is a trade-off between conversion efficiency, aesthetics, mechanical flexibility and durability. That is why there is plenty of research devoted to achieve high efficiency colourful and ST solar cells. Coloured and/or semi-transparent PV (ST-PV) can be designed using different approaches.

In order to compare their performance and appearance there are some standard figures of merit, which are listed below:

The standard figures of merit to compare PV performance in all types of solar cells, including ST and/or coloured are short circuit current density (J_{SC}) and power conversion efficiency (PCE). J_{SC} is the current density of a solar cell when the voltage across the cell is zero and it relates to light absorption. In other words, J_{SC} is the highest current density that can be produced in the solar cell. PCE of a solar cell is the portion of solar energy that is converted into electricity in a solar cell (the detailed definition and calculation of PCE is explained in Chapter 5). To put numbers into perspective, the record J_{SC} and PCE for Si crystalline cells are 42.65 mA/cm^2 and 26.7%, respectively [8]. Best below 20 µm film Si solar cells show J_{SC} around 34.5 mA/cm^2 and PCE of 15.4% [9]. Other thin film cells, for example GaAs or CIGS with less than 400 nm thickness have record J_{SC} (PCE) of 24.5 mA/cm^2 (19.9%) [10], and 31.1 (13.5%) [11], respectively. PCE for best commercial silicon solar cells ranges between 20 and 23% [12]. To compare the performance between different types of ST-PV devices, the transmission has to be taken into account. The figure of merit for transmission is the so-called average visible transmittance, or AVT. The AVT is the fraction of transmitted photons within the visible spectral range, normalised by the photopic response of the human eye. In this way, an opaque film will have $AVT = 0$, and a completely transparent one will have $AVT = 1$ (full details on how to calculate the AVT from a transmission spectrum in SI from Chapter 3). The AVT for quartz glass is 92% as $\sim 4\%$ of light is reflected from the front and back surfaces. Also, a typical clear double-panned insulated glass unit has AVT of near 80% [13]. A figure of merit to compare transmitted colour is perceived colour appearance in the standard illumination conditions. Calculations on colour appearance of coloured/ST solar cells can be found in the SI of Chapter 3.

After defining the important figures of merit, now we introduce different approaches on making coloured/ST PV depending on whether the reflection or transmission from the cell is broadband (non-selective) or specific for the visible light (selective). The summary of these mechanisms and methods is gathered in table 1.1.

Semi-Transparent PV				
Mechanism	**Method**	**Advantages**	**Challenges**	**Refs.**
Selective Reflection	Resonant Nanostructures on the front or back	Wide colour tunability, add-on	Sophisticated fabrication, non-Lambertian	[14]
	Non-resonant coatings	Simple fabrication, scalable, add-on	limited bandwidth control	[solaxess.ch]
	(Multi)layered coating	Simple fabrication, scalable	strong angle dependence	[15–18]
Non-selective Transmission	Segmentation	adaptable to non-flat surfaces, low cost	No colour tunability, high trade-off of PCE vs. AVT	[19]
	Thinning down active material	Flexible, simple fabrication, broad AVT range	Limited colour tunability, high trade-off of PCE vs. AVT	[20, 21]
	High bandgap materials	Transparent, industrially compatible fabrication	No colour tunability, limited theoretical PCE	[22, 23]
Selective Transmission	Organic thin films	Flexible, scalable, wide colour tunability, Low cost	Limited practical PCE, degradation	[24, 25]
	Luminescent Solar Concentrators (LSC)	Wide colour tunability, low cost	Limited practical PCE, not scalabale yet	[26–29]
	Dye-sensitized	Flexible, scalable, wide colour tunability, low cost	Limited practical PCE, degradation	[30, 31]
	Inorganic nanowires	Flexible, wide colour tunability, compatible with III-V	sophisticated fabrication, surface passivation	[32], and this work

TABLE 1.1: Different mechanisms and methods to provide semi-transparency in solar cells and some references.

Selective reflection –meaning a selected part of the visible light is reflected in order to produce the intended colour perception of the solar cell– can be implemented on both conventional opaque solar cells or on the thin ST ones. One method to provide selectivity in the reflected light can be resonant nanostructures that enhance reflection at a particular wavelength range depending on their size, and can be fabricated on the front or back side of the solar cell. These nanostructures can be designed and fabricated in different shapes and sizes which provide wide colour tunability for this method. Besides, these layers can be added on the solar cells after their production is completed which adds feasibility to their use. However, sophisticated fabrication processes and the non–Lambertian scattering nature of these nanostructures are still challenges to be addressed. Another method to provide selective reflection is by non-resonant external layers, like pigmented films, that are added on top of any kind of solar cell. Simple, cheap and scalable fabrication make them easy choices to provide colour to solar cells but the limited bandwidth control keeps them from producing pure narrow-band colours. Different kinds of coatings, either single– or multi–layered, with different thicknesses also provide colour to the solar cells underneath, although the increase in reflection and surface

damage during fabrication affect the solar cell's conversion efficiency [18]. Multi-crystalline silicon solar cells, for instance, get their colour with this technique.

Non-selective and selective transmission include all ST-PV approaches. In ST-PV, part of the visible spectrum is intentionally transmitted through, and does not contribute to the conversion efficiency. In the case of selective transmission the cell is ideally designed to absorb the ultraviolet (UV) and near–infrared (NIR) part of the sunlight and letting the visible part (or a selected part of it) pass through. By contrast the non-selective transmission type offers visible transparency by means of reducing the overall absorption in the cell [33].

Non-selective transmission, together with mechanical flexibility, can be achieved by segmentation of opaque solar cells, namely placing segments of solar cells in a flexible transparent carrier. The transparency is achieved by changing the filling fraction of the cells [19]. Another approach to achieve both transparency and mechanical flexibility is by thinning down -or lowering the concentration- of the photoactive material. In both of these cases, the colour tunability is limited and the trade-off on conversion efficiency is high. Using high band-gap materials (like ZnO or high band-gap perovskites) provides another way to achieve transparency although without any colour tunability [22, 23].

For selective transmission one of the most common technologies is making use of organic excitonic materials, where by controlling the molecular structure the absorption can be tuned to be selective for UV and/or NIR light, allowing for the visible light to pass through. Organic thin films provide flexibility, wide colour tunability and low cost. The challenges for this type of ST solar cells are the low conversion efficiency and low durability in comparison with their inorganic counterparts [24, 25]. Another method to achieve selective transmission is using Luminescent Solar Concentrators or LSCs. LSCs are based on luminophores embedded in a polymer or glass waveguide that convert the spectrum and send the concentrated light into the side-walls with attached standard PV cells. The luminophores are designed to both absorb and emit outside of the visible range. Wavelength-selective LSCs may be designed to absorb UV and emit NIR light or absorb NIR and emit deeper NIR light, offering visible

transparency and/or colour tunability at low cost. However, it is important to know that most LSCs (including wavelength-selective ones) are limited predominately by reabsorption losses that need to be reduced before these technologies are scaled to a practical module size. Dye-sensitized solar cells are another type of selective transmitting solar cells where an organic dye solution serves as light harvesting material. Similar to LSCs, wide colour tunability and low cost are advantages of this approach but low conversion efficiency and limited durability are still limiting factors of this method.

A more recent approach, which is also described in this thesis is the use of free standing inorganic nanowires (NW) for ST-PV. NW arrays embedded in flexible carriers, have the advantage of being compatible with high efficiency PV materials such as III-V semiconductors, in addition to wide colour tunability and flexibility. Similar to resonant nanostructures, however, the sophisticated fabrication is still a challenge [32]. We describe the potential of NWs for ST-PV in Chapter 3.

1.3 Outline of This Thesis

Grasping the true importance of the challenge we are facing today, to make sure the energy transition of our time will surely happen, the question that this thesis discusses is: How can we fill the gap between aesthetically desirable solar cells (colourful, semi-transparent, and flexible) and high conversion efficiency and durability, and play a role in the direction of the necessary energy transition of our century? Our approach focuses on using nanophotonic concepts in inorganic nanoscale absorbers as means to minimize this compromise.

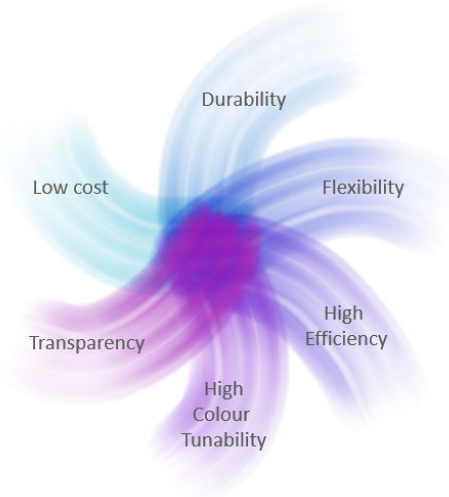

FIGURE 1.6: Intersection of various factors would lead to the ideal solar cell solution.

In **Chapter 2** , we focus on understanding the optical properties of one of the most effective nanostructures to capture, guide and efficiently absorb light: vertically standing semiconductor NWs. We study the unique light absorption properties in NWs with various aspect ratios, ranging from disk-like Mie resonator to $\sim$ 30 μm-long NWs. Using a modified Beer-Lambert law we propose a model to understand the interplay between coupling and confinement of waveguiding modes in the nature of the light absorption cross-section of NWs. An array of GaAs NWs is then characterised by means of confocal fluorescence microscopy as means to probe 3D absorption cross-section.

In **Chapter 3** we make use of these promising nanostructures to design NW-based building blocks of ST and colourful solar cells for Building-Integrated PV (BIPV). Here, we theoretically study the effect of NW arrays geometry for three common PV materials (GaAs, InP, and Si) on the perceived colour and AVT. We study the origin between the outperforming NW geometries with respect to their waveguiding properties. Moreover, we experimentally show the transmission and colour of free standing GaAs NW arrays in PDMS under different angles of illumination. This work

highlights the potential of such nanostructures as new efficient solutions for ST and colourful BIPV.

In **Chapter 4** we focus on combining flexibility and high efficiency in an ultra-thin Si cell as a different solution for integrable PV. When Si is in the order of a few microns thick, it becomes flexible but at the expense of very poor light absorption. Here we present a new family of surface texturing, based on correlated disordered hyperuniform patterns, capable of efficiently coupling the incident spectrum into the Si slab waveguiding modes. Three different texture designs are fabricated, characteristic ring-like signatures are measured in the Fourier space, and the increase in absorption is measured in an integrating sphere. Our absorption equivalent photocurrent marking far above the highest found in literature for Si of similar thickness suggests that this kind of texturing is a breakthrough toward flexible, light-weight c-Si PV.

In **Chapter 5** we combine the light waveguiding properties of NWs described in Chapter 2 and 3 with k-space engineering at the array level to increase absorption in an ultra-thin GaAs NW/Si tandem cell beyond the bulk limits. Our results show that k-space engineering is not only an effective way to design ultra-thin, high efficiency and flexible single junction solar cells (as shown in Chapter 4) but also a reliable method for optically-coupled ultra-thin tandem cells.

In summary, this thesis provides key insights into the nanophotonic designing of inorganic semiconductor nanomaterials for next generation integrable PV. We describe new concepts in semiconductor NWs and thin film slabs, with particular attention to the strong coupling of light into waveguided modes, as efficient tools to break the compromise between semi-transparency, flexibility or light-weight and light absorption.

CHAPTER 2

Understanding and Visualising Light Absorption in Semiconductor Nanowires

Owing to their intrinsic light trapping and unique absorption enhancement effect, nanowire (NW) arrays for PV applications have received a lot of attention in the recent years. Even though analytical methods are very insightful in understanding the nature of light-matter interaction in single infinite cylindrical NWs, more detailed analysis of finite element numerical simulations is necessary to study finite NWs with complex geometries. In this Chapter we focus on length-dependent absorption cross-section in NWs with various aspect ratios, ranging from disk-like Mie resonator to ~ 30 μm NWs. We distinguish a short range and a long range component in NW absorption, and inspired by the Beer-Lambert (BL) absorption formalism, we plot and fit the absorption efficiency in long NWs as a function of its length. The outstanding agreement between the fitted curve from modified BL and the simulated absorption as a function of length indicates that the modified two-term exponential BL equation is a proper model to describe the length-dependent light absorption in NWs. Moreover, we perform confocal fluorescent microscopy to provide 3D maps of light distribution around vertical GaAs NWs on a GaAs substrate. As means to resolve differences with the light extinction around the NWs for different wavelengths, we perform measurements for three excitation wavelengths at the exact same area. From off-axis y-z cut planes, for the first time, we provide direct comparison of the cone-shape of absorption shadow around the NWs at different wavelengths.

2.1 Introduction to Nanowire Solar Cells

Since early 2000's, semiconductor nanowires (NWs) were envisioned as new promising building blocks for next generation photonics and photovoltaics, with the promise of achieving efficient solar energy conversion at low cost [35–39]. Semiconductor NWs are high aspect-ratio nanostructures with lengths that can vary from a couple to tens of microns, and diameters in the range of few tens to few hundredths of nanometers. Owing to the NW cross-section being about the wavelength of light inside the semiconductor, strong light-matter interactions take place. As an example, the effective absorption cross-section in either horizontally or vertically standing NWs has been shown to be up to a couple orders of magnitude larger than the geometrical one [40–42]. In the context of solar energy conversion, the unique optical properties of vertically standing NWs combined with their capability to integrate mismatched materials (either within the NW [43, 44] or with mismatched substrates [45]) make NW arrays an exciting new platform for next generation PV, including light-weight, thin and flexible solar cells.

The typical geometry envisioned for NW-based solar cells is shown in figure 2.1, where a uniform array of vertically-standing NWs is embedded in a transparent matrix and sandwiched between two contacts. This configuration was first proposed in 1992 as a light emitting diode [56] and it was

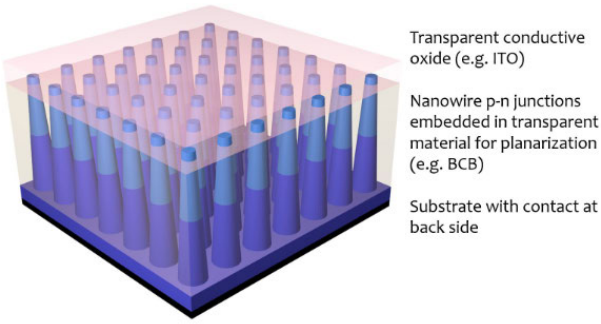

FIGURE 2.1: Typical geometry for -tapered- NW solar cell axial junction. Adapted from [34]

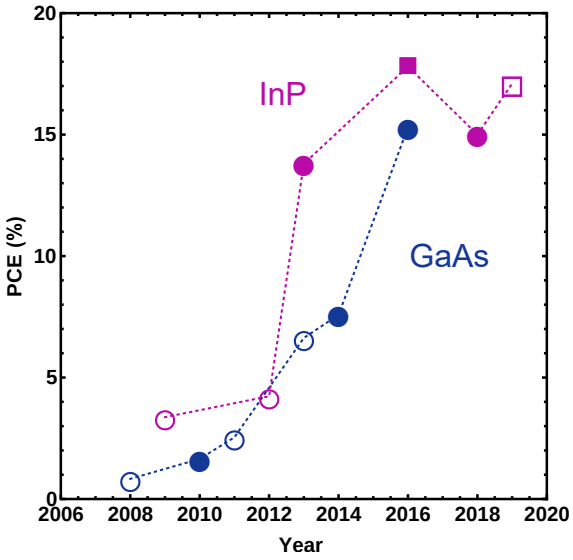

FIGURE 2.2: Evolution of GaAs (blue) [35, 46–50] and InP (magenta) [39, 51–55] NW-based solar cell efficiencies in the past years. Circles and squares represent bottom-up and top-down fabrication methods, while filled and empty representations correspond to axial and radial junctions, respectively.

later embraced as a solar cell design in 2002 [57]. The first experimental NW-based solar cell was demonstrated in 2007 out of Si with a power conversion efficiency of 0.1% [58]. Despite the low efficiency of this first device, the area of NW-PV has been rapidly growing. It was soon realised that NW-PV is mostly beneficial for the III-V semiconductor family. GaAs and InP for instance, are III-V semiconductors with direct bandgaps of 1.441 and 1.344 eV, respectively, which make them particularly interesting for solar cell applications [59]. Despite thin-film solar cells based on III-V semiconductors have shown the highest efficiencies so far, the scarcity of raw material make them too costly for terrestrial PV. Reaching similar efficiencies with less raw III-V material and on cost-effective substrates has the potential to address the cost limitations relating to III–V solar cell technology.

In the race towards high efficiency NW-PV with III-V semiconductors, the performance has increased by over 17-fold since the first GaAs NW solar cell work in 2008. Figure 2.2 shows the evolution of NW-based solar cells

based on GaAs (in blue) and InP (in magenta). Circles and squares represent two different fabrication methods: bottom-up and top-down, respectively. As seen in the figure, most NW-based record efficiency solar cells so far are made bottom-up rather than etched-down. This is particularly true for GaAs. GaAs has a much higher surface recombination velocity than InP, so this material suffers more from etching-induced surface roughening and surface passivation becomes crucial. Another feature of NW-based PV that is represented in figure 2.2 is the junction configuration. In NWs, both homo and hetero- junctions can be achieved either along the NW axis (i.e. axial junction) or across it (i.e. radial junction). Filled and empty symbols represent axial and radial junctions, respectively. It is interesting to see that most high efficiency cells are based on axial junctions even though it was long believed that radial junctions were more beneficial due to two main factors. First, the smaller distance between photocarrier generation and the p-n junction area enhances the probability of minority carrier collection. Second, the axis of light absorption and charge separation being decoupled makes independent optical and electrical optimization possible. However, in practice, controlling the doping in both the core and the shell while maintaining low defect density at the interface is a big challenge, especially for bottom-up cells. Additionally, the large junction area in radial junction cells boosts the dark current and thereby reduces the PV efficiency [55, 60, 61].

Although the general trend in efficiency enhancement of NW-based solar cells is impressive and encouraging, there is still room for improvement. Best record efficiencies for bulk GaAs and InP are 29.1% and 24.2%, respectively [62]. Besides solar cell efficiency, the NW architecture and their unique optical properties enable new concepts in tandem or semi-transparent PV [32, 63, 64], photo-detectors [65–67], lasers [68, 69] and other optoelectronic devices [70]. Fundamental studies that increase our understanding of the light interaction with the NWs hold the prospect of leading to materials' optimization and enhanced performance in NW-based opto-electronics.

In this Chapter, we describe the theoretical framework for light absorption in NWs, with the waveguiding formalism and numerical simulations. In particular, we focus on light absorption in vertical NWs and investigate

the use of confocal fluorescence microscopy as a tool to experimentally probe the absorption cross-section in NWs.

2.2 Theoretical Background: Light Interaction with Vertical NWs

When light is incident on an object of a material with a refractive index different than that of its environment, light may be scattered into different directions. Scattering means that the energy of the incident light is removed from the direction of incidence and is distributed to other directions. If the material has a non-zero imaginary refractive index for that wavelength, light may also be absorbed by the object. The extinction of light defined as the decrease of the electric field amplitude in the direction of propagation, is the result of the combined scattering and absorption. The electromagnetic field distribution inside and around any object (and thereby light extinction) can be calculated by solving Maxwell's equations and considering the relevant boundary conditions. While approximations can be used, such as Rayleigh conditions in objects smaller than the wavelength of light, solving these equations analytically is not always straightforward. Analytical solutions can be found, however, in highly symmetric systems.

For instance, Mie theory has been widely used as an analytical framework to describe light interaction in highly symmetric objects. In the case of NWs the Mie formalism has been used to consider individual, infinitely long circular cylinders as NW models surrounded by a homogeneous medium. In this case, the incident and scattered fields are expanded into cylindrical harmonics. The resulting scattering cross-section has been shown to strongly depend on the radius of the cylinder, the angle of incidence, wavelength and polarization of the incident light with respect to the cylinder high-symmetry axis. Owing to the momentum mismatch between a plane wave propagating along the NW axis and the Transverse Magnetic (TM) or Transverse Electric (TE) solutions from Mie theory, no modes are excited when the light propagates along the NW axis (i.e. vertical configuration) [71, 72]. In solar cells, however, the vertical configuration is likely the most relevant one. Thus, the Mie framework is not sufficient.

2.2.1 Waveguiding Properties in Infinite Dielectric NWs

A more complete optical description of NWs may be given by classical waveguide theory. In bulk homogeneous media there is a continuum of modes available for the light to couple to, so the light with any wavelength can travel in any direction. When the size of the medium is reduced and comparable to the wavelength of the light inside that medium the optical modes become discrete. Generally, under such conditions an object with high index contrast (e.g., a semiconductor NW in air or water) offers unusual optical phenomena such as tight optical confinement, high fractional evanescent fields, and tailorable waveguide dispersions, which create new opportunities for manipulating light on the nanoscale.

For high symmetry objects like planar slabs or infinitely long cylinders it is possible to derive analytical solutions to Maxwell's equations. For instance, the case of an infinitely long dielectric cylinder surrounded by air results in the following eigenvalue equation [73]:

$$\pm\left(\frac{1}{k_{cyl}^2}-\frac{1}{k_{air}^2}\right)^2\left(\frac{k_z m}{k_0 a}\right)^2=\left(\frac{\epsilon_{cyl}J_m'\left(k_{cyl}a\right)}{k_{cyl}J_m\left(k_{cyl}a\right)}-\frac{H_m'\left(k_{air}a\right)}{k_{air}H_m\left(k_{air}a\right)}\right)\times\left(\frac{J_m'\left(k_{cyl}a\right)}{k_{cyl}J_m\left(k_{cyl}a\right)}-\frac{H_m'\left(k_{air}a\right)}{k_{air}H_m\left(k_{air}a\right)}\right) \tag{2.1}$$

, where m is the azimuthal mode order, a is the cylinder radius, ϵ_{cyl} is the complex permittivity of the cylinder, k_0 is the free space wavevector, k_{cyl} and k_{air} are the transverse components of the wavevector inside and outside of the cylinder, respectively, k_z is the wavevector along the cylinder axis in free space and J_m and H_m are the m^{th} order Bessel and Hankel functions of the first kind, respectively. Through basic substitutions, this equation can be written in terms of k_0 and k_z, which describe the dispersion of each mode [74, 75].

The existence of leaky and guided modes is given by solutions to the equation above. Every value of the propagation constant k_z that fulfills equation 2.1 describes an eigenmode of the cylinder. All eigenmodes

can be labelled with two numbers: n, the azimuthal mode number, and l, the radial mode number, which show the number of field maxima in the azimuthal direction and in radial direction, respectively. From these solutions it follows that (infinite and cylindrical) NWs support a limited number of modes which increase in number as their radius is increased. For incidence perpendicular to the cylinder axis, ($k_z = 0$), equation 2.1 can be split into conditions for purely TM (i.e. magnetic fields in the plane normal to the cylinder axis) and purely TE modes (i.e. the electric fields normal to the NW axis)[76]. Conversely, for light incidence along the NW axis ($k_z = k_0$), hybrid HE and EH modes are also possible.

The propagation constant k_z can either be purely real or complex. The purely real values of k_z (for which $k_z > k_0\ n_{med}$) characterizes modes that are bound to the cylinder. The amplitude of the fields outside of the cylinder decays exponentially. In a non-absorbing perfect cylinder these guided modes can travel for a very long distance without any attenuation. For the complex values of k_z, however, the decay of the amplitude of the fields happens inside the cylinder and along its axis. These modes are called leaky. The decay length of these modes is defined as: $L_d = 1/2\,\mathrm{Im}(k_z)$. As an example, the dispersion relation of the eigenmodes of an infinite InP cylinder ($k_0 r$ as a function of $k_z r$) from finding the real and complex roots of equation 2.1 is shown in figure 2.3. Next to the dispersion plot, figure 2.3 shows the in-plane electric field lines of some low-order eigenmodes in a cross-section of the cylinder, which are footprints to the nature of each mode [77].

In general, when the cylinder diameter is small enough, all modes are suppressed except for the fundamental HE_{11} mode. The wavevector of this mode however is close to that in air, so that the evanescent wave outside the cylinder bounds is considerably large. At larger cylinder dimensions, additional modes are allowed with evolving leaky/guided character. Despite the infinite cylinder is a powerful approximation to describe the optical properties in free-standing semicondcutor NWs, real NWs have a limited length. The effect of limited NW length on the absorption properties of NWs is studied in the following sections. Also, real NWs likely exhibit a hexagonal cross-section rather than cylindrical (especially in the case of bottom-up grown NWs) due to crystal faceting. It has been shown however, that the field distribution and mode dispersion in cylindrical NWs of radius

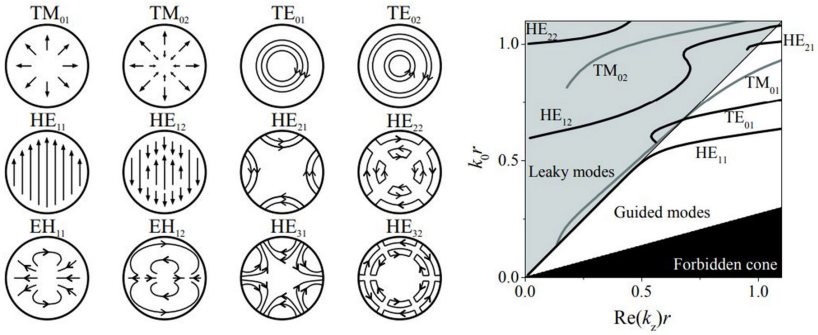

FIGURE 2.3: Left: Representation of in-plane electric field lines for lower orders eigenmodes of an infinitely long NW. Right: Dispersion relation of guided and leaky modes that can be supported in this NW. k_0 is the propagation constant in vaccum and k_z is the propagation constant in the medium. The plot shows the modes at a frequency corresponding to $\lambda_0 = 532\,\text{nm}$ and NW is assumed to be made of InP, with refractive index of 3.7. The radius of the NW is varied. We can see light cone of air in gray, light cone of InP in white, and the forbidden cone in black. Adopted from ref [77].

r is very similar to those in hexagonal NWs with same cross-sectional area (i.e. $3\sqrt{3}a_{hex}^2/2 = \pi r^2$) [73, 78].

2.2.2 Light Absorption in Vertically Standing NWs

As mentioned in section 2.1, the most relevant configuration for NW-based PV is when the radiation propagation is along the NW axis (i.e. k_z=k_0, or vertical NW conditions), as it allows for the parallel and homogeneous connection of ensembles of NW devices. So far, we have described how to understand light-matter interactions in a single infinite cylindrical NW surrounded by a homogeneous medium by using waveguiding theory. However, in reality NWs are neither infinite nor free-standing in air. Thus, while analytical methods are very insightful in understanding the nature of light-matter interaction, finite element numerical simulations are more appropriate to study complex geometries. In this thesis, we have used 3D Maxwell numerical solvers to simulate and investigate the optical proper-

ties of nano-objects and ensambles. Finite-difference time-domain (FDTD) Lumerical or Meep solvers have been used throughout this thesis.

Figure 2.4 shows an example of an FDTD simulated absorption spectrum of a 2 μm-long GaAs NW (dashed curve) [79]. The NW is 126 nm in diameter and surrounded by water ($n_{water} = 1.33$). The highest absorption

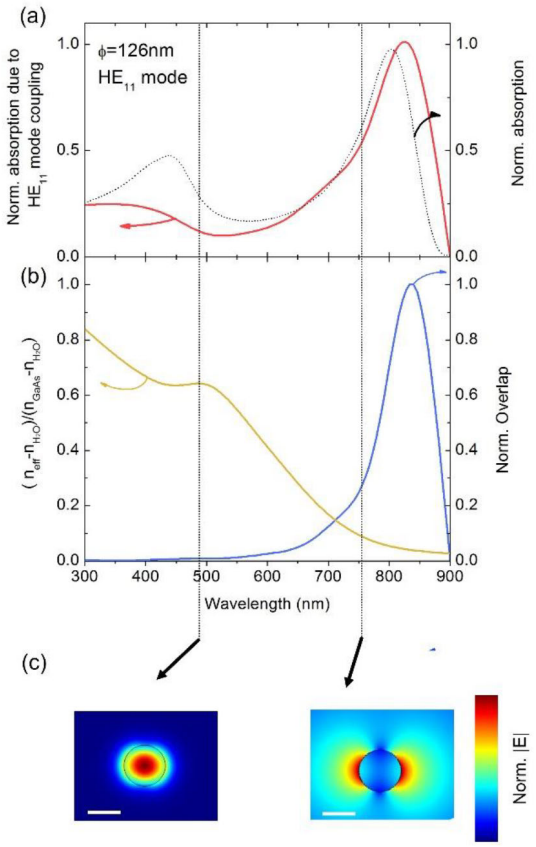

FIGURE 2.4: FDTD simulated absorption spectrum (dashed curve) linked to the light coupling into the HE_{11} guided mode of a 126nm-thick GaAs infinite NW in water. The spectrum of the latter (red curve) is given by the product of the mode overlap with a plane wave (blue curve), confinement (yellow curve) and extinction coefficient (not represented). (c) Field distribution of the HE_{11} eigenmode at two wavelengths. Scale bar is 100 nm. Reproduced with rights from [79]

is found nearby the GaAs bandgap energy, in the form of a pronounced peak centered around 800 nm. This feature can be well reproduced by considering light coupling to the first order waveguided mode, HE_{11}, of an infinite GaAs cylinder surrounded by water (red curve). The HE_{11}-related spectrum was obtained by the product of the overlap of the field distribution of the mode and a plane wave (blue curve), with the mode confinement inside the NW (yellow curve) and the GaAs extinction coefficient (not represented). The overlap is calculated by considering the complex wavefunction of the mode and that of a plane wave propagating along the NW axis [79].

It is interesting to note that the overlap is expected to monotonically increase with wavelength for the fundamental HE mode. With increasing wavelength, the mode expands and becomes more delocalized and thus the spatial overlap with a plane wave increases. However, at some point the field intensity of the mode becomes negligible and so does the coupled power. In the case of higher order modes, the mode also disappears due to cut-off conditions. As a consequence, the overlap, and thus in-coupling, shows a maximum at a wavelength close to cut-off conditions when mode localisation is very small (<1%).

By comparing the lineshape of the different components that lead to the absorption spectrum, one can recognise that the peak in overlap mostly defines the presence of a peak in absorption. The absorption peak is actually asymmetrically broadened at lower wavelengths, due to the rising contribution from the stronger absorption through the more confined mode as the wavelength becomes smaller. Indeed, the shorter the wavelength the more confined is the mode giving rise to an effective refractive index closer to bulk GaAs. Despite the very poor light coupling (i.e. small overlap), the calculated absorption spectrum exhibits a secondary broad feature at short wavelengths arising from the strong absorption coeficient of GaAs and large field concentration inside the NW. In general, mode confinement and strong coupling cannot occur together with a plane wave as excitation source, and absorption in vertical NWs is always a compromise between the two, where confinement dominates at shorter wavelengths and strong light coupling dominates at longer wavelengths.

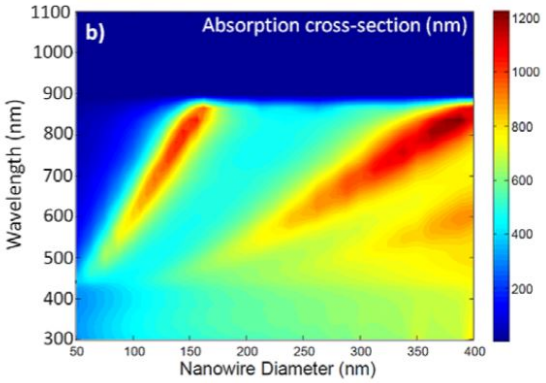

FIGURE 2.5: FDTD simulated absorption cross-section of a 2 μm-long single GaAs NW standing on a Si substrate as a function of diameter. Reproduced with rights from [80].

Owing to the confinement/overlap condition for the wavelength at which absorption peaks, light absorption in NWs is highly dependent on its dimensions. An example is given in figure 2.5, where the absorption cross-section (σ_{abs}) calculated for a 2 μm-long GaAs NW is shown as a function of NW radius [80]. In here, the NW is surrounded by air, and thus the peaks will appear shifted compared to the previous case. In any case, two main branches related to the HE_{11} and HE_{12} modes are clearly visible. It is interesting to realise that most of the in-coupled light will be quasi-guided along the NW surface and only a small fraction will actually travel through the GaAs. However, the light coupling is so strong, that is able to capture light far from the NW, resulting into absorption cross-sections an order of magnitude bigger than the NW geometrical cross-section. As a result, the effective absorption efficiency of NWs (i.e. $\sigma_{abs}/(\pi r_{NW}^2)$, with r_{NW} being the NW radius) can be far above 100% [40].

2.2.3 Length-Dependent Absorption Cross-Section

When studying light interaction with NWs, it is typically assumed that the aspect ratio of the NW is large ($length >> diameter$) and that at long distances, $length >> distance^2/\lambda$, scattering functions can be approximated to those of infinitely long cylinders. However, the aspect ratio also plays a

role in the nature of activated optical modes. It has been shown that the light scattering from a sphere, a cube and a low aspect ratio cylinder (i.e. a disk) is very similar. Thus, low aspect ratio NWs can still be regarded as Mie resonators [81]. An example is shown in figure 2.6. Figure 2.6a shows the scattering cross-section of a Si cylinder as a function of wavelength and cylinder height, for a fixed diameter of 100 nm. The length is spanned from 100 to 1000 nm, thus varying the aspect ratio (AR) from 1 to 10. At small ARs, one can distinguish two clear features at wavelengths around 450 and 500 nm, assigned to electric and magnetic dipole (ED and MD, respectively) resonant excitation. As the cylinder length is increased, the modes red-shift, which has been previously explained by the current loop fitting better inside the longer particle and thus a larger fraction of the field is in the high index medium [81]. The red-shift eventually is thus expected to saturate when the current loop easily fits inside the cylinder. Indeed, the two modes red-shift with cylinder height and appear to merge at a wavelength of about 575 nm, at which point the red-shift appears to cease.

A similar trend can be observed for the absorption cross-section as a function of cylinder height (figure 2.6c). Figure 2.6d shows a few selected absorption spectra in logarithmic scale for several ARs. As the NW becomes longer, only peaks associated to the coupling of light into leaky/guided modes are visible. The spectral position of the main absorption peak shifts to longer wavelengths with NW length, asymptotically reaching the expected peak position for an infinite one.

Another example is shown in figure 2.7a, which displays the simulated absorption spectra of a vertical 300 nm-thick GaAs NW free-standing in water. We consider various NW lengths, up to much larger values (i.e. 30 μm). In here, the absorption cross-section has been divided by the geometrical cross-section of the NW, thus giving a measure for the apparent absorption. It is clear that the longer the NW the larger the absorption, reaching levels far above 1 and does not seem to saturate. As a result, the NW appears as a funnel for light that uptakes light far from the NW boundaries, up to 10 times farther away than its own radius at the absorption peak in the longest NW discussed here (see sketch in figure 2.7b).

Depth dependent light absorption in bulk homogeneous media is commonly explained by the well-known Beer-Lambert (BL) law. BL assumes

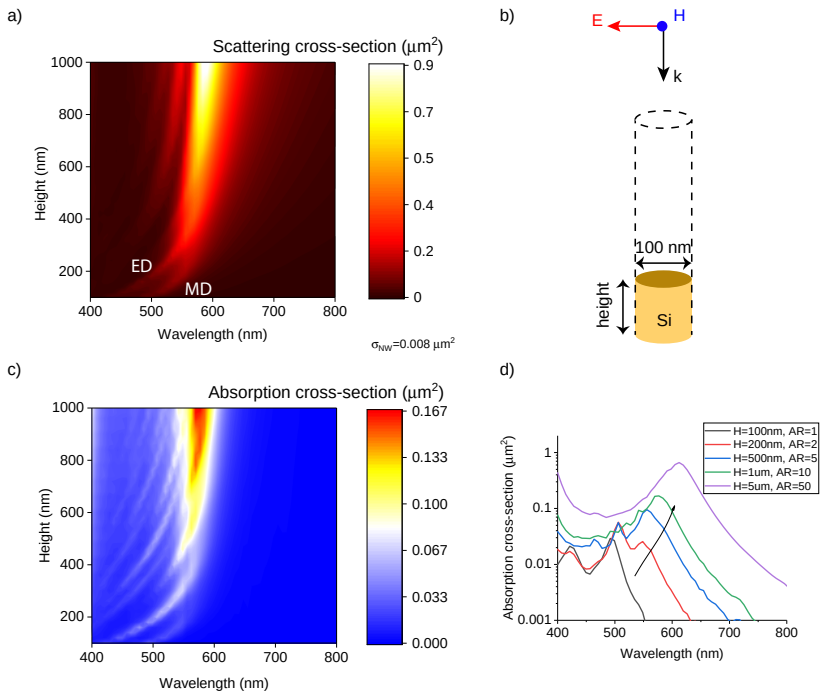

FIGURE 2.6: FDTD calculated scattering (a) and absorption (c) cross-section of a 100 nm-thick Si cylinder in air as a function of cylinder height. The light source is a plane wave with propagation direction along the cylinder axis as indicated in (b). d) Calculated absorption spectra for a few height conditions, indicating the shift and absorption increase with increasing the cylinder aspect ratio (AR).

that the light intensity decays exponentially as it travels through a lossy medium, with a characteristic decay length l_α given by the absorption coefficient ($1/l_\alpha = \alpha = 4\pi\kappa/\lambda$, with κ being the extinction coefficient) of the medium. As such, the absorption as a function of material thickness t follows $Abs = 1 - e^{-\alpha t}$. The BL law has been extensively used to fit the absorption as a function of thin film thickness to experimentally obtain the absorption coefficient of a new material.

Inspired by the BL formalism, we plot the apparent absorption as in figure 2.7 but now as a function of NW length (L) at three different wavelengths: 488, 561 and 640 nm (data points in figure 2.8a). Interestingly, we

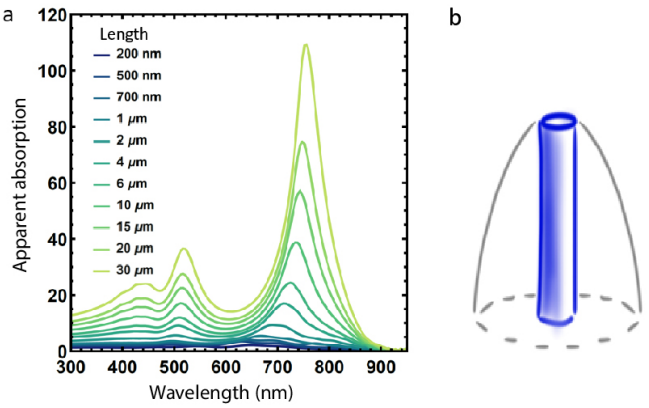

FIGURE 2.7: a) Apparent absorption of a single free standing GaAs NW surrounded by water, with diameter 300 nm and different lengths as specified in the legend. b) Schematic representation of the evolution of the absorption cross-section with NW length.

find that the absorption does seem to follow a similar exponential trend as in that expected from BL. The key discrepancy is the fact that in bulk, the absorption can never exceed 1. For a NW, however, the absorption cross-section can be tens or hundreds of times bigger than the geometrical cross-section thus resulting into effective absorption far above 1. This effect can be taken into account by incorporating the term Abs_∞, which stands for the highest absorption efficiency for an infinite NW, leading to the modified BL equation:

$$Abs_{eff} = Abs_\infty(\lambda)\left(1 - e^{-\alpha_{eff}(\lambda)L}\right) \tag{2.2}$$

Abs_∞ is left as a fitting parameter together with the effective absorption coefficient (α_{eff}), both of which are highly dependent on the wavelength. Fitting the data to equation 2.2, we find very poor fits, specially in the short NW regime. However we find that a reliable fit is obtained by adding a second exponential term, such that:

$$Abs_{eff} = Abs_\infty^{short}(\lambda)\left(1 - e^{-\alpha_{eff}^{short}(\lambda)L}\right) + Abs_\infty^{long}(\lambda)\left(1 - e^{-\alpha_{eff}^{long}(\lambda)L}\right) \tag{2.3}$$

, where now we distinguish between a short range and a long range component. The best fit is plot as solid lines in figure 2.8. The short and long

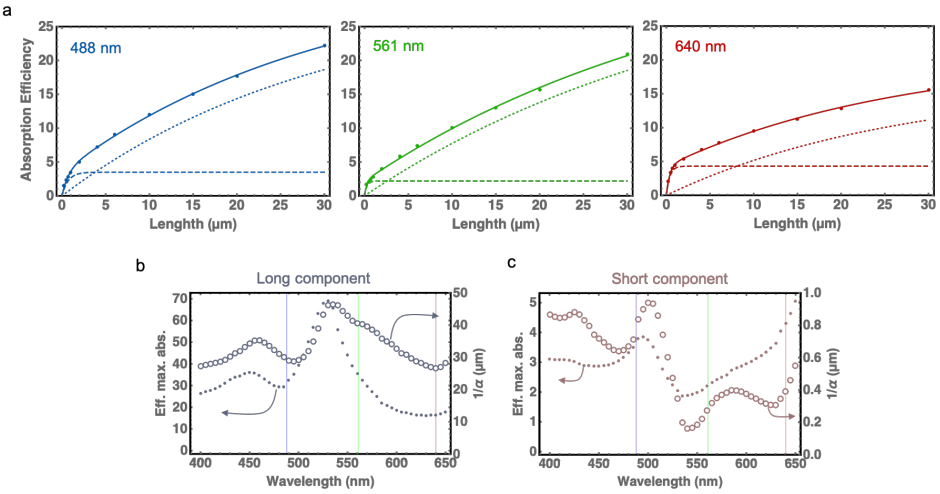

FIGURE 2.8: a) Apparent absorption of a 300 nm-thick GaAs NW in water as a function of NW length at three different wavelengths as indicated in each graph. Solid lines correspond to the fitted double term modified BL equation. Dashed and dotted lines correspond to the short and long range contributions to the fit, respectively. b) and c) Fitted maximum absorption and absorption coefficient as a function of wavelength for the long and short range terms in equation 2.3, respectively.

components to the fit are also plot as dashed and dotted curves, respectively. The outstanding agreement between the fitted curve and the simulated absorption as a function of length indicates that the modified two-term exponential BL equation is a proper model to better understand length-dependent light absorption in NWs. A few observations arise from the fits in figure 2.8:

- The strength of the short range component given by the Abs_∞ parameter (and as indicated by the saturation value of the absorption) is always much smaller than that for the long range one
- The short range terms shows a characteristic length that is consistently in the order of a few hundredths of nanometers
- The characteristic length for the long range component seems to exceed the longest NW length investigated here (i.e. 30 μm)

- There is a finite absorption efficiency (or cross-section) for the infinite NW given by $Abs_{\infty}^{short} + Abs_{\infty}^{long}$

To acquire a broadband overview of the long and short range contributions, figures 2.8b and c show the fitted values for the respective maximum absorption, Abs_{∞}, for wavelengths ranging from 400 to 650 nm (filled dots). The wavelengths 488, 561 and 640 nm are marked with blue, green and red vertical lines. The inverse of the fitted α_{eff} is also plotted as open circles in figures 2.8c and d.

One can see that the characteristic absorption length is up to 50 μm for the long component while the short range component is only present in the first 1 μm of the NW. It is interesting to note that in this wavelength range, the characteristic absorption length for bulk GaAs is in the order of 10-300 nm. While the short range component has values of α_{eff} closer to those of bulk GaAs, on average these values represent about 50% of the absorption coefficient of GaAs. We interpret such a percentage as the fraction of light localisation. On the other hand, α_{eff}^{long} is only up to about 1% of that in bulk GaAs, indicating a highly delocalised light. As discussed earlier, light is able to interact with the NW modes when leaky. Thus it is not surprising that Abs_{∞} for the "leakier" long range component is much larger than that for the short range. We tentatively interpret Abs_{∞} as a measure for light coupling.

Finally, we comment on the spectral features of the fitted parameters. In this wavelength range, the absorption spectrum of the longest NW shows a two main features at 450 and 540 nm associated to different optical modes (see figure 2.7a). Similar features at these wavelengths also appear in the long range component fitted parameters. Interestingly, Abs_{∞}^{short} also displays two peaks but are blue-shifted relative to the long component ones. We explain this effect by the stronger confinement of the short-range component.

2.3 Experimentally Probing the Length-dependent Absorption in Vertically Standing NWs

One way to experimentally probe the length-dependent absorption in vertically standing NW is by measuring the absorption in multiple NW arrays of the same diameter but various lengths [82, 83]. However, apart from inconvenience of having to transfer NW arrays onto transparent supports or make them free-standing, it is practically unlikely to obtain NWs with exact same diameters and different lengths. A more practical solution would be a single measurement in which the depth-dependent absorption is acquired for NWs that may still be standing on opaque substrates. Confocal fluorescent microscopy has proven to provide 3D maps of light around vertical NWs where the strong long-range disruption of the light path along the NW is probed [79, 84]. Moreover, multimode waveguiding in NWs has been experimentally demonstrated with fluorescence emission profiles from dye-decorated NWs [85]. In these works it has been shown that fluorescent dyes in water surrounding nanophotonic objects are excellent probes for the field distribution around them at the laser frequency. This is particularly true for distances far from the nanostructure. In the case of NWs, light matter interactions for emitted fluorescent light is more complex as dye molecules sit within the first few nanometers to the object surface. Next, we explain this technique in more detail.

2.3.1 Confocal Fluorescent Microscopy

Confocal microscopy, most frequently confocal laser scanning microscopy (CLSM) or laser confocal scanning microscopy (LCSM), is an optical imaging technique for increasing optical resolution and contrast of a micrograph by means of using a spatial pinhole to block out-of-focus light in image formation [86]. An example of the working principle of a confocal microscope is shown in 2.9a, where two pinhole apertures are positioned at confocal positions. The first pinhole focuses the light beam on a small part of the sample and the second pinhole –together with the dichroic mirror and the second filter- only allows the fluorescent light from that small part of the sample to be detected.

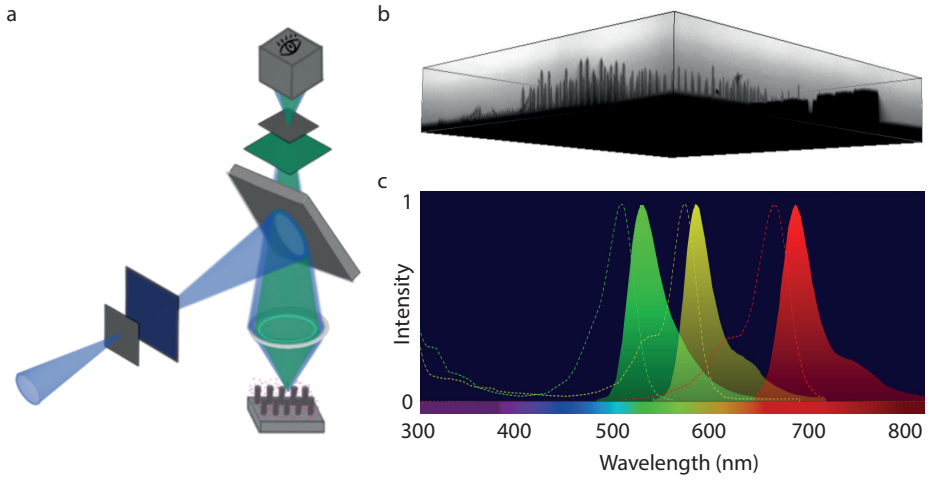

FIGURE 2.9: a) Sketch of a confocal fluorescent microscope. b) Cube data of vertically standing GaAs NWs on GaAs substrate obtained from fluorescent confocal microscopy. The NWs and the substrate which emit no light are seen in black. c) Excitation (dotted lines) and emission (filled solid lines) spectra for fluorescent dyes Alexa Fluor 488, Alexa Fluor 546, and Alexa Fluor 647 from Sigma Aldrich in green, yellow and red, respectively.

2D images are produced by either moving the sample with a piezo-stage or by rastering the light beam with fast mirrors. The later (i.e. laser scanning confocal microscopy) is much more convenient in fluorescence as it mitigates quenching of the dye. By taking 2D images at increasing depths of focus, it enables the reconstruction of three-dimensional maps of light (a process known as optical sectioning). Figure 2.9b is an example of the 3D fluorescence image of dye-embedded NW array. The represented gray transparency indicates the amount of detected light, so dark areas represent areas from where no light is being detected. The substrate and NWs appear as black, due to the lack of fluorescent molecules in those volumes. Everywhere else, the detected fluorescence is considered to be a quantitative measure for the field energy density at that spot.

Fluorescent dyes are excited most efficiently at a particular wavelength and emit at a slightly lower wavelength (i.e. Stokes-shift). Such an energy difference between excitation and emission is beneficial to efficiently filter

the laser out and thus ensure that only fluorescent light is detected. Figure 2.9c shows the excitation (dotted lines) and emission (filled solid lines) spectra for three fluorescent dyes that will be used in this work: Alexa Fluor 488, Alexa Fluor 546, and Alexa Fluor 647 in green, yellow and red, respectively. The dyes are chosen in a way that the absorption peaks resulted by light-coupling to the first and second order leaky/guided modes for our NWs fall in the spectral range that excites the dyes efficiently.

2.3.2 Imaging Light Extinction in GaAs Vertical NW Arrays

We now visualise light extinction in GaAs NWs with confocal fluorescence microscopy. The sample consists of fields of NW arrays etched down from a GaAs substrate. The NW diameters range from $\sim 300\,\text{nm}$ to $\sim 400\,\text{nm}$ and are spaced by a pitch distance of $3\,\mu\text{m}$, so that the wires are far enough to minimize optical interaction. More details on the sample fabrication can be found in the Methods section 2.5. Figures 2.10a, b and c are x-y cuts from 3-dimensional mappings of light distribution around the NWs by using fluorescent dyes Alexa Fluor 488, Alexa Fluor 546 and Alexa Fluor 647, respectively. These dye molecules are excited with respective laser beams of wavelength 488 nm, 561 nm and 640 nm. The NW positions are revealed by the black spots. As explained in earlier works [79], the emitted fluorescent light intensity of the molecules is proportional to the local excitation field energy density. Thus by scanning the sample in the x-y-z planes we obtain a diffraction-limited resolution image of the field intensity distribution around NWs.

To better visualize the depth-dependent light distribution, figures 2.10d, e and f show y-z plane cuts of the exact same area for the three wavelengths. All images have been normalised to the maximum fluorescence intensity, far above the NWs. Close to the substrate, the darker color indicates that almost no light reaches the substrate owing to the NW's presence. Taking a closer look at the vertical cuts, we can see that each NW has a dark dome-shaped shadow around them, the exact shape and strength of which depends on the excitation wavelength. The shape of this shadow resembles that of the absorption cross-section described in figure 2.7. For the considered NW geometry and wavelengths, extinction is mostly ruled by absorption. The observed shadows may be thus regarded as a measure

for the absorption around the NWs. Given that the three images in figure 2.10d, e and f are taken at the same precise NWs, direct comparison between 3D absorption at different wavelengths is possible.

As means to better resolve differences with the shadow shape around the NWs for different wavelengths, we plot a series of y-z vertical cuts by rotating the x-cutting plane with respect to the high-symmetry axis of the array (see right top-image in figure 2.11). We zoom-in to a row of five equally long ($\sim$ 9 μ) NWs. The images in figure 2.11 show the vertical cuts in 5° increments in rotation for two of the dyes. To enhance the contrast, we now use a double-gradient colour scale (see the Look-Up Table of the colour scale at the bottom right of figure 2.11). The scale is chosen

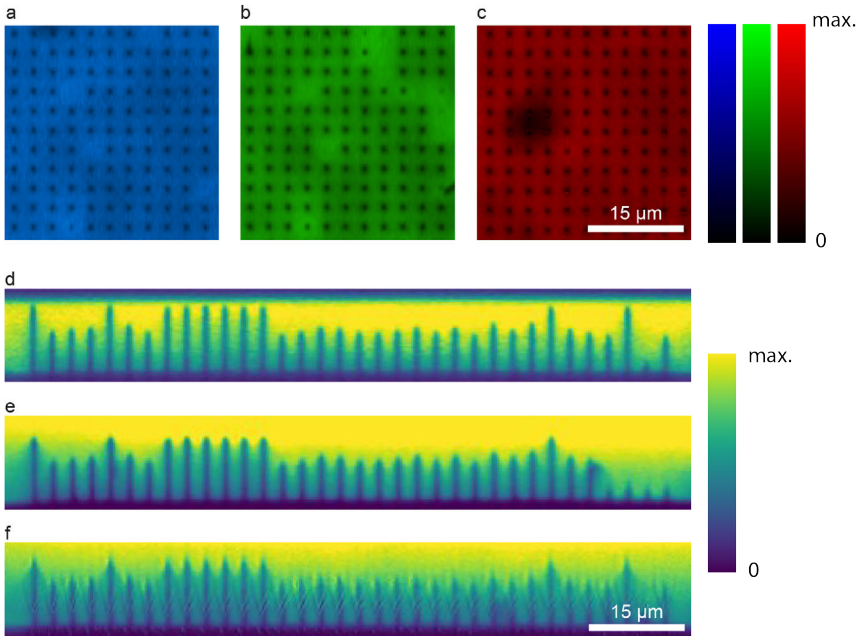

FIGURE 2.10: a), b), and c) Fluorescence 2D images of a GaAs NW array on GaAs substrate, embedded in water with fluorescent dyes Alexa Fluor 647, Alexa Fluor 546 and Alexa Fluor 488, respectively. Note that despite the same area is imaged at the different wavelengths, some of the NWs have broken off between experiments. d), e), and f) y-z cross-cut images of the exact same row of NWs for the three wavelengths, respectively.

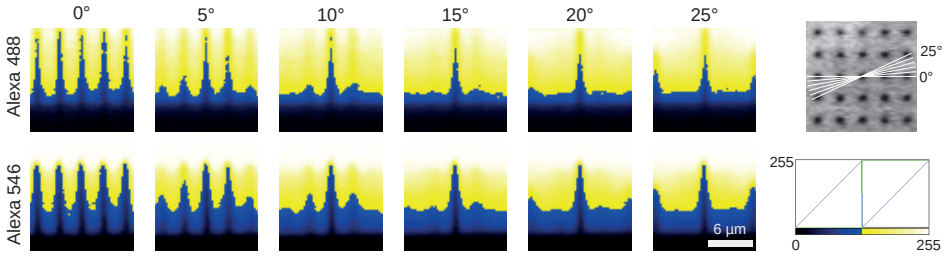

FIGURE 2.11: Emitted light distribution in y-z planes for a row of five equally long (~ 9 μm) NWs for two fluorescent dyes (labeled as Alexa 488 and Alexa 546). The data cubes are cut at 5°,10°,15°,20°, and 25°. At 20° the absorption shadows of NWs from the adjacent rows are emerging.

such that a large blue-yellow contrast is shown at 50% of the maximum intensity. Already from the images at $0°$ with this color scale one can better distinguish a different shape of the shadow around the NWs between the two wavelengths. By imaging the vertical cuts off-axis, we basically trace the shadow in depth and provide better statistics.

In the following, we compare the experimentally measured 3D extinction with the theoretical length-dependent absorption cross-section. To do so, we make use of the modified BL equation and fitted parameters from the previous section. At a given height (z) from the substrate, the absorption cross-section x and y boundaries around a NW are defined by:

$$(x - x_0)^2 + (y - y_0)^2 = r_{NW}^2 Abs_{eff}(L_{NW} - z) \tag{2.4}$$

, where x_0 and y_0 indicate the NW position. r_{NW} and L_{NW} correspond to the geometrical NW radius (150 nm) and length (9 μm), respectively. Since the color scale of the confocal images is chosen so that a strong contrast is given at 50% extinction, we multiply the absorption cross-section by a factor 2.

Figure 2.12 shows again the two vertical cuts at $5°$. Overlapped, we plot the depth dependent absorption cross-section as calculated by equations 2.4 and 2.3 with a dashed red line. We have used the fitted parameters at the two laser wavelengths (488 and 561 nm). We also plot the contribution from the long range component as solid line. In both wavelengths, we

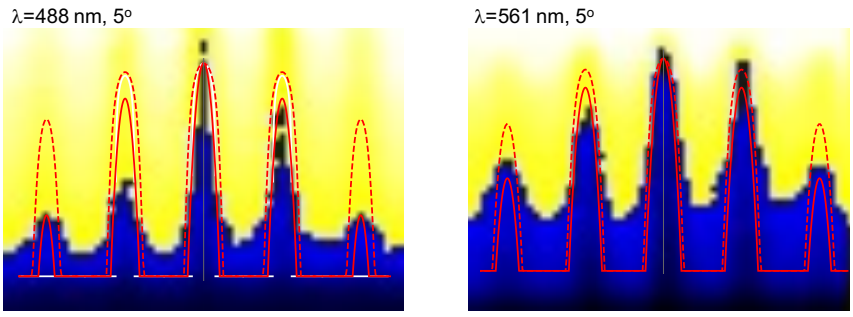

FIGURE 2.12: Vertical cuts of confocal data at 5° rotation for two excitation wavelengths of 488 and 561 nm, overlapped with calculated depth dependent absorption cross-section (dashed red lines) and long component contribution (solid red lines).

observe a very good agreement between the confocal data and the long-range absorption cross-section (solid curve), rather than with the total absorption cross-section (dashed curve). It seems thus that the contribution of short-range interactions is absent. While this could be limitation in our experiment, it is also possible that the short-range interactions are only allowed in short NWs. Further investigation is needed to fully understand this effect.

2.4 Conclusions

In this Chapter we dive deeper into understanding optical properties of semiconductor NWs as promising building blocks for next generation photonics and photovoltaics. After explaining analytical methods that describe light-matter interactions for a single infinite cylindrical NW surrounded by a homogeneous medium, we have focused on length-dependent absorption cross-section in NWs with various aspect ratios, ranging from disk-like Mie resonator to ~ 5 μm Si NWs. With increase in height, the evolution of the absorption features from ED and MD Mie modes into leaky/guided modes are visible. Moreover, inspired by the BL law, we fit the FDTD simulated absorption efficiency vs. length of a single free standing GaAs NW with diameter 300 nm and lengths ranging from 200 nm to ~ 30 μm. Doing

so, we are able to distinguish between two components in absorption, a short range and a long range one, which arise from strong confinement and strong coupling between the NW's mode and the plane wave, respectively. The outstanding agreement between the fitted curve from modified BL and the simulated absorption as a function of length indicates that the modified two-term exponential BL equation is a proper model to better understand length-dependent light absorption in NWs. Then, we perform confocal fluorescent microscopy on GaAs NW arrays on GaAs substrate, in order to provide 3D maps of light distribution around NWs. Dark shadows around the NWs are associated to their absorption cross-section. We compare the shadows obtained in the fluorescence images with different laser excitations to the simulated length-dependent absorption cross-section. We surprisingly find that the shadow is very well explained by neglecting the short range BL component. This work provides direct evidence and comparison for different wavelengths of the length-dependent absorption in NWs.

2.5 Methods

2.5.1 NW Fabrication

In this work we have used nanowire arrays fabricated at University of Eindhoven via top-down method by lithography and dry-etching of an undoped (100) GaAs wafer. First, the substrate is cleaned from the native oxide by immersing in weak ammonia solution, with the following PECVD deposition of 600 nm SiN_x layer. To transfer the pattern into SiN_x, E-beam lithography (EBL) is used. A layer on negative e-beam resist MAN-2410 of 600 nm is spin-coated on the SiN_x and the resist is baked on the open hot plate for 180 seconds at the temp of T=100°C. The sample is transferred to the EBL chamber and exposure is performed. MAN532-S is used as the developer solution for the exposed structures. The sample is put into developer solution for 110 seconds to ensure the full structures development and vertical sidewalls of the developed nano-pillars. To clean off the leftovers of the resist, the wafer is immersed in the H_2O bath for 600 seconds. The sample is then put in the reactive ion etching (RIE) chamber (N-RIE) to transfer the resist pattern into SiN_x. With an etching rate of 14.3 nm/min, the pattern is transferred after 32 min of the etch. To remove the resist leftovers, the sample is put in acetone solution overnight. To ensure complete removal of the resist, ICP-RIE etching of NWs is performed, using SiN_x as a mask. In this step, $Cl_2/Ar/N_2$ 7/4/2 sccm with an RF power =200 W, ICP power = 700 W, reactor pressure of 3 mTorr and etching time of 7 minutes is used. After this step, the samples are put in 10% HF solution to clean the sidewall passivation and leftovers of SiN_x mask. SEM images of the as-fabricated NW array are shown in figure 2.13. The NW diameter and length were targeted to be around 300 nm and 8.8 μm, respectively. The non perfect anisotropic etching leads to NWs with a reduced diameter ($\sim$ 235 nm) at the center of the NW compared to that at the tip and bottom ($\sim$ 315 nm), resembling an hourglass shape.

2.5.2 Confocal Microscopy Set-Up

We have used an inverted confocal microscope (Nikon A1R-MP), equipped with diodes and diode-pumped solid-state lasers (DPSSL). In this work,

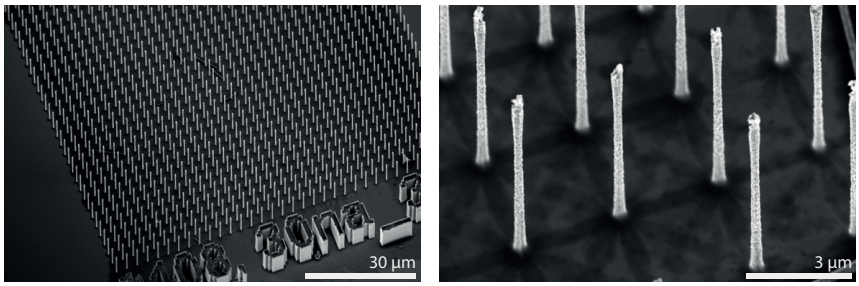

FIGURE 2.13: SEM images of nanowire arrays made with wet etching.

we have used excitation wavelengths of 488, 561 and 640 nm. The system is equipped with two scanners, Galvano scanner and Resonant scanner. The latter is the one used in our measurements. There are four PhotoMultiplier detectors that together with a range of filters are used for selective confocal fluorescent detection. In all measurements 100x oil-immersion objective was used (Apo TIRF, NA=1.49). The pinhole was set to 1.2 Airy unit to find a good compensation between the high resolution and good contrast in the images. For the dye solutions, the concentration was set to 500 μM in DI water. The resolution in x-y plane (focal plane) is given by 0.44 λ/ NA and the resolution in z plane (axial plane) is calculated as 0.75 λ/ NA.

CHAPTER 3

Coloured and Semi-Transparent Nanowire-based Solar Cells for Building Integrated Photovoltaics

Building-Integrated Photovoltaics (BIPV) provide smart spatial solutions to integrate solar cells into already-built areas, which is of extreme importance to maintain and increase the pace of energy transition of our time. Here, we study colourful and semi-transparent PV (ST-PV) based on semiconductor nanowires (NW) as a promising BIPV element for windows. We perform FDTD simulations for different PV materials in a wide range of NW array geometries and report interesting trends between the photocurrent (J_{ph}) and average visible transmittance (AVT), next to varied shades of corresponding perceived transmitted colours. Besides, we find opposite trends in J_{ph}/AVT versus incidence angle for different array geometries. It appears that for arrays with symmetric shape of absorption spectra around the visible range the tilted incidence light is beneficial for the PV performance. Moreover, we provide experimental demonstration of free standing NW array-PDMS composite containing nine different geometries. We measure the transmission and compare the calculated colours to their optical image, and we demonstrate how the change in various incidence angles affects the transmitted colour.

3.1 Introduction

As mentioned in Chapter 1, integrating solar cells into already-built areas is essential to keep the pace of solar energy replacing non-clean energy sources. Especially for countries like the Netherlands, with many homogeneously dense built regions, in order to protect the landscape it is crucial to integrate these sustainable energy solutions into rooftops, building facades, windows, and other sunlight-exposed built areas [87]. Building-Integrated Photovoltaics (BIPV), which are photovoltaic systems that are used as part of the buildings' construction, are often the optimal way of integrating renewable energy systems in urban landscapes where undeveloped land is scarce and expensive. Apart from better use of space, with BIPV the electricity is generated close to where it is used (i.e. supply on-site), which reduces electrical transmission losses, the need for storage capacity, potentially installation costs and the food-vs-fuel trade-off [88, 89].

Brief History of BIPV

The use of PV on buildings is not a new concept and a long-sought aim in the PV community. Already in the 1970s, aluminium-framed PV modules were mounted on buildings in remote areas as means to supply electricity to those buildings without access to an electric power grid. A decade later, solar cell devices in the shape of module add-ons to roofs emerged. It wasn't until the 1990s when PV systems were especially designed to integrate into a building's envelope and the first integrable PV modules became commercially available [88]. In the past 10 years, BIPV technologies have experienced a tremendous growth. Currently, a wide variety of commercial BIPV systems are available in the market which can be mostly categorized in two groups of façade systems, like facades and glazing (windows, skylights, etc.), and roofing systems, such as flat or pitched roofs in shape of tiles, shingles, etc. As described in Chapter 1, BIPV is still an emergent technology with two main challenges to be tackled: How can one maximize functionality and aesthetic quality of architectural PV surfaces; and how to minimize the trade-off between performance, aesthetics, mechanical flexibility and durability. Such trade-off is found more critical for (semi)transparent PV systems (to be used as windows and facades)

FIGURE 3.1: Conceptual representation of colourful windows that could be made with semi-transparent solar cells based on semiconductor NW arrays embedded in transparent polymer (PDMS) and sandwiched in ITO contact layers (sketch shown as inset). A wide range of colours and transparency is achieved by adjusting the NW diameter (d) and pitch distance (p) of the array.

than in colourful opaque ones, likely due to the large compatibility of the latter with high-efficiency PV materials. As a result, the best demonstrated power conversion in semi-transparent PV (ST-PV) is about half of the thermodynamic limit for their respective transparency [13, 90].

In ST-PV, as the name indicates, part of the visible spectrum is intended to transmit through. As such, it can be primarily used as façade or glazing element. Depending on its broadband spectral response, ST-PV is considered wavelength-selective or non-wavelength-selective, and as such each type has its own respective fundamental efficiency limit. While the first is ideally designed to absorb the ultraviolet (UV) and near-infrared (NIR) part of the sunlight and letting the visible part (or a selected part of it) pass through, the latter offers visible transparency by means of reducing the

[0]Copyright note: Miami International Airport. Miami, Florida. Photograph by: jpellgen on Flickr. Art work by: Harmonic Convergence (2011) by Christopher Janney.

overall absorption in the cell. Advantages and challenges on different types of wavelength-selective and non-wavelength-selective ST-PV are listed in Table 1.1 in the first Chapter of this thesis. In general, the selective UV and NIR absorption makes wavelength-selective options most efficient ST-PVs, with a theoretical maximum PV efficiency of 21% at full transparency compared to the 33% efficiency limit in opaque cells [91]. The difference simply arises from the 19 mA/cm^2 of photocurrent given by the visible spectrum. While potentially efficient, wavelength-selective ST-PV are so far attained by external photonic control (with sophisticated fabrication methods) or excitonic absorbers (which either suffer from poor efficiency or stability) [92]. Non-wavelength-selective options, on the other hand, are simple in fabrication (e.g. by reducing the amount of absorber material) at the cost of colour control and the largest compromise in conversion efficiency. This highlights the importance of harvesting NIR photons to maximize efficiency [64, 93–95].

In this Chapter we exploit built-in nanophotonic concepts in nanostructured PV materials to minimize the negative effects of semi-transparency and colour on efficiency in ST-PV. We propose free-standing semiconductor NW arrays as a new promising solution for highly performing aesthetically pleasing coloured and ST solar cells, which introduces a new class of ST-BIPV in between wavelength–selective and non–wavelength–selective. Semiconductor NWs are well-known for their large absorption per unit volume, which has been proven useful in photovoltaic and photoelectrochemical applications [40, 96–100]. Owing to light coupling into leaky waveguiding modes in vertically standing NWs (see Chapter 2), the absorption spectrum of NW arrays can be tailored by geometry (i.e. NW diameter and pitch distance) without the need for modifying material composition [80, 101–103]. Such control over the absorption spectrum in NW arrays has enabled completely new concepts for tandem PV designs [63, 64, 104] and it offers a smart way to introduce wavelength–selective semi-transparency in single junction solar cells by reducing the photoactive material volume in a controlled manner. An additional advantage of NW-based ST-PV is their compatibility with high efficiency PV materials such as III-V semiconductors and Si, which opens up the possibility of minimising the compromise between aesthetics and power conversion efficiency often found in other wavelength-selective PV materials. Thanks to peeling-off techniques, NWs

can be removed from their growth substrate to any transparent external support for the realisation of semiconductor PV windows [32, 105].

Here, we explore how these unique built-in wavelength-selective photonic properties in NW arrays can be exploited for building integration as ST-PV. The NW arrays, in this study, are embedded in a transparent polymer layer and sandwiched between two transparent contacts to form the PV stack. We use FDTD simulations to estimate the colour, transparency and PV performance of free-standing vertical NW array cells based on three common high-efficiency PV materials, namely GaAs, InP, and Si. We find counter-intuitive interplay between transparency and PV performance in this new class of ST-PV, which we explain from the dispersion of multiple waveguiding orders with NW diameter. We then fabricate free-standing GaAs NW arrays with nine degrees of transparency and colour. We examine the effect of illumination angle on their appearance with wide-field optical microscopy. We find that the appearance is fairly constant up to about an angle of 30°, which we explain by the competing excitation of Mie resonances and coupling into waveguiding modes.

3.2 Theoretical Considerations on Photocurrent vs AVT

3.2.1 Idealized ST-PV

First, we illustrate ideal cases of wavelength and non-wavelength selective PV approaches, and their respective maximum PV performance as a function of degree of transparency. The degree of visible transparency is quantified by the Average Visible Transparency, or AVT [91, 106]. In ideal wavelength-selective cells the absorption spectrum resembles that of a bandpass filter, where the transmission fraction and bandwidth determine the cell's AVT. Figure 3.2a and b showcase two ideal wavelength-selective absorption spectra, where the AVT is given by a constant transmission fraction throughout the whole visible spectrum (labelled as "Gray Scale") or it is given by the bandwidth of a 100% transmissive spectral band (labelled as "Colour-Selective"). In the latter, we have chosen that the bandpass minimal wavelength is fixed at 390 nm. While in the "Gray Scale" case, the

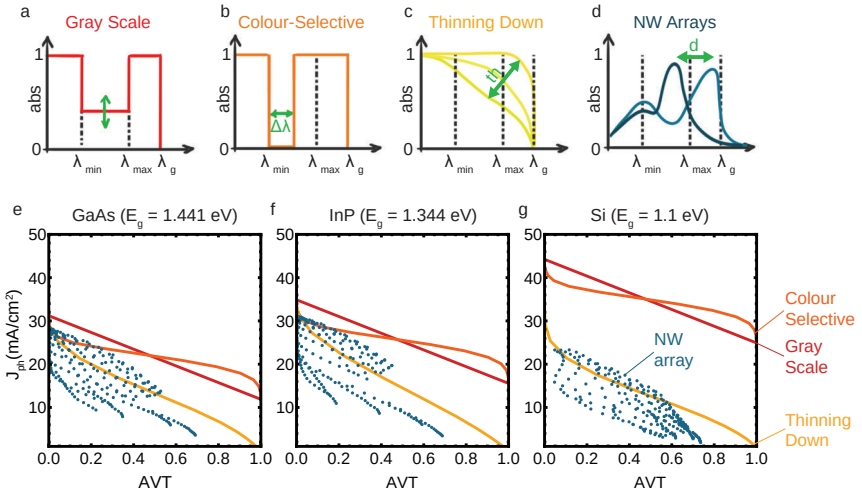

FIGURE 3.2: Top: Sketch of ideal broadband absorption spectra for two wavelength-selective ST-PV approaches of a) "Gray Scale" and b) "Colour selective", and non-wavelength-selective approach of c) "Thinning Down" compared to this work's approach d) "NW Arrays". Shades of yellow in (c) demonstrate three thicknesses for the absorber material, and two shades of blue in (d) showcase two different diameters of NW as examples. Bottom: Calculated photocurrent density (J_{ph}) versus Average Visible Transmittance (AVT) of different approaches for three common PV material of e) GaAs, f) InP, and g) Si. The colours of the spectra and the data points correspond to (a) to (d) scenarios. Each data point results from an FDTD simulation of a NW array with specific diameter and pitch (As shown in figure 3.1)

AVT value is directly given by 1-Absorption, to calculate the AVT in the "colour-selective" case one needs to take the cell transmission and photopic response of the human eye into consideration. More details on the AVT calculations and photopic response of the human eye can be found in the SI.

Next to the two wavelength-selective ideal show-cases, figure 3.2c shows the absorption spectrum of a non-wavelength-selective approach, where transparency is induced by thinning down the absorber layer (labelled as "Thinning Down"). This is the simplest way to achieve transparency in a cell from the fabrication point of view. In this case, one can consider the Beer-Lambert law to obtain the thickness-dependent absorp-

tion for a given absorber material, sketched in shades of yellow in figure 3.2 c. Figure 3.2 e, f and g show the maximum photocurrent as a function of AVT for GaAs, InP, and Si, where we assume ideal absorption in the three semi-transparency scenarios described above. In all three ideal semi-transparency scenarios (*Gray Scale*, *Colour-Selective* and *Thinning Down*), we have neglected reflection at the glass or solar cell, thus representing the respective upper limit performance. As expected, the more transparent the solar cell the lower the photocurrent. Note that the *Thinning Down* approach is the least performing semi-transparency solution with total loss of photocurrent at 100% transparency. Contrarily, in the two wavelength-selective approaches (*Gray Scale* and *Colour-Selective*) the photocurrent loss from AVT$= 0$ to AVT$= 1$ is 19 mA/cm^2, regardless of material. It is also interesting to note, that between the two wavelength-selective approaches, *Gray Scale* seems better suited for ST-PV with AVT$< 50\%$, while for larger transparencies, *Colour-Selective* offers higher performance for the same transparency.

3.2.2 NW-Based ST-PV

We now introduce the free-standing NW-based PV stack as a ST-PV solution. Square NW arrays of either GaAs, InP or Si are embedded in a PDMS layer that provides mechanical stability which is sandwiched between two 100-thick ITO layers as transparent electrode contacts (see sketch in figure 3.1). For the PV effect one requires asymmetric contacts, which may be achieved via doping within the NW [50, 53, 54, 97] or by the introduction of thin carrier blocking layers or selective contacts [55, 60, 107]. Additional passivation layers at the large surface area of the NWs is also crucial to maximize the open circuit potential [53, 97, 107]. Since the optical response of the arrays is not likely strongly affected by such thin layers or doping profiles [99, 108], we thus consider the simplified case of two symmetric ITO contact layers. We have examined periodic arrays of NWs with diameters between 50 and 200 nm, and pitch distances from 300 to 1000 nm. The NW length was fixed to 6 μm for all materials, since this length is a fair compromise between absorption efficiency and fabrication feasibility. More details of the simulation set-up can be found in the SI.

Using the transmission and absorption spectra as obtained from FDTD simulations of the NW-based PV stacks we calculate the photocurrent and AVT for a series of NW array geometries (blue data points in figures 3.2 e, f and g). Each data point represents a single array with particular combination of NW diameter and pitch distance. From figure 3.2 e, f and g, it is clear that NW array ST-PV offers a wide range of possible AVT values, up to about 70% transparency which is a similar value to what has been demonstrated so far with other material systems [90]. For reference, AVT values for residential windows varies between 15% to 90% depending on how tinted or clear the windows are and as a general rule of thumb, glass with AVT above 60% looks already clear [109]. Such a broad range of AVT possibilities for the same single-material in NW arrays is a first indicator of their potential for ST solar cell designs for different implementation areas; ranging from dark, coloured to tinted clear semi-transparent glazing.From the PV performance perspective, some NW array geometries show higher photocurrent values than those given by the *thinning down* approach for the same AVT. Furthermore, some NW array geometries even outperform the *colour-selective* approach at low AVTs ($< 20\%$ for GaAs and $< 18\%$ for InP). This result is very impressive given the fact that reflection and parasitic absorption are actually considered in the NW array PV case, contrary to the other ideal scenarios.

Effect of NW Geometry on Performance and Transparency

To get a better understanding of the mechanism behind the broad span of transparency and photocurrent values in the NW arrays, the same set of data is now plotted by colour coding the pitch distance. Figure 3.3a shows the change in AVT and photocurrent with increasing GaAs NW diameter (datapoints from right to left) for eight different pitch distances, colour-coded as indicated by the legend. Similar graphs are obtained for the other two PV materials, shown in the SI. For each pitch distance, the photocurrent vs AVT displays a sort of z-shape. This effect is most evident for the largest pitch distances. For the smallest diameter, the AVT shows the highest values in each of the pitch series. As one may expect, as the diameter is increased the AVT decreases at the same time as the photocurrent increases. However, we find a surprising switch in trend for diameters bigger than 80

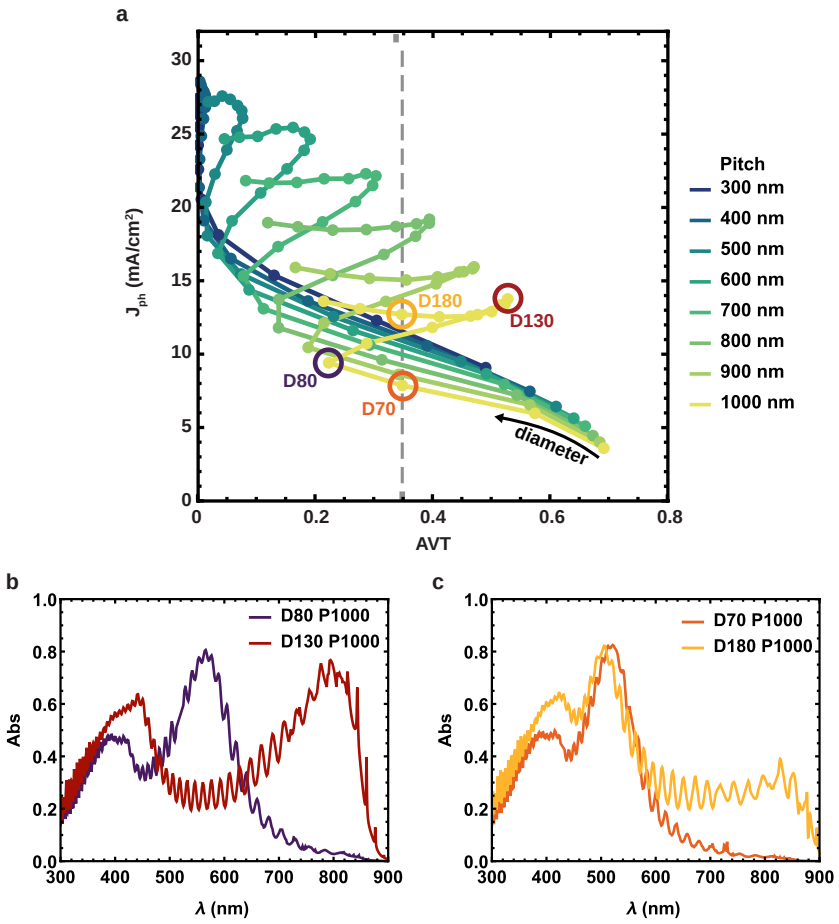

FIGURE 3.3: a) Simulated J_{ph} vs. AVT of representative GaAs NW arrays as in figure 3.2e collected by pitch values as indicated by the legend. b) and c) Absorption spectra for datapoints highlighted with circles in (a). D80 and D130 are turning points in the z-shape spectrum. D70 and D180 show different photocurrent values for the same AVT value.

nm. For diameters larger than 80 nm and up to 130 nm, the photocurrent increases along with transparency. Again, at a diameter of 130 nm, the trend switches once more, leading to the more standard anti-correlated photocurrent vs AVT. The unprecedented correlation between photocurrent and AVT that we observe for a certain range of NW diameters is an excellent

new opportunity to achieve ST-PV based on absorber reduction concepts with efficiencies beyond those obtained from thinning down the absorber. In the following, we explain this phenomenon by the diameter-dependent waveguiding properties of vertical semiconductor NWs.

First, we take a closer look at the absorption spectra (figure 3.3b) of the two GaAs NW arrays with 1μm pitch distance where the AVT vs photocurrent changes trend, namely for 80 nm and 130 nm in diameter (labelled as D80 and D130, respectively). Each geometry result in the lowest/highest transparency for similar photocurrent values among their neighbouring data points, respectively. The peaks in absorption found at ~ 550 nm for D80 ($\sim$ 450 and 800 nm for D130), are well known to arise from the efficient light coupling to HE01 (HE01 and HE02) waveguiding modes of the nanowires [79, 80] (more details on waveguiding modes can be found in Chapter 2). In the case of 80 nm GaAs NWs embedded in PDMS, the first order waveguiding mode sits right at the peak of the human eye photopic response, thereby becoming the least transparent array of all the diameter series. As mentioned in Chapter 2, increasing the NW's diameter causes a red-shift in the absorption peak(s). Because of the diameter-induced red-shift of the absorption peak, the transparency increases with diameter. At the same time, a new absorption peak appears at shorter wavelengths due to higher order waveguiding mode. Consequently, the photocurrent also increases with diameter.

The dual increase in AVT and photocurrent occurs until the NWs reach the diameter of 130 nm, at which point the first order waveguiding mode coincides with the GaAs bandgap ($\sim$850 nm). As the diameter further increases, the efficient coupling to the first order waveguiding mode no longer sits within the absorption spectrum of GaAs and thus the photocurrent sharply decreases. Notice that this effect is less evident in Si due to its indirect bandgap nature (see SI). In parallel to the photocurrent decline, the higher order absorption peak at shorter wavelengths shifts towards the visible spectral range as the diameter increases, which in turn reduces the AVT. As a result, the anti-correlation between AVT and photocurrent is attained again. We observe that at smaller pitch distances the z-shape in the photocurrent vs AVT is softer, which we attribute to the optical cross-talk between NWs broaden the absorption peaks. An interesting consequence of the z-shape behaviour is that more than one photocurrent value can

be achieved for the same AVT value. See for instance the two datapoints D70 and D180 marked in figure 3.3a. While both array geometries show an AVT value of ~ 0.35, the photocurrent is 1.6 times larger for the larger diameter (i.e. 7.8 and 12.7 mA/cm^2). The absorption spectra for these two array configurations as shown in figure 3.3c reveal that both arrays display very similar absorption peaks although arising from different order waveguiding modes. However, for the large diameter case there is the tail absorption related to the first order waveguding peak in the NIR (around 850 nm), which is the responsible for the larger J_{ph} value in D180.

In summary, the sudden correlated increase in AVT and photocurrent arises from the fact that there are multiple absorption peaks in the spectra of vertically standing NWs. For certain NW geometries, the two peaks are just positioned at each side of the visible spectral range, resembling the absorption spectra for wavelength-selective solar cells. The NW array approach to make ST coloured solar cells is a very powerful concept: by tuning their geometry through diameter and pitch, the interplay between AVT and J_{ph} can be adapted to maximize performance without the need to fine tune the material composition.

Effect of NW Geometry on Cell Appearance

Next, we focus on the NW array solar cells daylight appearance for the same geometries considered in the previous section. Figure 3.4 (left) and (right) show both simulated appearance in transmission and AVT, respectively, of GaAs, InP and Si NW arrays in a matrix form. For the appearance, we use the FDTD simulated transmittance, the D65 daylight spectrum and the Colour Matching Functions (CMF) from CIE 1964 standard [110]. Further details on the colour calculation and representation are found in the SI. At first glance, Figure 3.4 proves that NW arrays open up the possibility of creating a beautiful and diverse colour palette with a wide range of transparency for integrating solar cells into buildings. Note that the colour squares represented in 3.4(left) contain information on both colour hue as well as transparency. By comparing the AVT matrices with those for the colours in figure 3.4, one can notice that high transparency results into less saturated colours and vice-versa. Colours are highly saturated with AVTs up to 0.4 for arrays with small pitch distances. By contrast, arrays with

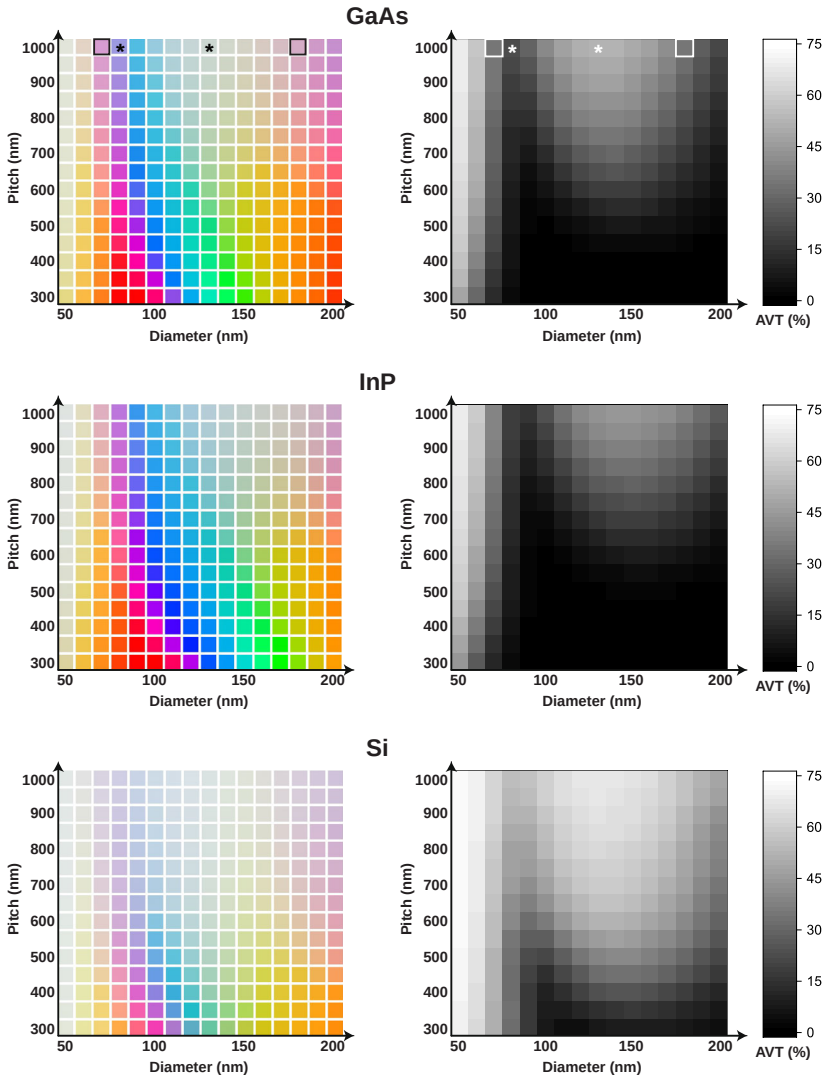

FIGURE 3.4: Left: Calculated perceived colour for NW arrays cells based on GaAs, InP, and Si. Right: AVT colourmap representation of the same NW array cells. The squares marked with an asterisk correspond to the colour and AVT for geometries whose spectra are shown in figure 3.3b. At these two diameter values, the arrays display the lowest and highest AVT for a given pitch, respectively. Framed squares correspond to the same geometries as in figure 3.3c.

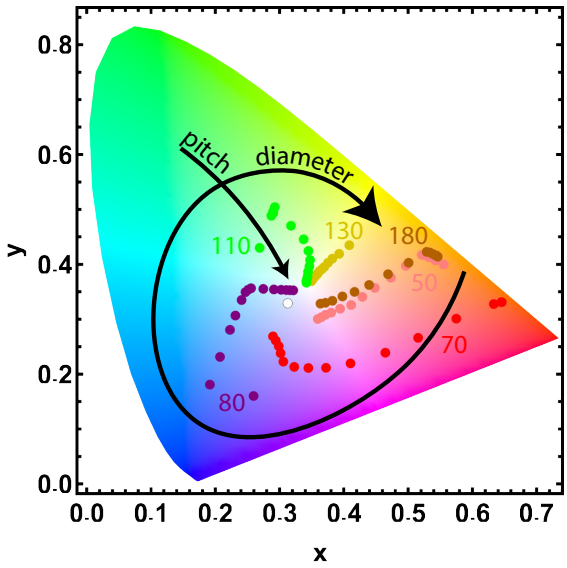

FIGURE 3.5: Chromaticity diagram overlapped with chromaticity values for GaAs NW arrays with diameters 50, 70, 80, 110, 130 and 180 nm and pitch distances from 300 to 1000 nm. The increase in diameter and pitch is indicated by black arrows.

pitch distances larger than 600 nm show less saturated colours arising from the larger degree of semi-transparency (AVT between 0.4 to 0.7). While it is sensible that the decreased NW density from increasing pitch distance induces a larger degree of transparency, we observe that the pitch also has an effect on the hue, particularly for pitch distances shorter than 600 nm (or <500 nm in the case of Si). This is observed by the gradual shift of the colour pallet to larger diameters as the pitch decreases. The hue is also highly dependent on NW diameter. At a given pitch distance, the colour follows the inverse of the rainbow order by increasing diameter and eventually repeating colour at larger diameters (see for instance the two squares highlighted in the GaAs colour matrix). Such a trend of colour hue with diameter is not unexpected given the red-shift of waveguiding-induced absorption peaks with increasing diameter, as explained in the previous section.

A different and more objective way to describe the effect of NW array geometry on the appearance is by using the chromaticity diagram (figure

3.5). The chromaticity x and y coordinates are given by the normalized tristimuli, as described in the SI. More intuitively, in the chromaticity diagram the hue is indicated by the angular component from the central white point, while the radial component indicates colour purity (i.e. pure colours are represented at the edge of the diagram). Overlapped with the chromaticity diagram in figure 3.5, we include datapoints indicating the colour evolution of GaAs NW arrays with changing pitch distance for seven different NW diameters (chromaticity plots for the other two material systems can be found in the SI). Arrays with same NW diameter are represented by datapoints of the same colour (e.g. red datapoints correspond to arrays of 70 nm in diameter). As expected from the colour pallets, we find that the various array geometries cover most of the chromaticity plot. Looking at the farthermost datapoint from the center of each diameter configuration, it is clear that the hue changes with diameter in a cyclic fashion from red to blue, green, yellow to red again (represented by the circular black arrow). This repeat in colour arises from the fact the higher order waveguiding mode appears at the same spectral position as the diameter is increased.

With increasing pitch distance (as indicated by the straight arrow), the array appearance is brought towards the central white point, arising from the increase in transparency. However, it is interesting to note that while there is a fairly straight radial shift in the pitch-induced appearance change for the diameters of 130, 140 and 200 nm, there is also a pitch-induced hue shift in the case of diameters of 80, 90 and 110 nm. This pitch-related hue change is not just an effect that occurs due to the small diameters (as it does not occur for smaller diameters like 70 nm), but rather associated to the spectral position of the waveguide-induced absorption peak for a given NW diameter.

Effect of Illumination Geometry on the Appearance

One key application of ST-PV is to be used as window components. Given that the illumination geometry changes through the day/year, it is important to address the influence of angle of incident sunlight on the appearance and the PV performance of ST-PV. To evaluate this effect on the NW solar cells, we have performed FDTD simulations under different angles of incidence (θ) of an incoming plane wave onto a GaAs nanowire array stack

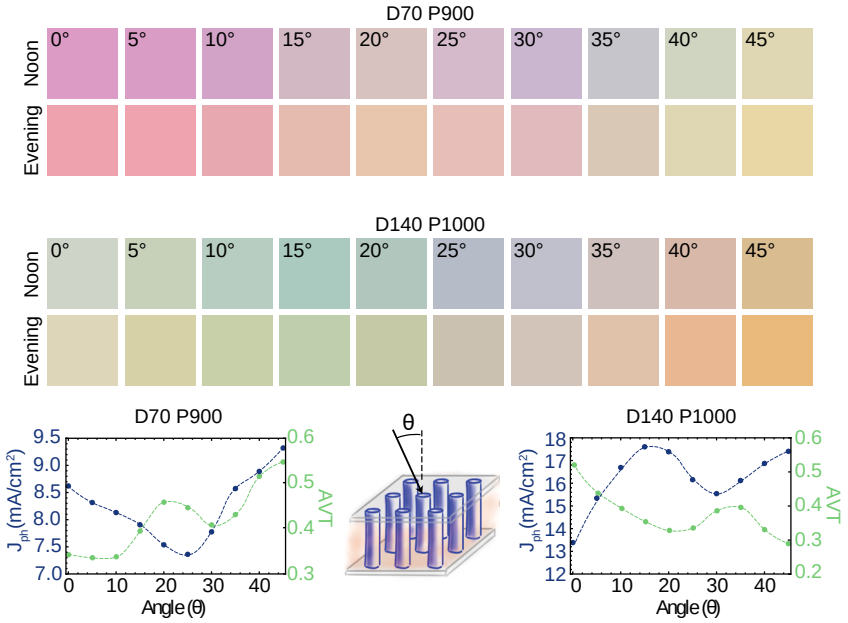

FIGURE 3.6: On top, perceived transmitted colour for two geometries of GaAs NW arrays (diameter 70 and pitch 900 marked as D70 P900, and diameter 140 P1000 marked as D140 P1000) under different incident angle θ from the sun (shown in the sketch). For both cases, the perceived colour is calculated for both the standard daylight spectrum at noon (D65) and the standard evening spectrum. Below, for both geometries J_{ph} and AVT as a function of θ are plotted.

(see the sketch in figure 3.6). We have considered two GaAs NW array configurations as study case, which show very different appearance under standard illumination conditions (i.e. daylight at normal incidence): Array D70 P900 corresponds to nanowires of 70 nm in diameter and 900 nm apart; and array D140 P1000 composed by nanowires of 140 nm in diameter and 1 μm apart. Under standard illumination, array D70 P900 shows a strong pink appearance (AVT $\approx 34\%$), while array B displays as light green with relatively large transparency (AVT $\approx 53\%$).

Apart from changes in the angle of incidence, variations in the relative spectral power distribution of daylight are known to occur, particularly in the ultraviolet spectral region, as a function of season, time of day, and geographic location. Thus, besides the standard noon spectrum (D65)

we have also considered the standard evening spectrum (based on black body radiation at 4000K) and represented the perceived colours in figures 3.6 as a function of angle, under the *Noon* or *Evening* labels, respectively. Interestingly, the appearance of both arrays is relatively similar between noon and evening illumination when the angle of incidence is small ($< 20°$-$30°$) despite the stronger red component in the evening spectrum (see SI). At those small angles the colour hue is fairly stable in both arrays, however for larger angles the change in colour is more abrupt. At large angles and noon illumination, the colour hue shifts from pink to blue to green/yellow in array D70 P900, and from green to blue and orange in array D140 P1000. Such a spectral change with angle may be expected by the allowed resonant excitation of other modes in the NWs. Earlier works have shown that the absorption in NWs is mainly governed by coupling to waveguiding modes up to angles of incidence around $20°$ after which Mie resonances contribute to the absorption [72].

Based on the simulated spectra and the daylight illumination conditions (AM1.5G), we compute the photocurrent and AVT as a function of angle of incidence on the two NW array cells (bottom panels in figure 3.6). It is interesting to see that the transparency of the two array configurations exhibits completely opposite trends with angle of incidence. While the AVT of array D70 P900 steadily increases with angle, the opposite occurs for array D140 P1000. A decrease in transparency and increase in photocurrent with increasing the illumination angle may be expected, as the NW array appears more dense. In fact, a 0.5% increase in conversion efficiency for an illumination angle of 15 degrees for a GaAs vertical NW array has been measured before [111]. However, the AVT behaviour observed in array D70 P900 is surprising. Comparing the absorption spectra versus the incidence angle for these two geometries suggests that the position of the absorption peak at normal incidence determines whether or not the non-zero angles would be beneficial for the PV performance (See the absorption spectra in the SI). For the array D70 P900 the peak in absorption at $\theta = 0$ is positioned inside the visible range. For larger θ however, contributions from Mie modes changes the position of the absorption peaks towards the shorter wavelengths, hence outside of the visible range, which results in higher AVT.

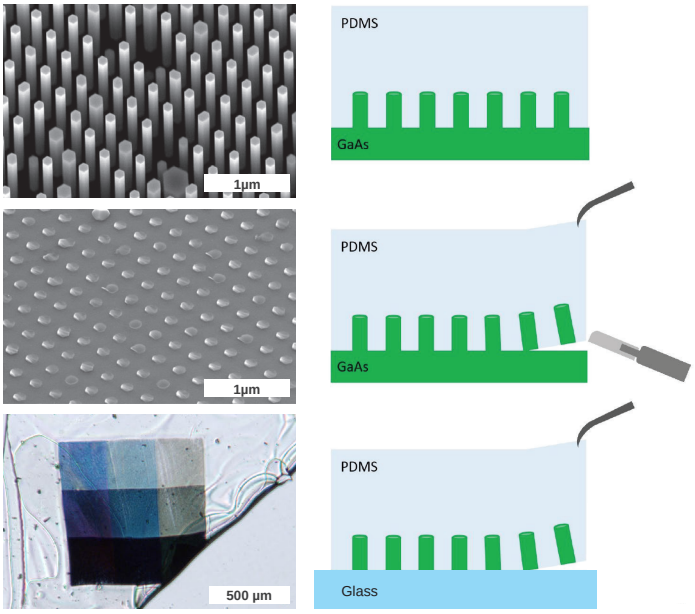

FIGURE 3.7: Right: Sketch showing the steps to prepare NW-polymer composite: embedding the GaAs NW array on GaAs substrate in polymer, cutting and peeling off the NW-polymer composite off the substrate, and placing it on transparent glass holder. Left: SEM image of a GaAs NW array on GaAs substrate, SEM image of the substrate after the NW array is cut and peeled off, and optical image of the nine fields of vertically standing NW arrays inside polymer placed on a clean cover glass.

3.3 Experimental Demonstration

We now describe the fabrication and characterisation of vertical GaAs NW arrays with different diameters and pitch distances as proof of concept. The arrays were grown by metal organic chemical vapor deposition via selective area epitaxy on a pre-patterned GaAs substrate with periodic arrays of holes (hole diameters of 50, 70, 100 nm and pitch distance of 300, 600, 900 nm). The pre-patterning and growth was performed by the group of Prof. Dr. Anna Fontcuberta i Morral at EPFL. The as-grown sample consists of 3×3 fields of 300×300 μm^2 NW arrays, each with different NW diameter and pitch distance. Owing to lateral overgrowth, the actual NW

diameter is larger than that of the openings. The NW diameter distribution for each of the array fields can be found in the SI. Owing to the same growth time in arrays with different NW diameter, the NW length is not the same in all arrays, ranging from 4.5 to 7 μm. Further details on the substrate preparation and NW growth can be found in the SI.

As shown schematically in figure 3.7, self-standing arrays were attained by embedding the NW arrays in a PDMS polymer film and subsequently peeling the composite off from the GaAs substrate. A surgical knife was used to cut the polymer area around the NW fields and then undercut the NWs from their base. The NW-polymer composite was removed with the help of tweezers and was placed on a clean cover glass (more details in the SI). Figure 3.7 shows the SEM images before and after peeled off, where it is clear that the NWs were nicely cleaved near the NW/substrate interface. The optical microscope image of the PDMS-embedded arrays transferred to a glass substrate is also shown, where NW diameter increases from left to right, and pitch distance from bottom to top. From the optical image, one can already discern different colours (from black to purple, blue and green) and degrees of transparency (from what appears like satin glass to fully opaque) offered by the NW arrays in such a small span of geometries.

Optical Characterisation

The optical properties of the NW/PDMS are assessed with confocal microscopy in transmission mode coupled to a spectrometer. The transmission spectra and optical image for six of the nine fields are plotted in figure 3.8a and c, respectively. In figure 3.8c, the top row of arrays (labeled i, ii and iii with increasing NW diameter) corresponds to those with the largest pitch distance (pitch = 900 nm), and thus are more transparent. Oppositely, the bottom row of arrays (labeled as iv, v and vi with increasing diameter) are more dense (pitch = 600 nm) and thus show more vibrant colours as expected from the theory shown in the previous section. The three arrays with the smallest pitch distance were completely opaque and are thus not discussed here. The blue, green and red curves in figure 3.8a correspond to geometries with hole diameters of 50, 70 and 100 nm, respectively. Solid (dashed) lines show the spectrum for the array with pitch distance of 900

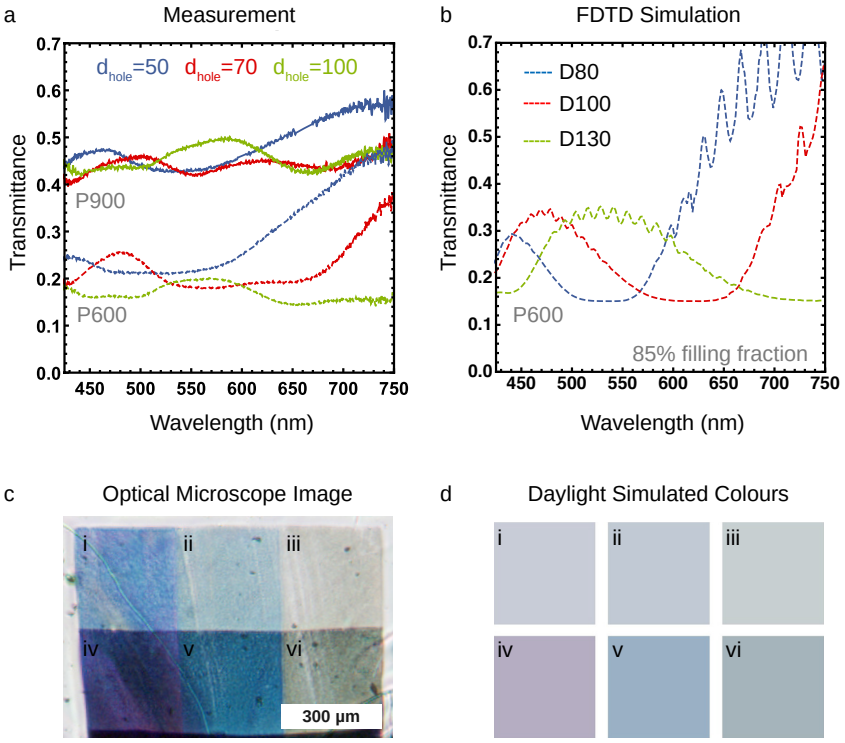

FIGURE 3.8: a) Measured transmittance spectra of six NW array fields with nominal hole diameters of 50, 70, and 100 nm (shown in blue, red and green, respectively), and pitch distances of 600 and 900 nm (shown in solid and dotted lines, respectively). b) FDTD simulated transmittance (1-Absorption-Reflectance) of NW arrays with pitch distance of 600 nm and diameters 80, 100 and 130 nm. The NW absorption has been reduced to 85% to account for the growth/peel-off yield c) Optical image of the six fields: i, ii and iii are with pitch 900 nm, and hole diameters of 50, 70 and 100 nm, respectively. iv, v and vi have pitch of 600 nm and same sequence in hole diameter. d) Perceived colour in transmission as calculated from data in (a). The AVT values for the arrays are i) 44.5%, ii) 43.7%, iii) 47.4%, iv) 23.2%, v) 19.2%, and vi) 18.5%.

nm (600 nm). On average the transmission for the arrays with the largest pitch distance is the highest (with an AVT around 45%).

The three different NW diameters give rise to characteristic spectral features in transmission that are not strongly perturbed by the pitch distance.

Figure 3.8 b shows the simulated transmission spectra for three different NW arrays with diameters of 80, 100 and 130 nm, which are close to the average NW diameter found in the as-grown arrays. For clarity, we only show simulations for one pitch distance (pitch=600 nm). Here, the transmission has been obtained by considering only 85% of the NW-PDMS absorption of a perfect array, as to account for defects and missing NWs in the peeled-off arrays. The measured spectra are in very good qualitative agreement with the simulated ones, with some discrepancies in the absolute strength of the transmission peaks. We attribute these differences to the different NW length, possible parasitic absorption in the PDMS layer and to the fact that the collection of transmitted light is limited by the objective's NA=0.8 in our experiment.

Based on the measured spectra, we have also computed the expected array appearance under daylight and is represented in figure 3.8d. It is interesting to note that the colours are slightly different than those in the optical image, as the microscope lamp spectral distribution differs from that of the Sun. Despite subtle differences and smaller contrast, the daylight simulated colours clearly show a progressive colour change, from purple to green-blue, with increasing diameter.

Appearance Under Angled Incidence

We finally also experimentally show the effect of the angle of incidence on appearance of the arrays. To capture images at different angles of incidence, we use an optical microscopy with tailored 3D printed wedged sample holders with various tilt angles, up to 45° (see figure 3.9-top). The images taken at various incidence angles are shown in figure 3.9-bottom. In agreement with our simulations described in the previous section, we see that the colour appearance is quite robust for small angles, up to about 20°. At already 25°, we observe a gradual change in colour that is most apparent in the arrays with smaller NW diameter (leftmost arrays). For instance, the middle array (average NW diameter of 130 nm, and 900 nm in pitch) appears bright blue for angles up to 20° and then quickly changes to purple for larger angles of incidence. By contrast, the arrays with larger NW diameters (rightmost) appear more robust in colour, where the only the optical density seems to increase with angle. However, as

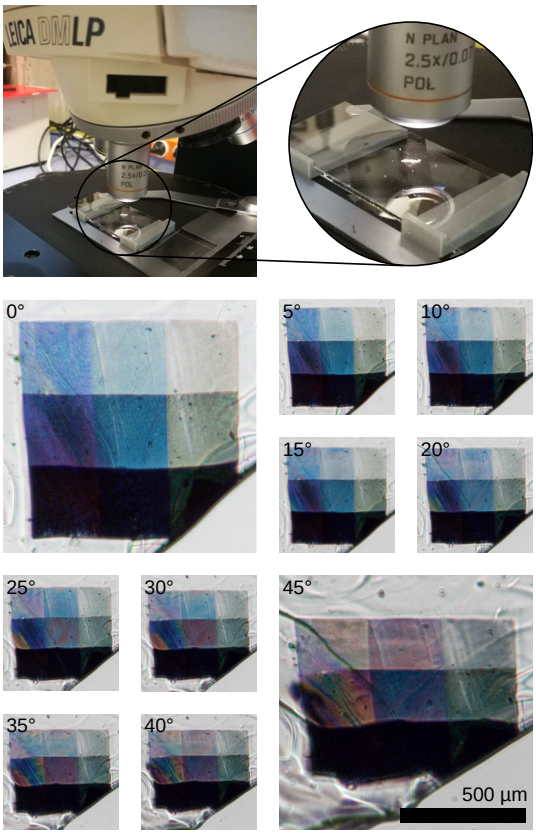

FIGURE 3.9: Top: Leica microscope set-up. In the zoomed-in picture an angled incidence measurement is done using a tailored 3D printed wedged sample holder. Bottom: Optical measurements from nine fields of vertically standing NW arrays embedded in PDMS and placed on a cover glass, under incidence angles of 0 to 45°.

indicated above we suspect the contribution of various NW geometries to the transmission spectrum in these arrays, which may contribute to their robustness in appearance. Introducing multiple NW geometries in a hyperuniform manner to the array may be an interesting additional control knob to design NW-based ST-PV with additional features, such as increased performance or robustness to illumination conditions.

3.4 Conclusions

In this Chapter we explore in detail the potential of semiconductor NW-based solar cells as a powerful and tunable in design approach for wavelength-selective ST solar cells. The unique property of vertically standing NWs -of diameters in the range of hundreds of nanometers- which is efficient coupling of light into waveguiding modes of these nanostructures makes them great nanophotonics-driven tools to control the light in our intended way. FDTD simulations of PMDS-embedded NW arrays confirm that by changing diameter and periodicity one can engineer the absorption and transmission spectra of a solar cell to provide a broad range of bright colours, semi-transparency and high PV performance.

We find that for three common PV materials (Si, GaAs and InP), when photons with energies close to the material's bandgap efficiently couple to a waveguiding mode of the NW, the photocurrent vs AVT is maximised, and outperforms the idealised non-wavelength-selective performance. In fact, the absorption spectra of the arrays under such conditions resemble those of wavelength-selective approaches, with NIR absorption. From simulations under various illumination conditions (angle and spectrum), we find that the colour appearance is quite robust to spectral and small angle changes. For angles larger than $\sim 20^{\circ}$, the arrays show a more abrupt change in colour likely arising from the excitation of Mie resonance modes. Throughout the whole span of illumination angles, the expected photocurrent varies by $\pm 10\%$.

Finally, we experimentally demonstrate the fabrication and colourful optical properties of free standing vertical GaAs NWs by the PDMS-embedding and peeling-off method. Two sets of purple, blue and green arrays with average AVT around 20 and 50%, respectively, are demonstrated. We compare the transmission spectra and perceived transmitted colours to those expected from geometrical considerations. We also show images of the arrays under increasing angle of incidence up to 45°. As predicted by theory, we observe two main regimes: from normal incidence up to 20-30° the colours are kept similar, and for larger angles the colour appearance of the arrays changes. Given the fact that high PV efficiencies have already been demonstrated in opaque NW arrays, this work high-

lights the potential of such nanostructures as new efficient solutions for BIPV.

3.5 Supplementary Information

3.5.1 FDTD Simulations

Finite Difference Time Domain (FDTD) simulations of vertically standing NW arrays were performed with the Lumerical software package. The simulation geometry consisted of cylindrical NWs of 6μm in length, surrounded by PDMS and sandwiched between two layers of indium tin oxide (ITO) films of 100 nm in thickness. The NWs are ordered in a square lattice by using periodic boundary conditions on the x-y boundaries. Perfectly matching layers (PML) are defined at the top and bottom boundaries. The NW diameter is mapped from 50 to 200 nm in steps of 10 nm, and the pitch is changed from 300 to 1000 nm in steps of 50 nm. Each array is excited from the top with a broadband plane wave. The simulation wavelength range was chosen in accordance to the bandgap of each material, where for Si is from 300 to 1100 nm, for GaAs is from 300 to 930 nm, and for InP is from 300 to 1000 nm. The optical constants are taken from Ref. [112]. As for direct bandgap materials it is difficult to obtain a good fit to refractive index data due to the sudden jump in the extinction values, the wavelength range for GaAs and InP is divided in two parts to obtain a good fit to experimental data. The mesh accuracy of the simulation layout is chosen large enough for the cylindrical shape of the NW to be well-preserved while keeping a reasonable simulation time. Simulations were powered by SurfSara, the Dutch national e-infrastructure with the support of SURF Cooperative. Frequency-domain field and power monitors are positioned above the source, and before and after the NW array to respectively record the reflected power and transmitted power before and after the NWs. The recorded value shows what percentage of the optical power injected by the source passed through each monitor. By subtracting the absolute values from the two transmission monitors the fraction of absorbed power for each wavelength is obtained.

3.5.2 Photocurrent Calculation

To calculate J_{ph} the fraction of the absorbed photons for each wavelength is obtained from FDTD simulations. By multiplying the absorption with

AM1.5G solar spectrum N_{ph} the number of absorbed photons at each wavelength is calculated. After integration over all wavelengths, the total number of generated photocarriers is achieved, and by multiplying by the elementary charge of the electron (e) it gives the estimated J_{ph} of our solar cell.

$$J_{ph} = e \int N_{ph}(\lambda)\, abs(\lambda)\, d(\lambda) \tag{3.1}$$

3.5.3 Average Visible Transmittance (AVT) Calculation

Average visible transmittance (AVT) is a measure of visible transparency of the ST solar cell. The recommended calculation approach, which is accepted by window industry is to integrate the transmission spectrum and normalize it to the photopic response of the human eye as such:

$$AVT = \frac{\int T(\lambda)\, P(\lambda)\, S(\lambda)\, d(\lambda)}{\int P(\lambda)\, N_{ph}(\lambda)\, d(\lambda)} \tag{3.2}$$

Where λ is the wavelength of the light, T(λ) is the transmission spectrum (which we obtain from FDTD simulations), $N_{ph}(\lambda)$ is the AM 1.5G solar photon flux and P(λ) is the photopic response of the human eye. The photopic response (sometimes also referred to as y(λ) or V(λ)) is a standard function established by the Commission Internationale de l'Éclairage (CIE) and determines the sensitivity of the human eye to different colours. The CIE photopic standard spectrum of 1978, the most commonly used in window industry, is shown in figure 3.10. The photopic response is a fairly symmetric gaussian-like distribution centered around 555 nm.

3.5.4 Colour Perception Calculation

The chromaticity coordinates (x,y) are calculated from the spectral power distribution of the stimulus and the CIE colour-matching functions (x',y',z') as follows. First, the spectral integration of the colour-matching functions

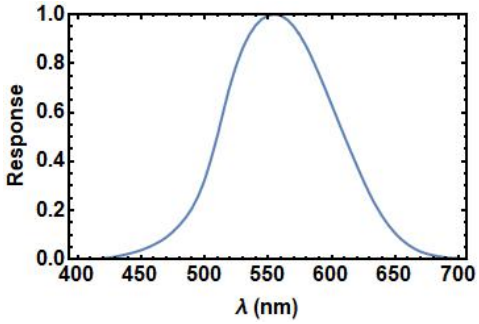

FIGURE 3.10: Photopic response of the human eye.

convoluted with the stimulus function gives rise the tristimuli values X,Y and Z:

$$\begin{aligned} X &= \int s(\lambda)x'(\lambda)d(\lambda) \\ Y &= \int s(\lambda)y'(\lambda)d(\lambda) \\ Z &= \int s(\lambda)z'(\lambda)d(\lambda) \end{aligned} \tag{3.3}$$

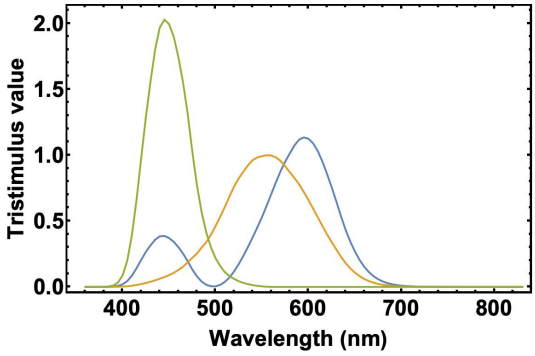

FIGURE 3.11: Colour matching functions as a function of wavelength

The colour matching functions are represented in (Figure 3.11). $s(\lambda)$ is the stimulus function, which is basically the light the eye receives. In our case, we consider two different illumination conditions (Figure 3.12) that are normalised by the transmission spectrum of the NW array. The

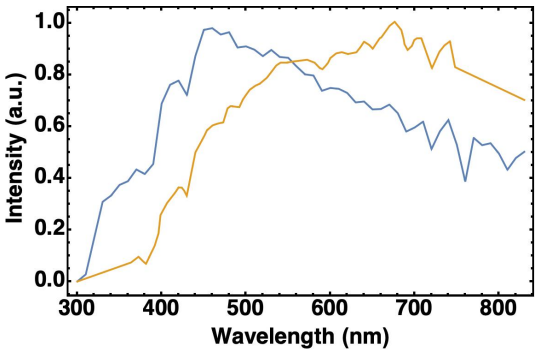

FIGURE 3.12: Relative spectral power distribution for standard daylight (blue) and evening light (orange) illuminations used for our colour calculations. CIE standard illuminant D65 is used to represent average daylight and the blackbody radiation at 4000K is used to represent the evening illumination.

chromaticity coordinates are simply a normalisation of the tristimuli in the form:

$$x = \frac{X}{X+Y+Z}; y = \frac{Y}{X+Y+Z} \tag{3.4}$$

We have used Mathematica software to obtain the chromaticity values, which are used to represent coloured the matrices in Figure 3.4 with the XYZ Colour function.

3.5.5 NW Sample Fabrication

Zn-doped 2-inch GaAs 111B substrates with a thin layer of PECVD grown silicon oxide ($\sim$ 30 nm) were patterned with arrays of holes of different diameters (50, 70, 100 nm) and pitches (300, 600, 900 nm). The patterning process was realized by electron beam lithography followed by dry (reactive ion etching –RIE) and wet etching (buffered hydrofluoric acid—BHF).

Arrays of n-GaAs hexagonal pillars were grown by low pressure (20 mbar) MOVPE using trimethylgallium, arsine and disilane as precursor for Ga, As and Si, respectively, in a N_2 ambient. Prior to the GaAs:Si growth, the patterned substrates were deoxidized during 4 minutes at 870°C under arsine, the decomposition of which results in a H^+ surface treatment. The

epitaxial growth was subsequently carried out at 850°C at a nominal growth rate of ∼46 pm/s (as calibrated separately on a planar, unpatterned GaAs (100) surface). The resulting sample consists of 9 different growth fields of $300 \times 300\ \mu m^2$ each with different hole diameters and pitch distances. The NW length is affected by both hole size and pitch distance. For pitch 900 nm, the length of the wires with increasing diameter are respectively around 6.9, 5.7, and 4.5 μm. The measured NW size distribution is shown in Figure 3.13.

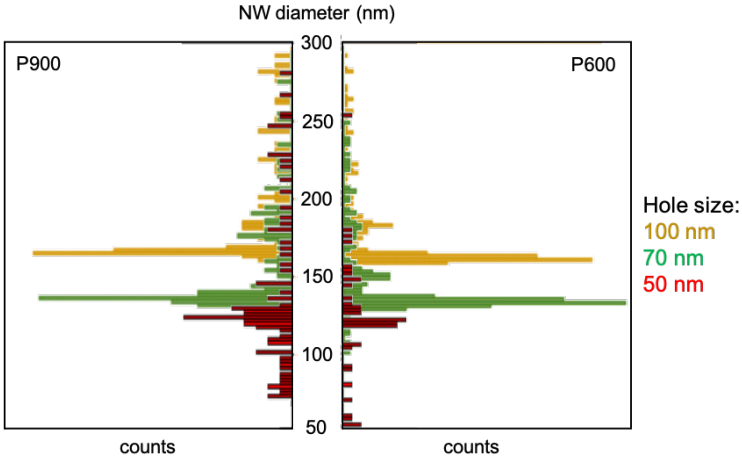

FIGURE 3.13: GaAs NW diameter distribution for different hole openings and pitch distances. Values are obtained from image processing of SEM pictures.

After growth, the NWs were peeled off from their substrate as follows. First, the as-grown sample was spin-coated with polydimethylsiloxane (PDMS). After spin-coating, the sample was placed in the oven for 24 hours at 50°C followed by at least another 24 hours outside of the oven for complete curing of the PDMS. For the peel off, a small square framing all the NW fields was cut in the PDMS with a surgical knife. Then, the same knife was used to undercut the NW fields from their base and to lift the NWs - PDMS composite from the GaAs substrate. The composite was removed with the help of tweezers and was placed on a clean cover glass slip. If wrinkles are formed or to adjust the position of the composite on the new support, acetone was used.

3.5.6 Optical Characterisation

WITec alpha300 RS confocal microscopy setup was used in transmission mode with a 100x (Zeiss EC Epiplan Neofluor, NA 0.9, WD 0.28mm) and 60x (Nikon Achromat, NA 0.8, WD 0.3mm) magnification, air objectives, for top and bottom respectively. The samples were illuminated using the integrated LED illumination and spectra were collected using the fiber-connected WITec UHTS spectrometer, where the collection by the fiber acts as the confocal pinhole.

For imaging, a Leica DM-LP microscope was used in transmission mode. An incandescent lamp is used as the light source and the transmitted light is captured by a 20x air objective. The image is captured with Basler Aca1920-40gc camera without any post treatment. For the images taken under different angles, home-made 3D-printed wedged sample supports are used.

3.5.7 Geometry Dependent Photocurrent vs AVT for Si and InP

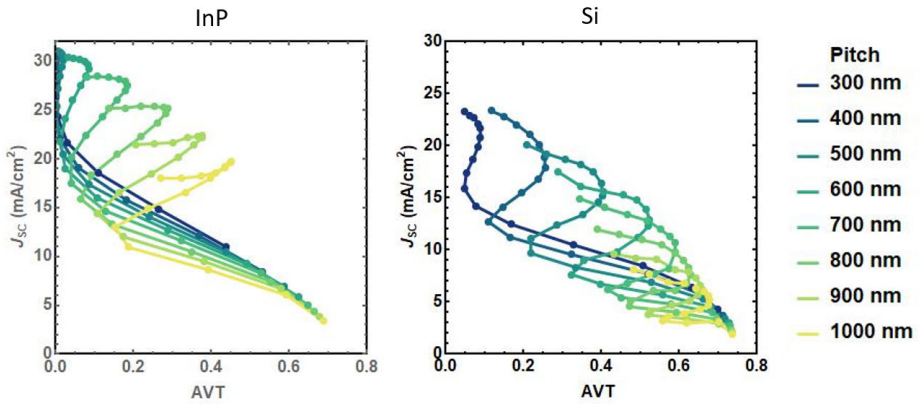

FIGURE 3.14: Simulated photocurrent vs AVT for different NW arrays based on InP (left) and Si (right). From blue to green, the colour indicates the array pitch distance from 300 to 1000 nm, respectively. The NW diameter is increased from 50 to 200 nm, from right-most datapoints to the left. The z-shape described in the text is less obvious for Si, owing to the indirect nature of its bandgap.

3.5.8 Chromaticity Plots for GaAs and InP

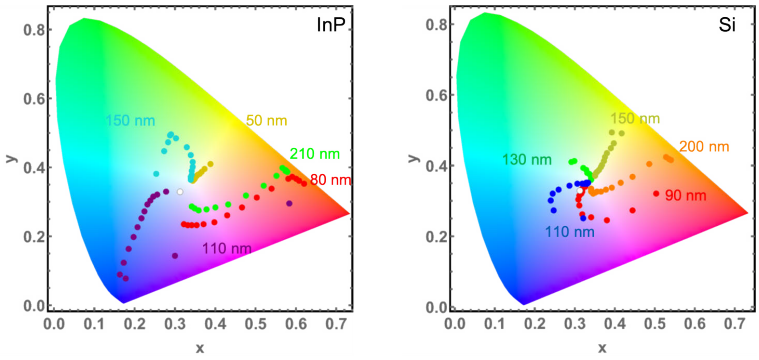

FIGURE 3.15: Chromaticity plots for the colour appearance in transmission for different NW arrays based on InP (left) and Si (right). The colour of datapoints indicates the NW diameter and the pitch distance increases from 300 to 1000 nm from outer-most datapoints towards the center of the chromaticity diagram.

The central area of this plot is the area all different white point from different light sources fall into. Thus, the closer to the center the appearance in transmission is, the more transparent. As expected, with increasing the pitch, data points for all diameters move from outside edges of the chromaticity plot towards inside. We observe that for some diameters the hue stays more or less the same but for some other the hue changes quite a bit with the change in pitch. Such changes are softer in the case of Si compared to GaAs and InP, owing to its indirect bandgap nature.

3.5.9 Interplay Between Waveguiding and Mie Resonances in the Absorption Spectra

Figures 3.16a and b show the absorption spectra for GaAs NW array with diameter 70 nm pitch 900 nm, and diameter 140 nm pitch 1000 nm, respectively, with length of 6 μm and pitch 900 nm. Different colours are for different angles of incident light. As we see, the peak at 510 nm which corresponds to light coupling to the first waveguiding mode is very present for the normal incidence. However, by increasing the angle of incidence the light coupling efficiency decreases. From 20 to 25 degrees, however,

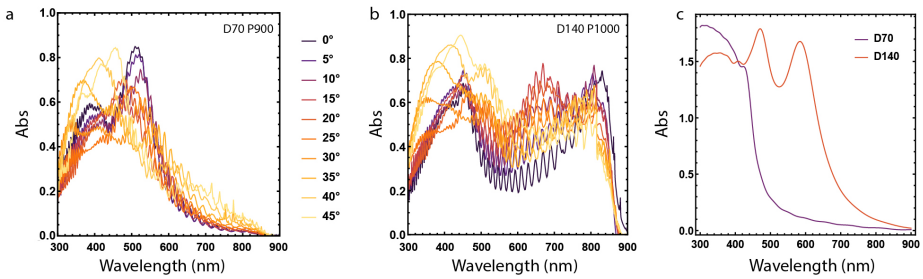

FIGURE 3.16: Absorption spectra of GaAs NW array of 6-μm length and a) diameter 70 and pitch 900 nm and b) diameter 140 and pitch 1000 nm. Different angles of incidence are shown in different colours, indicated in the legend. c) Absorption cross-section of Mie resonators with diameters 70 and 140 nm is plotted, for comparison.

there is another peak emerging at the lower wavelength range (between 300 nm and 400 nm) in the case of 70 nm NWs. Similarly, for NWs of 140 nm in diameter, additional absorption peaks appear in the green (500 nm). We assign this new spectral feature to excitation of Mie modes inside the NW. The Mie absorption for GaAs spheres of diameters 70 nm and 140 nm inside PDMS are plotted in figure 3.16c for comparison. The absorption cross-section of the Mie resonators shows similar spectral features to those appearing in the NWs with tilted illumination.

CHAPTER 4

Over 65% Sunlight Absorption in a 1 μm Si Slab with Hyperuniform Texture

Thin, light-weight and flexible solar cells will be an inevitable technology in the near future. Ultra-thin crystalline silicon (c-Si) cells capitalise on the success of bulk silicon cells while being light-weight and mechanically flexible, but suffer from poor absorption and efficiency. Here we present a new family of surface texturing, based on correlated disordered hyperuniform patterns, capable of efficiently coupling the incident spectrum into the silicon slab optical modes. We experimentally demonstrate 66.5% solar light absorption in free-standing 1 μm c-Si layers by hyperuniform nanostructuring. The absorption equivalent photocurrent derived from our measurements is 26.3 mA/cm^2, which is far above the highest found in literature for Si of similar thickness. Considering state-of-the-art Si PV technologies, the enhanced light trapping translates to a record efficiency above 15%. The light absorption can potentially be increased up to 33.8 mA/cm^2 by incorporating a back-reflector and improved anti-reflection, for which we estimate a photovoltaic efficiency above 21% for 1 μm thick Si cells.

4.1 Introduction

Micrometer-thick silicon photovoltaics (PV) promises to be the ultimate cost-effective, reliable and environmentally-friendly solution to harness solar power in urban areas and space, as it combines the low cost and maturity of crystalline silicon (c-Si) manufacturing [113] with the low weight and mechanical flexibility of thin films [114–116]. Efficient light trapping in ultra-thin c-Si is of utmost importance when the film is thinner than the absorption length. Indeed, due to the indirect bandgap of c-Si, inefficient absorption currently hampers the thinning of Si cells below $\sim$ 100 μm, which is crucial to enable flexible, light weight and lower cost c-Si PV [113, 117, 118]. 3D nanophotonic architectures are crucial for reducing the cell thickness as conventional anti-reflection coatings and multilayers can only prevent light reflection via impedance matching of the solar cell and air, but do not extend the light paths in the Si cell that are required for efficient photon absorption [119]. Despite the fact that many works have focused on nanophotonic principles for enhancing light absorption, there is still no unanimously agreed best strategy for the designing of light trapping nano-textures for PV. Periodic patterning of a thin slab, whether by adding plasmonic [120–124] or dielectric [125–127] structures, can reduce reflection and simultaneously scatter light in the plane of the thin film, but generally work only at discrete wavelengths and specific angle of incidence, due to the discrete crystal momenta of gratings. Oppositely, disordered patterns, such as Asahi roughening or random pyramid etching, scatter the light over a broad angular range and over a large range of wavelengths due to the large rotational and translational symmetry, but are not tailored to match the thin film architecture [128].

Recently, correlated disordered media have been shown to outperform random roughening and periodic patterning for light trapping [129–138]. Albeit many designs have been presented so far, it is still an open question what the best design is and whether the optimal one has already been achieved. For instance, it is not settled if the best result is obtained when starting the optimisation from a periodic or from a random structure. In contrast to these heuristic optimisation methods, hyperuniformity has recently emerged as a new framework to engineer light scattering and diffraction in a rational manner. Hyperuniform disordered (HUD) media are statis-

tically isotropic and possess a constrained randomness such that density fluctuations on large scales behave more like those of ordered solids, rather than those of conventional amorphous materials [139–142]. HUD patterns naturally arise in many physical systems, from the mass distribution in the early universe [143], structure of prime numbers [144], hydrodynamics [145], structure of amorphous ices [146], sheared sedimenting suspensions [147], to wave localisation [148] or colloidal packing [149]. When translated into photonic materials, HUDs exhibit large and robust photonic band gaps as in photonic crystals, but are both complete and isotropic [142]. As a result, HUDs display allowed modes that can propagate through the structure in an isotropic fashion as in random media. HUDs are a highly flexible platform to control light transport, emission and absorption in unique ways, beyond the constraints imposed by conventional photonic architectures [150–154], for the design of freeform waveguides [155], high-quality factor resonant defects and arbitrarily high-order power splitters [156, 157], hollow-core fibers [158] and photonic bandgap polarizers [159] among others.

In this Chapter we experimentally demonstrate that light absorption in a $1\ \mu$m-thick silicon slab is enhanced more than twofold in the wavelength range from 400 to 1050 nm when textured with optimised HUD-based patterns compared to the unpatterned slab. The resulting absorption is the highest demonstrated so far in a Si slab as thin as 1μm. This record value is achieved by k-space engineering of HUD patterns with a tailored scattering spectrum and diffractive coupling of solar irradiation into guided modes of the Si slab. Using our strategy to light management, we investigate PV efficiency by focusing on the trade-off between light trapping and increased carrier recombination given by the nanotextures. We find that the effect of increased surface-induced charge carrier recombination on the open circuit potential can be fully compensated by the large photo-currents. A detailed PV efficiency estimation reveals that efficiencies above 20% can be obtained for several optimised HUD designs and state-of-the-art Si PV technologies. This is a highly remarkable efficiency for such a thin indirect-bandgap material, which together with the fact that lower grade raw Si material can be used in such thin devices, establishes a new breakthrough in thin light-weight and flexible solar cells.

4.2 Light Absorption in Films with Disordered Hyperuniform Patterns

We demonstrate the power of hyperuniform disordered (HUD) patterns for lightweight, flexible and efficient photovoltaics, by first focusing on the absorption properties in ultra-thin (~ 1 μm) Si. The proposed structure for the highly efficient Si light absorber is shown in figure 4.1a. It consists of a thin Si slab (1 μm), of which the top 200 nm is patterned with an optimised HUD pattern. In this case, the pattern consists of a 2D network of Si walls, that resembles the honey-comb underlying structure in black butterfly wings [136, 160]. The Si pattern is infiltrated with a low refractive index medium by spin coating a polymer resist [161] with refractive index of 1.52. While the infiltrated pattern layer is expected to also reduce reflectance due to the better index matching with air ($n_{pattern} \approx n_{Si} \cdot f + n_{LRM}(1-f)$, with f being the Si filling fraction), an additional layer of resist on top ($50-100$ nm thick) further improves anti-reflectance, referred to as ARC. While the optical properties of the resist are not the ideal to guarantee minimal reflection, spin coating is a simple conformal fabrication method that ensures nanopattern filling and a flat top surface.

Figure 4.1b is a photograph of a suspended 4.8×4.8 mm^2 Si membrane nominally 1 μm-thick on a Si support frame before spin coating the resist. The membrane reveals a semi-transparent reddish colour owing to its small thickness and small absorption coefficient in the red and near infrared. HUD-based patterns were fabricated on the membrane with e-beam lithography in at least 100×100 μm^2 areas. These areas are clearly visible in the picture as they appear darker, highlighting the increased light trapping. A close-up scanning electron microscopy (SEM) image of the fabricated HUD network pattern on the Si suspended membrane is shown as inset. Due to the small thickness of the Si membrane, edge smearing effects typically observed in e-beam lithography on thick insulating wafers are reduced and very sharp features can be fabricated.

We have measured the light absorption of the free-standing membrane with ARC on the unpatterned and patterned regions by using an integrating sphere microscope [162, 163]. The curves in figure 4.1c compare the light absorption as measured for the flat membrane with that of the

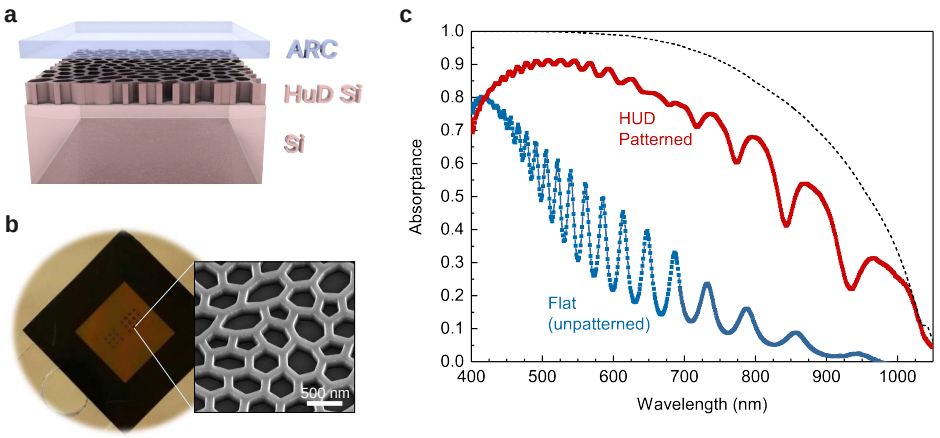

FIGURE 4.1: Ultra-thin light absorber design. a) Schematic representation of the ultra-thin light absorber consisting of a 1 μm-thick silicon film with the HUD pattern on the top surface (~ 200 nm thick) to improve light trapping. The pattern is infiltrated with a lower refractive index material (n_{LRM}), which is also used in a top flat layer, ARC, to reduce reflectance (50-100 nm in thickness). Note that the ARC layer is depicted floating above the nanopattern in the image only for clarity purposes. b) Optical image of the silicon membrane sample supported by a thick silicon frame (1×1 cm^2), where the textures have been fabricated. Inset: Scanning electron image of the as-fabricated Si membrane with the optimized honeycomb-like HUD network pattern. c) Absorptance spectra measured for the Si membrane with (red) and without (blue) the HUD pattern with ARC. The membrane is suspended in air and infiltrated with a polymer resist ($n_{LRM} = 1.52$) as ARC. The dashed black line corresponds to the Lambertian limit absorption for 1 μm Si, based on the optical properties given in Ref. [112].

HUD patterned membrane. The absorption spectrum of the flat membrane shows the characteristic Fabry-Pérot interferences for a 1.18 μm thick Si slab (see SI), with a peak in absorption at about a wavelength of 450 nm and rapidly decreasing absorption for longer wavelengths due to the small absorption coefficient of Si in the visible and near infra-red. In contrast, the absorption in the membrane with the HUD pattern is on average 50% higher in absolute numbers for the wavelength range of 500 to 900 nm and it follows the Lambertian limit trend ($4n^2$ limit for 1 μm-thick Si represented by the black dashed curve), which does not take into account reflection losses. Despite the fact that the membrane sits in air (i.e. no back-reflector) and the sub-optimised ARC, the fraction of absorbed solar photons in the

membrane increases from 25.5% to 66.5% by texturing the surface based on our optimised HUD design. This is the highest demonstrated absorption in a 1 μm Si absorber so far, and translates to a photocurrent of 26.3 mA/cm^2, far above the 19.72 mA/cm^2 in the best reported cell with similar thickness [164]. Simulations show that a metal back reflector will increase absorption even further for the whole spectrum and integrated absorption can reach up to 93.4% of the Lambertian absorption. In the following, we describe the design principle and physical mechanism that induces this record in absorption.

4.3 Light Trapping Mechanism and Design Optimisation

As in previous works that use periodic and heuristic aperiodic structures to promote light trapping, the main mechanism by which the HUD nanostructure enhances absorption is diffraction into the absorber [129, 165, 166]. In the presence of texturing, the guided modes of the thin silicon slab become leaky (quasi-guided) and can in- and out-couple to the incoming electromagnetic modes supported by the surrounding medium. The waveguide mode dispersion for a Si slab is shown in figure 4.2a, where we note that within the spectral region of interest, c-Si exhibits strong dispersion that leads to a strong curvature of the Si light cone and significantly different absorption of the guided modes, as indicated by the colour scale in figure 4.2a. The total absorption is obtained by summing up the coupling contributions of each mode. To maximize sunlight absorption in the slab we need to couple efficiently to the lossy modes for a broad range of wavelengths (from 350 nm to 1100 nm). Due to the large number of modes in a 1 μm Si slab, a pattern structure that diffracts normal incident light ($k_{\|} = 0$) to the range of $k_{\|}$ from ~ 15 to ~ 20 μm^{-1} (indicated by the two horizontal dashed lines in figure 4.2a) ensures all sunlight has a mode to couple to. However, due to the inhomogeneous absorption of the guided modes, coupled-mode theory calculations estimate that the highest absorption is actually given for uniform diffraction to the k-range from ~ 9 to ~ 25 μm^{-1} (see the detailed calculation in the SI). Targeting this wave vector range is a key design goal for engineering the diffraction pattern.

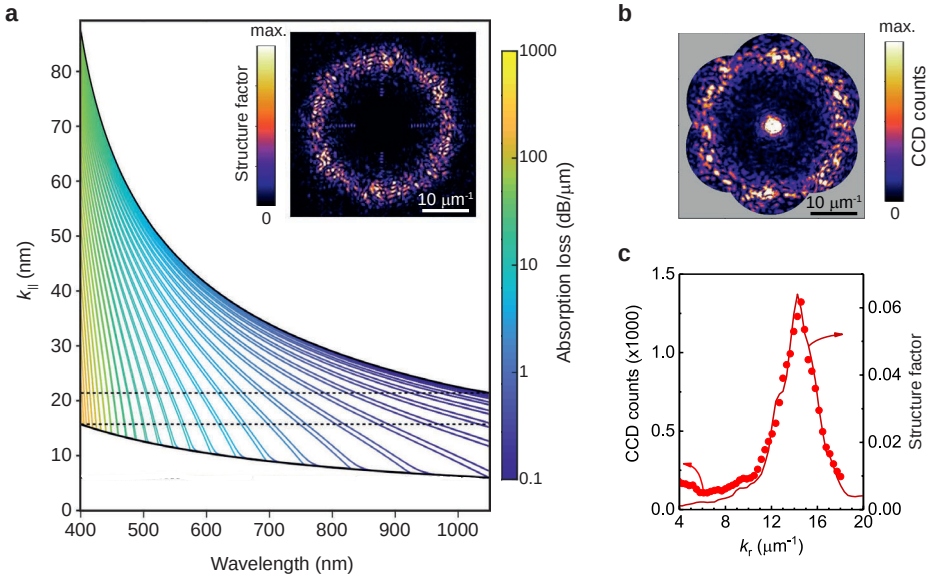

FIGURE 4.2: Light trapping mechanism. a) Waveguide modes for a homogeneous 1μm thick Si slab between air and a perfect metal for the wavelength range of interest in a solar cell. The modes are all lossy, with the absorption loss denoted by their colour, as shown in the colour bar. Black lines denote the dispersion curves for air (lower curve) and for Si (upper curve). The horizontal dashed lines denote two characteristic wavenumbers: $k_1 = 15.71$, and $k_2 = 21.41$ μm^{-1} as described in the text. Inset: Simulated first order diffraction pattern of the HUD network design that shows a characteristic diffraction ring in the desired k-space. b) Measured Fourier-space diffraction pattern in reflection of the *HUD network* design lithographically patterned in a Si wafer (wavelength 561 nm). c) Structure factor based on the radial distribution of the diffraction intensity in (a) and (b).

In contrast to periodic and random patterns, hyperuniform designs with correlated disorder are an intermediate concept that allows the creation of diffraction into only a tailored range of wavevectors. In particular, stealthy HUD structures offer a distinctive route to filling desired bands in Fourier space, intermediate between the continuous k-space content of random patterns, and the discrete crystal momenta of periodic point patterns. Stealthy HUD point patterns are isotropic with no diffraction below a certain critical wavevector value, k_C: $S(k_{\|} \leq k_C) = 0$). The so-called stealthiness parameter χ is defined as the fraction of wavevectors

for which the structure factor vanishes and can be used to measure the hyperuniform correlations. Thus, $\chi = 0$ for purely uncorrelated (Gaussian) point patterns and $\chi > 0.77$ for periodic structures [140, 148, 150, 154].

Our design approach starts with a 2D HUD point pattern ($\chi \sim 0.4 - 0.5$) that provides the most uniform filling in the Fourier space domain delimited by the two wavenumbers ($k_{\parallel,1}$ and $k_{\parallel,2}$) estimated from the waveguide properties of the slab (see SI for more details). Once the 2D HUD point pattern is created, it is transformed into a physical 3D design that can be fabricated with two material components: Si and a low refractive index material. In this case, the 2D HUD point pattern is decorated with 200 nm tall Si walls following a Delaunay tesselation protocol [150] that form a continuous Si network, and the voids are filled by the low refractive index material. However, with this design light absorption is no longer expected to be optimal as the 3D texture strongly disrupts the waveguide properties of the Si slab. Also, the tesselation protocol causes the resulting 3D network to become nearly hyperuniform as it slightly deviates from hyperuniformity constraint [167], (its structure factor may display a small but non-vanishing amplitude for $k_{\parallel} < k_c$.

To resolve this non-ideality, we introduce a second optimisation step to fine-tune the HUD-based 3D pattern, where the HUD properties (average distance between points) and Si filling fraction are optimised. This is done with full-wave 3D numerical simulations that compute light absorption at each optimisation step (see Methods and SI). While the process is computationally expensive, the initial 2D HUD optimisation procedure sets a good base to rapidly find a local maximum. As a result, we obtain an optimised 3D structure based on a 2D HUD point pattern, but with a structure factor function that may differ from what was initially estimated from the slab waveguiding properties. The inset in figure 4.2a shows the 2D simulated structure factor of the fully optimised HUD network design that was used to create the sample in figure 4.1. The structure factor for the first order diffraction shows a clear fingerprint of the hyperuniformity with a circular region around $k_{\parallel} = 0$ where $S(k)$ vanishes, but there is not a sharp cut-off as initially imposed. The nearly-hyperuniform structure factor is better discerned in the angle-averaged structure factor (solid curve) shown in figure 4.2c. Notice that the Fourier space in the optimised pattern is filled in

the wavevector region between 12 and 17 μm^{-1}, which is slightly different than the initial guess for $k_{\parallel,1}$ and $k_{\parallel,2}$.

We have performed momentum spectroscopy of the fabricated pattern on a Si surface, where the measured k-space diffraction pattern in reflection is shown in figure 4.2b as obtained using high-NA Fourier microscopy [168]. By construction the HUD pattern is designed to scatter normally incident light to parallel wave vectors that are *outside* the collection NA of air objectives. However, by combining strongly off normal illumination at six azimuthal angles we can reconstruct the structure factor in 2D Fourier space up to an effective NA almost twice higher than that of the objective lens (see full details in the Methods section). The angle resolved diffraction measured in reflection displays a similar fingerprint of the hyperuniformity as the 2D structure factor of the design. The measured angle-averaged reflection is also plotted in figure 4.2c, and is extremely well reproduced by the theoretical structure factor (solid line).

4.4 Comparison of HUD-Based Designs

So far, we have shown that a 2D HUD point pattern can lead to a highly efficient 3D design for broadband light trapping in a thin Si slab, by *decorating* the point pattern with two materials in a wall network fashion (figure 4.1b). However, there are many other decorating possibilities for the same initial 2D HUD pattern. For instance, instead of the wall network, one could place Si nano-holes at the points of the 2D HUD point pattern and fill the voids with ARC. This is the simplest HUD design, where a single element is cloned at tailored positions. We refer to this texture as *HUD hole*, and the SEM image of the as-fabricated sample is shown in figure 4.3a. Similar to the *HUD network* in figure 4.1, the Fourier microscopy intensity map, figure 4.3(b,top), indicates the HUD nature of the the design and it is very similar to the theoretical structure factor, figure 4.3(c,top).

Another very different way of obtaining 3D HUD patterns is inspired by the generation of *spinodal* structures [169, 170]. Here the mathematical recipe is to first define a random superposition of cosine waves with random phase, with wave vectors imposed by the desired wave vector dis-

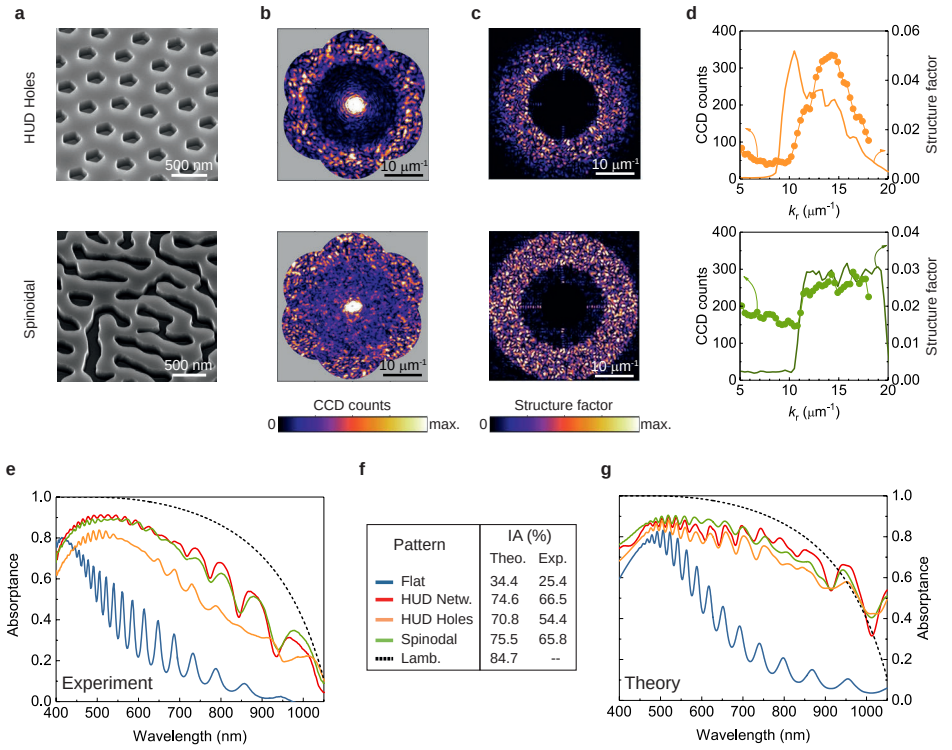

FIGURE 4.3: Performance comparison between different HUD-based designs. a) SEM images of samples textured with the *HUD hole* (top) and *spinodal* (bottom) designs. b) Measured angle-resolved diffraction in reflection of the corresponding pattern. c) Simulated 2D structure factor for the optimised *spinodal* and *HUD hole* patterns. d) Structure factor as a function of in-plane wavevector (k_r) given by the angle-averaged simulated (solid curve) and measured (dots) diffraction. Measured (e) and calculated (g) absorptance spectra for a 1μm thick Si slab suspended in air with the different surface nanopattern designs with ARC considered. The absorption spectrum for the *HUD network* design is the same as in figure 4.1.The theoretical Lambertian limit and the absorption for a flat Si slab (with an ARC) are shown as reference. f) Table listing the percentage of integrated absorbed solar photons (IA) for all patterns for the wavelength range of $400 - 1050$ nm. These numbers are obtained by integrating the theoretical or experimental absorption spectra over the solar flux (AM1.5G) and normalising for the total photon flux in the specified wavelength range.

tribution ($k_{\parallel,1} \leq k_{\parallel} \leq k_{\parallel,2}$), or structure factor. Thresholding the resulting function at a fixed height value defines material boundaries separating Si and low refractive index material (filling fraction f set by threshold choice), tracing out zebra-like patterns as in figure 4.3(a, bottom). The resulting two-phase material pattern is nearly hyperuniform, for which its structure factor is dominated by the wave vector distribution imposed at the initial design stage. Owing to its inspiration, we refer to this design as *spinodal*. Fourier microscopy of the as-fabricated *spinodal* design, figure 4.3(b, bottom), also exhibits a characteristic low scattering at small wavevectors, and a marked increase of scattering at $k_{\parallel} \sim 11\ \mu\text{m}^{-1}$. The contrast is lower compared to the other HUD designs and the scattering at small wavevectors is not expected from the theoretical structure factor, figure 4.3(c, bottom). We suspect the additional scattering at low wavevectors arises from fabrication imperfections.

The azimuthally-averaged k-space resolved diffraction and theoretical structure factor for the *HUD holes* and *spinodal* designs are shown in figure 4.3d as dots and solid lines, respectively. While the intensity distribution in the structure factor of the *HUD holes* is similar in shape to that of the *HUD network* pattern with a peak at $\approx 15\ \mu\text{m}^{-1}$, the structure factor of the *spinodal* is quite different and resembles a square function. All three proposed designs have a structure factor that is well suited to couple normally incident sunlight into the plane for absorption. The theoretical and experimental absorption spectra for the patterned and unpatterned suspended membranes are shown in figure 4.3e and g, where the ARC (same parameters for all designs) is also taken into account. The spectrum for the *HUD network* pattern is also included and it is the same as in figure 4.1c. As a quantitative measure to compare absorption between all the different designs, we have computed the fraction of absorbed solar photons (integrated absorption, IA), as listed in the table in figure 4.3f. The IA, is computed by considering the AM1.5G solar spectrum for the wavelength range of 400 to 1050 nm (see the Methods section for more details). For comparison, we also plot the Lambertian limit obtained by considering the same optical constants used in the full-wave simulations. Similar to the spectra measured in the *HUD network* patterned membrane (red curve), the two new designs raise light absorption in the long wavelength regime, particularly in the case of the *spinodal* (green curve). As expected from the absorption spectra, the *spinodal* and *HUD network* patterns result in a similar IA ($\sim 66\%$ in practice

and $\sim 75\%$ in theory). As also predicted by theory, the *HUD holes* design leads to a slightly lower absorption and IA ($\sim 54\%$ in practice and $\sim 70\%$ in theory). The discrepancy between theory and experiment may arise from the different end-shape of the holes (hexagonal instead of circular), local deviations in the ARC and/or membrane thickness. In any case, for all three designs the measured IA is more than twice that of the unpatterned membrane and we experimentally demonstrate for the first time and for two patterns that absorption is as high as $\sim 78\%$ of the Lambertian limit.

4.5 Full Device Design and Efficiency Estimation

So far, we have demonstrated the exceptional light trapping properties of the HUD patterns in thin Si, as evidenced by the enhanced absorption. However, in a full solar cell device one must also consider other effects of nanotexturing on its performance. It is important to assure that the gain from light trapping for PV remains despite the potential penalty of increased surface recombination, which can strongly affect the performance of devices with a Si thickness smaller than ~ 90 μm, where bulk-related losses are negligible [113, 117, 118]. In order to understand the effects of our HUD-based designs on the PV efficiency, we consider the full device structure shown in figure 4.4a. Now, the patterned Si film sits on top of a silver metal contact that also acts as a back reflector. By using interdigitated macroscopic Ag pads, both the n and p contacts are placed at the rear which reduces shading on the front of the cell. This technology, known as interdigitated back contact (IBC) photovoltaics, has enabled the highest PV efficiency in Si-based cells [171–173]. For simplicity, in our absorption calculations we consider a continuous Ag film at the back instead of the interdigitated pads, which is a fair assumption for optical purposes given their large characteristic sizes.

We have re-optimised the 3D pattern design taking into account the Ag back-reflector as part of the full structure. We also consider an improved ARC configuration, with $n_{LRM} = 1.82$ and ARC thickness of 72 nm (see SI). The resulting absorption spectra for all the different designs are shown in the SI. As expected, the metal back-reflector and improved anti-reflection increases light absorption as compared to that shown in figure 4.3g. Inter-

estingly, the three designs offer a highly robust absorption to changes in the angle of incoming light (see the angle dependent absorption spectra in the SI file), which strongly enhances the daily PV power output.

We have computed the photocurrent, J_{ph}, by integrating the simulated absorbed solar spectrum for the wavelength range of 300 to 1050 nm. To estimate the PV efficiency of our designs we have simulated the current-voltage characteristics of the solar cell with the PC1D software, where we have considered J_{ph} as input and a bulk lifetime of 0.5 ms (standard PV grade Si) and surface recombination velocity (SRV) of 100 cm/s. The

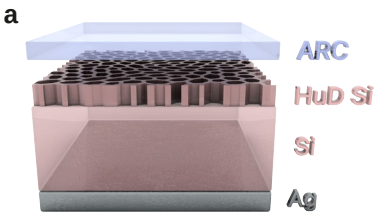

b

	J_{SC} (mA/cm²)	V_{OC} (mV)	η (%)
Unpatterned	18.4	769	12.1
HUD Network	32.7	755	21.1
HUD Holes	32.4	770	21.2
Spinodal	33.8	764	22.1
Best Si cell (165 μm thick)	42.2	744	26.3*

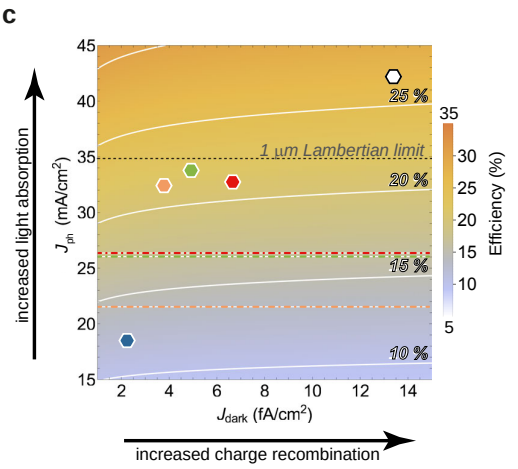

FIGURE 4.4: PV efficiency estimation. a) Full solar cell device design, which includes a Ag back-contact and improved ARC ($n_{LRM} = 1.82$ and 72 nm thick). b) Table summarising the estimated PV performance parameters from our optical and PC1D device simulations. c) Colour-map indicating the non-linear dependence of the maximum PV efficiency on the dark and photo-currents (J_{dark} and J_{ph}, respectively). The white lines are isolines at the efficiency indicated by the labels. The dashed black line corresponds to the J_{ph} given by the Lambertian limit in a 1 μm-thick Si slab. The dash-dotted lines correspond to the J_{ph} derived from our absorption measurements without back-reflector. The data points correspond to the estimated PC1D efficiencies for the different designs. The efficiency estimated for the unpatterned Si membrane and that for the best demonstrated bulk Si cell are shown for comparison. The total efficiency is not only affected by increased light trapping, but also by the additional pattern-induced surface area recombination, reflected in the increased dark current.

SRV value is the state-of-the-art in high efficiency Si solar cell devices [113, 171]. In order to account for the pattern-induced increased surface area, we have considered an effective SRV by multiplying it by the surface area increase factor. A more detailed description of the parameters used in our simulations is given in the SI. The table in figure 4.4b summarizes the estimated solar cell performance, in terms of short circuit current (J_{SC}), open circuit potential (V_{OC}) and PV efficiency (η), for the optimised *HUD hole*, *HUD network* and *spinodal* patterns. For comparison, we have included the theoretical case of an unpatterned Si membrane (with ARC) and the current record Si cell, which is 165 μm thick [171].

Because we assume no external resistance losses, $J_{SC} = J_{photo}$. With the pattern-induced light trapping, the J_{SC} in 1μm-thick Si is almost doubled for all three designs compared to the unpatterned cell (from 18.5 mA/cm^2 to 33 mA/cm^2), close to the Lambertian value for 1 μm-thick Si (at 35 mA/cm^2). At the same time, the estimated V_{OC} values in our three designs are higher than the best bulk cell and oscillate around that expected in an unpatterned thin film. Because of the small volume in a 1μm film compared to bulk, the saturated dark current, J_{dark}, in the cell is only limited by surface recombination. Considering the state-of-the art bulk carrier lifetime and surface recombination velocity, J_{dark} is almost one order of magnitude smaller in a 1μm Si film compared to Si bulk (165 μm thick) and thus the V_{OC} is improved by thinning Si down [113, 117, 174]. An interesting consequence of this is that lower grade Si material can thus be used in such thin devices, which have much lower costs (see the SI for more details on how the PV efficiency is affected by the bulk lifetime and surface recombination). As V_{OC} also depends on the photocurrent, J_{ph}, light trapping has the potential to compensate the effects of patterning-induced larger J_{dark} on the voltage. We find that, the *HUD holes* design uses the smallest surface area and the strong light trapping fully compensates the effect of increased surface recombination and leads to the same V_{OC} as in the unpatterned case.

From the PC1D full current-voltage characteristics we obtain the PV efficiency. Despite the different light trapping power and texture design in all three 1 μm-thick Si patterned cells, we estimate their solar cell efficiency to break the 20% milestone. Figure 4.4c represents the two major consequences of nanotexturing, increased light trapping and increased

charge recombination, on the PV efficiency (colour scale) by considering the illuminated diode equation ($J(V) = J_{dark}(e^{qV/K_BT} - 1) - J_{photo}$). The dashed horizontal black line corresponds to the ultimate photocurrent from the Lamertian light trapping in 1 μm thick Si and one can see the span of possible PV efficiencies depending on the carrier recombination properties of the device. In the graph, we include data points for the unpatterned and the three HUD designs, based on the J_{ph} and J_{dark} values found in our light absorption and PC1D simulations, respectively. For comparison, we also include the data point for the best demonstrated Si solar cell, which is 165 μm thick [171]. Note that the diode equation yields a slightly higher PV efficiency compared to that reported in Ref.[171] (0.5% higher efficiency) as the model neglects contact resistance losses. Figure 4.4c clearly visualizes the compromise for the total efficiency between light trapping and surface recombination properties of the different designs and it is particularly evidenced by the *HUD holes* and *HUD network*. Despite the fact that the two designs have different light trapping capabilities, the final PV efficiency is very similar.

While we theoretically predict the ultimate best device to be that with the *spinodal* texture, the large scale implementation of its fabrication may require some further technological developments. A combination of interference and nanoimprint lithography [175] has already demonstrated the fabrication of aperiodic structures with defined spatial frequency distribution in areas larger than 1 m^2. However, further work is needed to increase the required patterning resolution down to few tenths of nanometers. By contrast, HUD point patterns naturally arise in many physical systems, that can lead to simple and scalable fabrication of the *HUD holes* or *HUD network* patterns. For instance, it has been shown that the structure factor of dispersed colloidal particle (e.g. beads) patterns can be tuned by the ionic strength of the particular solvent [176, 177] and that the dewetting of semiconductor layers leads to HUD patterns [178]. Also, soft-imprint conformal lithography has proven an excellent low-cost alternative to pattern large-areas with a resolution below 10 nm that could actually serve for both *HUD holes and HUD network* [179]. While a master substrate has to be first made with other lithography methods (such as e-beam lithography), the master can be extensively re-used for the creation of multiple-use soft stamps.

4.6 Conclusions

In this Chapter, we have shown that stealthy HUD point patterns are an excellent platform to design a wealth of highly efficient nanoscale textures for trapping light in ultra-thin Si solar cells. We have described three different texture designs that offer broadband isotropic light trapping with a characteristic hyperuniform signature in the Fourier reflectance. We have fabricated such textures on a suspended Si membrane and experimentally demonstrated the highest absorption in 1 μm-thick Si, corresponding to a J_{ph} of 26.3 mA/cm^2. This exceptional light trapping can potentially be further improved by optimising the anti-reflection coating and incorporating a metal back-reflector, which in turn serves as electrical contact. Taking into account state-of-the-art values of Si electronic properties and IBC solar cell device design, we estimate realistic PV efficiency above 21% for a 1 μm-thick c-Si cell, which represents a breakthrough toward flexible, light-weight c-Si PV.

4.7 Materials and Methods

Absorption Simulations

Optical simulations were performed by our collaborator at the University of Surrey using a freely available finite-difference time-domain (FDTD) solver [180]. In all cases, the disordered structures are generated under periodic boundary conditions and are modelled as super-cells with sizes between 10 - 15 μm. For absorption simulations, periodic boundary conditions are employed in the transverse directions and perfect matching layer boundary conditions in the longitudinal direction. The dispersive dielectric function of Si was modeled using a sum of Lorentzian terms [135] as detailed in the SI section 4.8 and the mesh resolution was 5.2 nm. To calculate the absorption, the structure was illuminated by broad bandwidth plane waves pulses, and the subsequent transmitted and reflected fluxes were recorded for a long simulation time. Due to the diffusive character of the wave propagation and presence of various localised resonances in the disordered texture layer, the simulation is not run for a fixed amount of time but it keeps running until the field in the slab have decayed by a factor of 5×10^{-5} from its peak value in an interval of 20 simulation time units [180].

Sample Fabrication

For the fabrication of the HUD-patterned Si films, single crystal $\langle 100 \rangle$ 1μm Si membranes (Norcada Inc.) were used. We found that the actual thickness of the membrane varies slightly from sample to sample and within the membrane itself. From the Fabry-Pérot interference pattern in the absorption spectrum for the unpatterned membrane nearby the patterned areas, we deduce a total thickness of 1180 nm. The membranes were either 1.3×1.3 mm^2 or 4.8×4.8 mm^2 in size in a Si frame of 10×10 mm^2 and 300 μm thick. The nanopatterns were made by electron beam lithography followed by reactive ion etching. First, CSAR e-beam resist was spin coated as mask. Fields of either 100×100 , 150×150 or $180 \times 180\mu$m^2 patterns were exposed. After exposure and development, 200 nm of the

Si membrane was etched by first removing the native oxide followed by HBr and O_2 etching. The left-over resist was lifted off, and the sample was ready for Fourier microscopy. For the absorption measurements, an additional layer of resist (OrmoComp® resist) was spin coated on top of the sample to act as anti-reflective coating, ARC. The effects of the ARC on light absorption are described in the Supplementary Information section 4.8. From the interference fringes in the absorption spectrum taken on the unpatterned area, we deduce that the resist layer is of 200 nm.

Fourier-Space Illumination and Imaging

In order to experimentally characterize the structure factor of the HUD structures, we employed high-NA back focal plane imaging, also known as Fourier microscopy. In this technique angle-dependent scattering patterns of a sample are captured in single shot measurements, as opposed to performing angular scans using a rotation stage. We used a home-built inverted microscope reported in Ref. [168] that operates in reflection mode, so we chose the structures on the Si wafer for these measurements for easier handling. The microscope is infinity corrected with an Olympus MPlan IR 100x NA=0.95 objective, a 200 mm tube lens and 200 mm Fourier lens.

As the light source we use a cw DPSS laser (Lasos DPSS) with a wavelength of 561.3 nm. At this wavelength, the actual microscope NA equals 0.89, as calibrated with a diffraction grating. The image of the objective back focal plane is recorded by an Andor Clara silicon CCD camera. Captured Fourier images directly map the in-plane momentum space. Scattering at angles θ, ϕ (polar angle relative to sample normal and azimuthal angle, respectively) projects onto the camera plane at the location $(x, y) = f_o(\cos\phi \sin\theta, \sin\phi \sin\theta) \propto \mathbf{k}_{||}$, where f_o is the microscope objective focal length (f=1.8 mm). Since we essentially measure the structure factor as function of $k_{||}$ (wave vector parallel to the Si/air interface), one would expect to see the same dependence in both reflection and transmission.

Essential to our experiment is that the HUD patterns have structure factor $S(\mathbf{k}_{||})$ predominantly at parallel momentum just outside the NA of our collection objective. From free space one can therefore access the

structure factor for parallel momenta up to twice the microscope NA by illuminating at multiple oblique incidence angles [$0 < \frac{|\mathbf{k}_{\text{in},||}|}{2\pi/\lambda} \approx \text{NA}$].

Illumination with tailored $\mathbf{k}_{\text{in},||}$ is generated by using a spatial light modulator (Meadowlark 1920×1152 XY Phase Series SLM) that is imaged onto the microscope back focal plane. For each structure we collected six images arranged as the vertices of a hexagon. To obtain $S(\mathbf{k}_{||})$ collected images were shifted by their respective $k_{\text{in},||}$, while overlapping image areas were averaged.

Absorption Measurements

Absorption measurements on the membrane were done by using an integrating sphere microscope (modified LabSphere GPS-020-SL with the 17 mm working distance objective Mitutoyo M Apo Plan NIR 50× and NA = 0.42) coupled with a supercontinuum laser (Fianium WL-SC-390-3) and an acousto-optical tunable filter (AOTF, Crystal Technologies, with roughly 4 nm bandwidth). The photodetectors are Thorlabs amplified Si detectors (PDA100A), read out by Stanford Research Systems SR830 lock-in amplifiers. More details about the integrating sphere microscope set-up can be found in Ref. [163]. We have used three photo-detectors to measure the reference beam, the reflected and the transmitted/forward scattered light, respectively. The light reflected back into the objective is detected with the reflection detector, while the integrating sphere detector detects the transmitted and scattered light. The absorbance is calculated by subtracting the reflected and transmitted/scattered power from the incident power. Two reference measurements in reflection and transmission were done with a glass slide and calibrated mirror, to account for the response function of the set-up.

4.8 Supplementary Information

4.8.1 Design Parameters and Optimisation Flow

Figure 4.5 is a schematic representation of the optimisation procedure used in this work to achieve the final 3D HUD-based textures. We start with an empty canvas in k-space. From the waveguiding properties of the Si slab and coupled mode theory (see section Mode Coupling Analysis) we guess the best diffraction k-range that maximises efficiency. Second, we populate the k-space uniformly with the wavevector constrains derived in the previous step. For the HUD patterns, only the inner bound for the wavevector is used. As the stealthiness parameter χ is increased, a ring distribution naturally forms. Then, by inverse Fourier transformation of the k-space distribution a 2D point pattern is obtained. From the 2D point pattern, a 2D two-phase structure is obtained in a decoration step. For the spinodal, the two-phase structure is obtained by the random superposition of cosine waves with random phase with wave vectors imposed by the k-space distribution and thresholding the resulting function at a fixed height value. As a final step, the two-phase pattern is extruded to a height h_G and incorporated as part of the full 3D solar cell. Figure 4.6 is a cross-section representation of the 3D device design that is considered for the FDTD calculations in the last optimisation step. The sames values for h_{AR}, h_G and n_{AR} have been fixed to all design. We have used the values as obtained from optimising light absorption in a Si slab with a periodic hexagonal pattern (the periodicity of which was also optimised).

In the final optimisation step of the HUD and spinodal patterned cells, light absorption in the film is optimised by fine-tuning the average lattice spacing (a) and Si filling fraction (f) by using FDTD simulations. The optimised design parameter values are shown in Table 4.1.

Experimentally, a polymer resist was used as the low refractive index material by spin coating and a commercial membrane with nominal thickness of 1 μm. From the interference pattern in the absorption spectrum of the unpatterned membrane (figure 4.7), we deduce the actual thickness of the membrane and resist (listed in Table 4.2). On the pattern, we expect the ARC layer to deviate from the resist thickness on the unpatterned region.

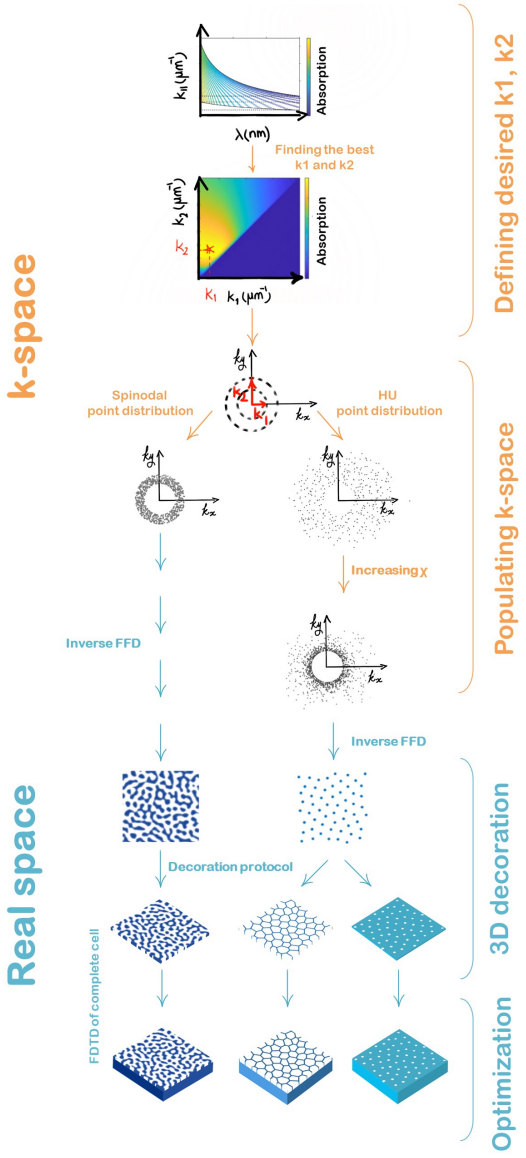

FIGURE 4.5: Schematic representation of the optimisation flow

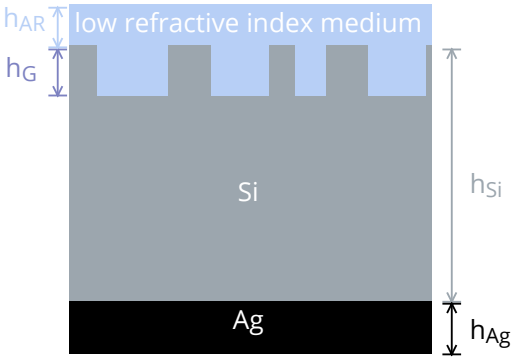

FIGURE 4.6: Schematic picture of the device design

Pattern	h_{AR} (nm)	h_G (nm)	n_{AR}	f (%)	a (nm)	χ
Unpatterned	72	196	1.82	–	–	–
Periodic hex	72	196	1.82	79	644	–
HUD network	72	196	1.82	55	475	0.5
HUD holes	72	196	1.82	68	480	0.4
Spinodal	72	196	1.82	58	–	–

TABLE 4.1: Parameters for the structures optimised for the full device.

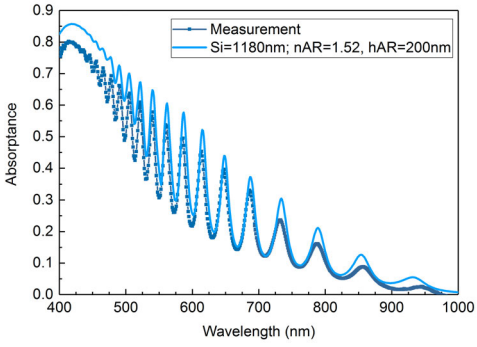

FIGURE 4.7: Measured and calculated absorption for a Si membrane suspended in air with a top layer of refractive index 1.52.

Figure 4.8 is the calculated reflectance from a representative double layer anti-reflective coating on c-Si. The two layers consist of the infiltrated

Parameter	Fabricated value	Optimal value
h_{AR}	50-100 nm	72 nm
h_G	200 nm	196 nm
h_{Ag}	–	200 nm
h_{Si}	1180 nm	1000 nm
n_{AR}	1.52	1.82

TABLE 4.2: Values of the parameters for the fabricated and optimal structures

pattern (with an effective refractive index considering the filling fraction of Si for each pattern) and the ARC layer. By using the parameters listed above for ARC refractive index and thickness, pattern thickness and Si filling fraction and the double-layer ARC model described in Ref. [181], we find that on average reflectance is below 10% for the wavelength range of 400 to 900 nm.

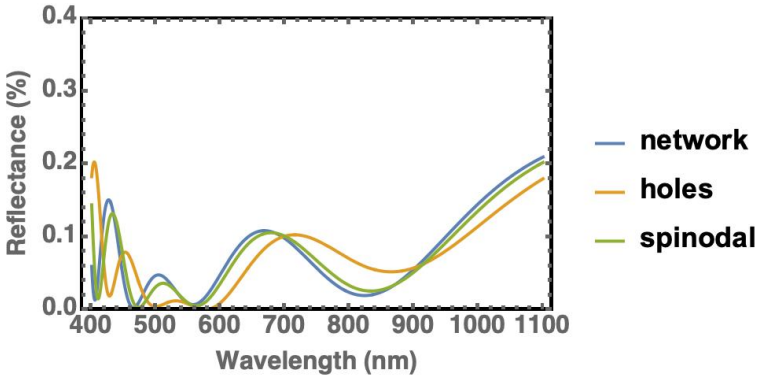

FIGURE 4.8: Calculated reflectance for a representative double layer anti-reflection on c-Si, with the layers being the ideal ARC and the infiltrated pattern.

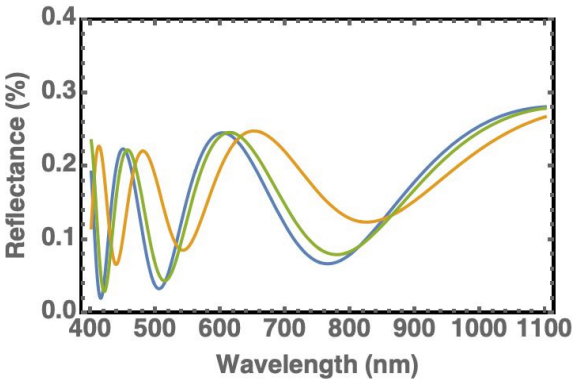

FIGURE 4.9: Calculated reflectance for a representative double layer anti-reflection on c-Si, with the layers being the resist-infiltrated pattern and top resist layer of 50 nm.

In our experiments, we have used a polymer resist as the low refractive index material, which has a sub-optimal refractive index ($n = 1.52$) and thickness ($h_A R \sim 50 - 100$ nm). The resulting reflectance (figure 4.9) is on average 10% higher than the previous case (figure 4.8).

4.8.2 Absorption Spectra in the Full Device

The simulated absorption for the optimised HUD-based textures in a full device configuration (i.e. including the Ag back reflector and optimised design parameters listed in Table 4.1) are shown in the figure below. The dispersive dielectric function of Ag was modeled using using the parameters from Ref. [135].

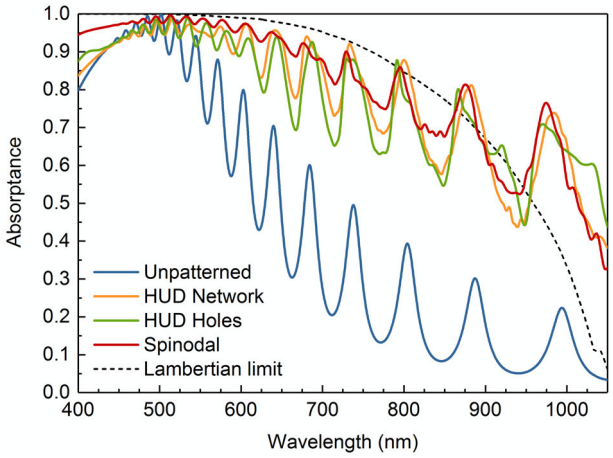

FIGURE 4.10: Simulated absorption spectra for the optimised textures in a full device configuration.

4.8.3 Si and Ag Dispersion Models

The dispersive dielectric function of c-Si was modeled using using a sum of Lorentzian terms [135]

$$\epsilon(\omega) = \epsilon_0 + \sum_{i=1}^{2} \frac{\sigma_i \omega_i^2}{\omega_i^2 - \omega_0^2 - i\omega\gamma_i} \,, \tag{4.1}$$

with the following values

	ε_0	ω_1	σ_1	γ_1	ω_2	σ_2	γ_2
c-Si	3.815	3.077	466.50	0.657	3.078	-458.431	0.669

TABLE 4.3: Parameters used to model the c-Si dispersion in Eq. 4.1.

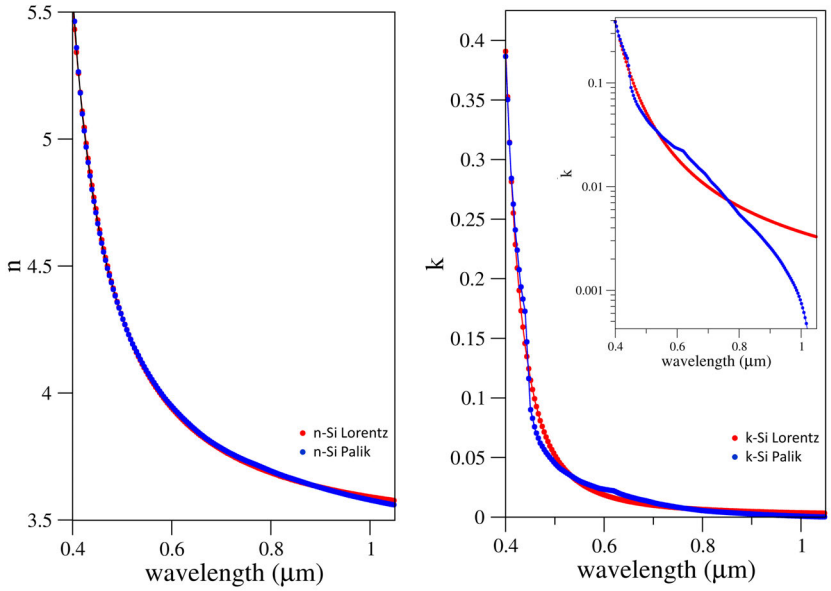

FIGURE 4.11: Comparison of the real and imaginary part of the c-Si index of refraction used in the simulations (Lorentz label) against the values in Ref.[182] (Palik label). The inset shows the same data in logarithmic scale to reflect on the discrepancy between the model and experimentally measured extinction coefficient at long wavelengths.

	ε_0	ω_1	σ_1	γ_1
Ag	3.8451	$9.986 \cdot 10^{-21}$	$5.4821 \cdot 10^{41}$	0.0129

TABLE 4.4: Parameters used to model the Ag dispersion in Eq. 4.1.

4.8.4 Mode Coupling Analysis

The coupling to guided modes is achieved through roughening or corrugating the surface of the absorbing layer, which renders certain portions of the guided modes excitable by incident light, giving rise to guided resonances. For the case of periodic patterns, it was shown that the $4n^2/\sin\theta$-limit calculated for a lambertian scatterer can be surpassed, when the grating

structure exhibits sub-wavelength modal confinement [183]. The analysis in this Chapter is based on the temporal coupled-mode theory [Haus1984] and applied to the case of nanophotonic light-trapping. The ultimate limit of achievable absorption corresponds to the sum over the absorption spectra of all guided resonances present in the frequency interval of the incident light and normalized by the same. The amplitude change with respect to time of a single guided resonance is given by [183]:

$$\frac{d}{dt}a(t) = \left(i\omega_0 - \frac{N\gamma_e + \gamma_i}{2}\right)a + i\sqrt{\gamma_e}S(t)\ , \tag{4.2}$$

with a the resonance amplitude (here, $|a|^2$ is the energy per unit area in the slab), ω_0 the resonance frequency, N the number of excitation channels that a given resonance can couple to, γ_e denotes the extrinsic loss-rate to each of the N channels, γ_i the intrinsic loss rate of the resonance due to material absorption, and S the amplitude of plane wave for a given excitation channel. Assuming a harmonic expansion for the resonance and the incident wave amplitudes, $a(t) = a(\omega)\exp(i\omega t)$, $S(t) = S(\omega)\exp(i\omega t)$, the absorption spectrum of the resonance is given by

$$A(\omega) \equiv \frac{\gamma_i(\omega)\,|a(\omega)|}{|S(\omega)|} = \frac{\gamma_i\gamma_e}{[\omega-\omega_0]^2 + [\gamma_i + N\gamma_e]^2/4}, \tag{4.3}$$

The spectral cross-section of the resonance is found through the integral $\sigma = \int_{-\infty}^{\infty} d\omega A(\omega)$, which, under the assumption of weak variation of N, γ_e, and γ_i with frequency, is given by

$$\sigma = 2\pi\gamma_i \frac{1}{N + \gamma_i/\gamma_e}. \tag{4.4}$$

In the overcoupling regime $\gamma_e \gg \gamma_i$, or in case $N \gg \gamma_i/\gamma_e$, the maximal value of eq. 4.4 can be approximated as [183]:

$$\sigma_{\max} = 2\pi\gamma_i/N \tag{4.5}$$

This maximum spectral cross-section carries the unit of frequency and when normalized by the incident spectral bandwidth $\Delta\omega$, it is assumed that the resonance contributes an additional $\sigma/\Delta\omega$ to the average absorption $\bar{A}$. The latter can equivalently be expressed by an effective absorption coefficient

α_{T} times thickness of the absorbing layer ℓ, or $\bar{A} = \alpha_{\mathrm{T}}\ell$. The value of $\bar{A}$ is then found as the sum over the maximum spectral cross-section of all modes, normalised by the incident spectral bandwidth $\Delta\omega$:

$$\bar{A} = \frac{\sum \sigma_{\max}}{\Delta\omega} = \frac{1}{\Delta\omega}\sum_{m}\frac{2\pi\gamma_{i,m}}{N_m}\,, \tag{4.6}$$

where the index m labels individual resonances and the summation is performed over all modes in the frequency interval $\Delta\omega$. When the guided resonance is approximated as a plane wave in the slab, the intrinsic loss-rate can be expressed as $\gamma_{i,m} = \alpha_m \cdot v_m$, where α_m is the mode's absorption coefficient $\alpha_m = 2\frac{\omega}{c}\kappa_m$. Here, κ_m and v_m and denote the imaginary part of the mode's refractive index and its group velocity, respectively.

The number of channels N associated with a given mode are obtained by considering the structure factor of the surface texture. We approximate the structure factor as a ring in reciprocal space of homogeneous intensity with inner radius k_1 and outer radius k_2 and assume that waves scattered by the surface patterning acquire any wavevector exclusively within this range with equal probability. From the area of the structure factor $\mathcal{A} = \pi\left(k_2^2 - k_1^2\right)$ and the area of a single mode $\mathcal{A}_k = 2\pi k_m \Delta k_m$, the number of channels can then be approximated as

$$N_m = \frac{\mathcal{A}}{\mathcal{A}_k} = \frac{(k_2^2 - k_1^2)}{2k_m\Delta k_m}, \tag{4.7}$$

with the mode's propagation constant $k_m = \frac{\omega}{c}n_m$, the mode's refractive index n_m and where the spectral width of the resonance Δk_m depends on the structure factor as well as the incident bandwidth $\Delta\omega = c\Delta k$, with speed of light c. The case of a continuous structure factor as considered here in contrast to the discrete points in reciprocal space corresponding to a periodic grating bears the consequence that the absorption spectrum in the vicinity of a resonance is not necessarily in the form of a sharp lorentzian, but instead can have significant absorption over a larger wavelength interval. From the broad shape of the resonance in the HUD case shown in figure 4.12, we infer that a single average value will inaccurately represent the same and integration over the spectral width Δk_m will result in a more sensible approximation. For this case, the summation over the guided resonances is

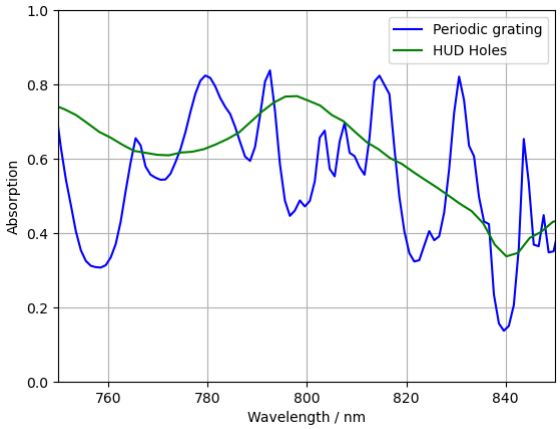

FIGURE 4.12: Excerpt of the absorption spectrum for an optimized periodic grating compared with a stealthy hyperuniform point distribution, obtained from FDTD simulation described elsewhere.

performed for each small wavelength interval and the result normalised by the spectral bandwidth of the resonance $\Delta\omega_m = c\Delta k_m$. Furthermore, the mode's group velocity $v_\mathrm{g} = \frac{c}{n+\omega\frac{\partial n}{\partial\omega}}$ approaches the phase velocity $v_\mathrm{p} = \frac{c}{n_m}$, since $\partial n \to 0$ in the small wavelength interval, such that the internal loss-rate can be approximated as $\gamma_{i,m}(\omega) = \alpha_m(\omega)\cdot v_\mathrm{g}(\omega) \approx \alpha_m(\omega)\frac{c}{n_m}$. Substituting N and γ_i in eq. 4.6 and rewriting the same for the narrow band limit $\Delta\omega \to c\Delta k_m$, we obtain:

$$\tilde{A}_\mathrm{T}^\omega = \sum_m \frac{4\pi\alpha_m k_m}{n_m(k_2^2 - k_1^2)}\,, \tag{4.8}$$

where superscript ω indicates that α_m, k_m, and n_m are now evaluated at the frequency ω under consideration and not averaged across the resonance's spectral width. Equation 4.8 clearly highlights the influence of the structure factor on the absorption in the slab. The $k_{1,2}$-ring area relates to the number of modes that couple to a single resonance and reducing it on the one hand increases the overall absorption. On the other hand, the number of modes taking part in the summation is also reduced, leading to a lower overall absorption. This has an important impact in the broadband regime where there is a large ensemble of relevant modes for absorption as shown in figure 4.2. Conversely, in the narrowband regime, where the number of

relevant modes is comparatively small, it is possible to reduce the area of the structure factor without greatly disturbing the number of modes in the summation.

In order to calculate an upper limit for the total absorption of light in the slab, we employ the analytical solutions derived for lambertian light-trapping in textured solar cells [184], which considers a thin absorber with the texture on the front-, and a perfect metal reflector on the rear surface. The formula is reproduced in eq. 4.9 below:

$$A_{\mathrm{T}}(\omega) = \frac{1 - \exp\left(-f_p \cdot \tilde{A}_{\mathrm{T}}^{\omega}\right)}{1 - (1 - \frac{1}{n}) \exp\left(-f_p \cdot \tilde{A}_{\mathrm{T}}^{\omega}\right)}, \tag{4.9}$$

where the product absorption coefficient times slab thickness $\alpha\ell$ is identified with eq. 4.8 as indicated above. The calculated path-length enhancement factor $f_p = 4$ in the weakly absorbing limit results in an overestimation of the absorption in the small-wavelength range, but is retained nonetheless to facilitate computation of the spectrally averaged absorption. The latter is found through convolution of eq. 4.9 with the AM1.5 photon flux and integration over the range $[400, 1050]$ nm, normalized to the total amount of photons in the same interval;

$$IA = \frac{1}{\int_{\omega} F(\omega) d\omega} \int_{\omega} A_T(\omega) F(\omega) d\omega, \tag{4.10}$$

where $F(\omega)$ describes the number of photons per square meter and second at the frequency ω as obtained from the AM1.5 spectrum.

Figure 4.13 shows the spectrally averaged absorption as a function of k_1 and k_2, approximated by Eq. 4.10; we obtain that the intensity is maximised for $k_1 = 9.1\mu\mathrm{m}^{-1}$ and $k_2 = 24.8\mu\mathrm{m}^{-1}$, but maintains relatively large values for a range of k values around the optimal ones.

The optimal values for k_1 and k_2 can be further refined by taking into account the anti-reflecting coating ($h_{\mathrm{AR}} = 72nm$, $n_{\mathrm{AR}} = 1.82$) and the corru-

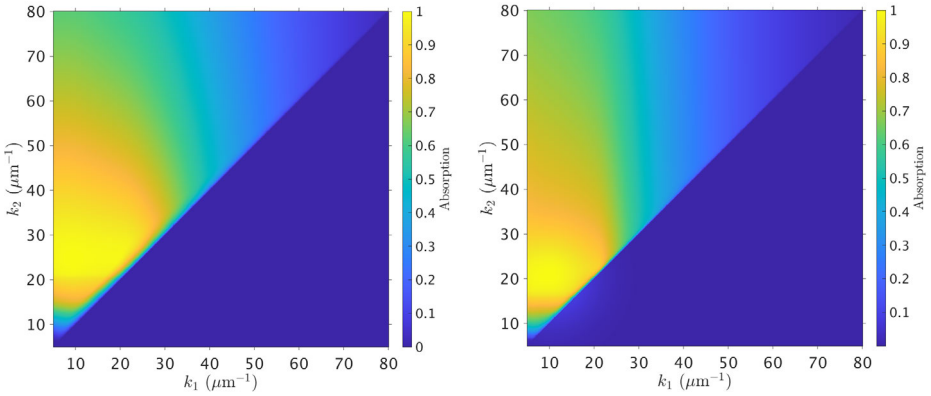

FIGURE 4.13: Absorption of a Si slab as a function of the inner (k_1) and the outer (k_2) radius of the ring-shaped homogeneously distributed structure factor, using the spectrally averaged absorption over the frequency range 400 – 1050 nm. Left: Mode data obtained through a finite-difference eigenmode solver for a slab with metal back-reflector in air. Right: Similarly obtained mode data for a slab with back-reflector, anti-reflective coating ($h_{AR} = 72nm$, $n_{AR} = 1.82$) and including Maxwell-Garnett effective medium approximation for the patterned layer.

gated surface by using an effective homogeneous medium with a complex refractive index calculated using Maxwell-Garnett effective medium theory for a slab of thickness 196 nm. Under these assumptions, the intensity is now maximised for $k_1 = 9.7\mu\text{m}^{-1}$ and $k_2 = 20.4\mu\text{m}^{-1}$.

For the last mentioned optimized $k_{1,2}$-values the absorption is compared with the bulk absorption coefficient times thickness $\alpha_0(\omega) \times \ell$ to identify the absorption enhancement across the spectral bandwidth. From the trends in figure 4.14 it appears absorption is enhanced throughout the entire spectral bandwidth, especially so in the low-wavelength regime, while the absorption approximates the product $\alpha_0(\omega) \times \ell$ close to the bandgap of silicon. The agreement of both curves emphasizes the role of eq. 4.8 as the effective absorption (coefficient times thickness), attained through employment of the surface texture.

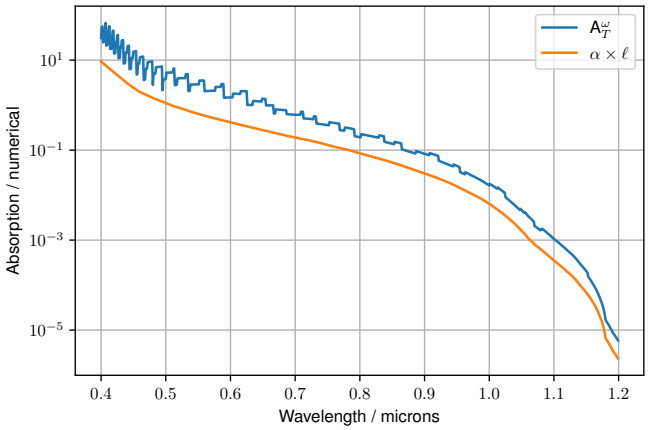

FIGURE 4.14: Comparison of eq. 4.8 with $\alpha_0 \ell$, the product of bulk absorption coefficient with slab thickness.

4.8.5 Angular Dependence of Absorption

In this section we contrast the angular dependence of the absorption in the samples analysed. The results presented in figure 4.15b show that the periodic structuring gives rise to a strongly anisotropic absorption, whereas for a disordered structuring (figure 4.16), be it hyperuniform or spinodal the angular response is mostly isotropic, roughly following the unstructured slab (figure 4.15a) case, but with an enhanced absorption due to the optimised coupling of the incoming solar radiation to the quasiguided modes of the silicon slab.

4.8.6 Device Simulation Parameters in PC1D

PC1D is used to model and simulate a 1 μm silicon solar cell, the used parameters are displayed in Table 4.5. These values match state-of-the-art Advanced HE-Tech devices as reported by Liu *et al.* [185]

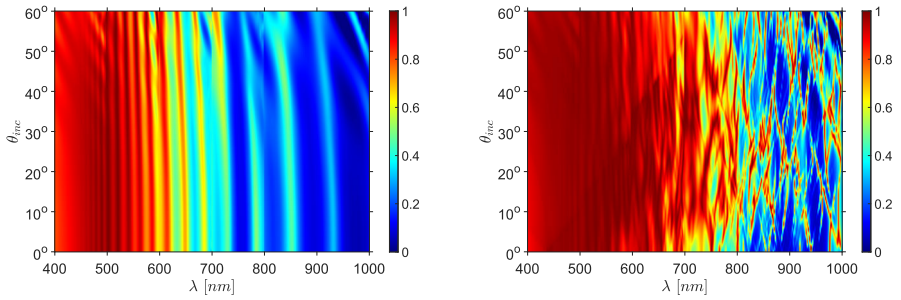

FIGURE 4.15: Angular dependence of the absorption for a) an unstructured 1μm-thick silicon slab and b) the periodically structured texture in a 1μm-thick silicon slab.

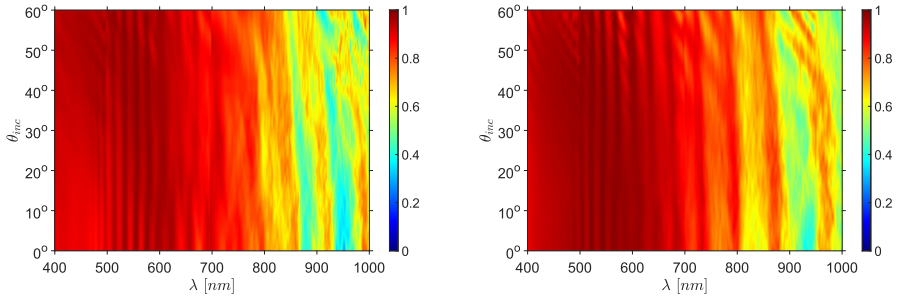

FIGURE 4.16: Angular dependence of the absorption for a) a hyperuniform structured texture and b) the spinodal structured texture in a 1μm-thick silicon, respectively.

Constant parameters	Value
Exterior rear reflectance	100%
Base contact	2 Ω
Emitter peak doping	6 x 10^{18} cm^{-3}
Background doping	10^{17} cm^{-3}
Bulk recombination	500 µs
Rear surface recombination	1 cm/s
Front surface recombination	100 cm/s

TABLE 4.5: Used parameters for PC1D simulations of the 1 μm Silicon solar cell.

In order to specify the device for our case, with front surface texturing, internal reflection is added to the model. From the absorption measurements, the short-circuit current density (J_{sc}) is calculated and internal reflection in PC1D is modified to match the calculated J_{sc}. Moreover, for the three different structures (HUD Network, HUD holes and Spinodal) the front surface recombination was increased due to the extra surface generated by texturing. The enhancement factor differs per structure as a HUD Network structure requires more etching compared to HUD holes and has therefore a larger surface and thus a larger recombination velocity (SRV) enhancement factor. With increased internal reflection and a SRV enhancement factor, open-circuit potential (V_{oc}) and efficiency (η) can now be obtained and are presented in Table 4.6. The corresponding I-V and efficiency curves for all four surface texturing are displayed in Figure 4.17.

	SRV factor	Internal reflection	V_{oc} (V)	J_{sc} (mA/cm^2)	Efficiency (%)
Unpatterned	1	59.5	0.769	18.4	12.1
HUD holes	1.75	96.25	0.770	32.4	21.2
HUD Netw.	3.274	96.5	0.755	32.6	21.1
Spinoidal	2.37	97.32	0.764	33.8	22.1

TABLE 4.6: Results of PC1D simulations with the values presented in Table 4.5. Internal reflection is altered until it matches the calculated J_{sc}.

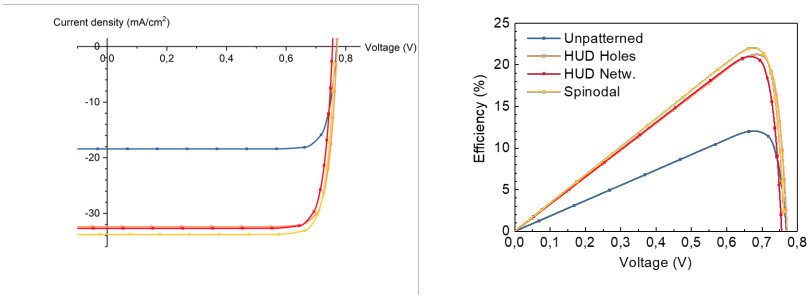

FIGURE 4.17: I-V curves (a) and efficiency curves (b) corresponding to different front textured surfaces. The colours represent the different structures.

4.8.7 Bulk Lifetime and Surface Recombination Effects

A comparison of the 1μm Si membrane with the presented standard values to other devices is made by adjusting several parameters in PC1D. Firstly, efficiencies of the four devices are calculated with a range in bulk recombination lifetime (τ) of 100 μs to 2 ms, plotted in figure 4.18. Different bulk lifetimes translate to the quality of silicon, as high quality silicon has a long bulk lifetime and vice versa. In order to have the 1 μm device into perspective with a 200 μm solar cell, PC1D was again used with the same parameters as in Table 4.5.

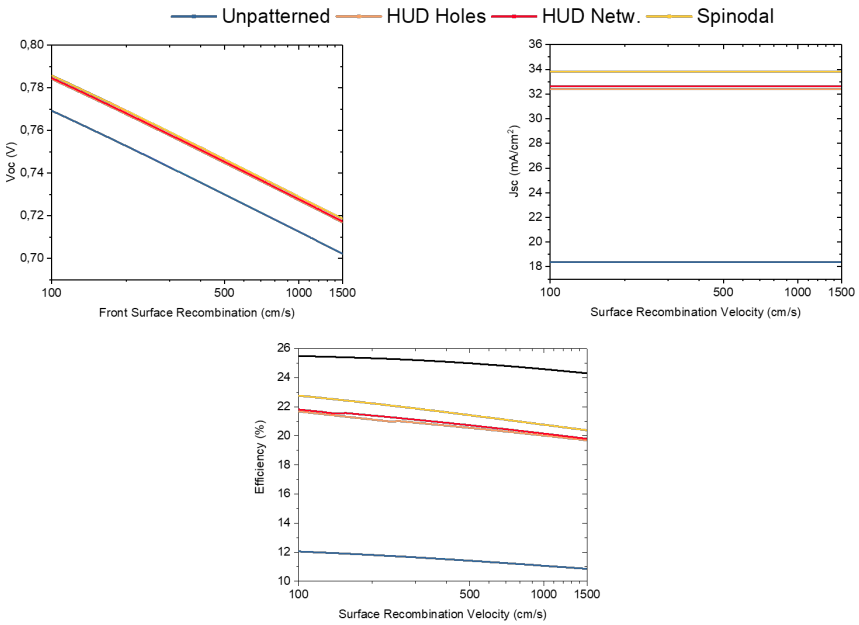

FIGURE 4.19: Efficiency plotted against the logarithm of SRV values for the four different structures. The efficiency plot also contains efficiency of bulk 200 μm silicon as reference (black line).

Figure 4.18 clearly shows that the efficiency in any of the thin film cells is hardly affected by increasing the bulk recombination lifetime from 100 μs to 2000 μs. This observation is explained by the fact that a 1 μm silicon membrane is too thin for bulk recombination to play a major role in

recombination losses. Bulk lifetime thus has little to no influence on thin film Si and bad quality silicon can therefore be used for thin films without a major loss in efficiency.

On the other hand, an increase in lifetime in a 200 μm Si wafer does affect efficiency significantly, particularly when the bulk lifetime becomes smaller than 500 μs. The efficiency drops by 1.7% absolute efficiency by increasing the bulk lifetime from 100 to 2000 μs. For thicker wafers it is therefore necessary to use silicon with the highest possible quality to minimize bulk recombination losses.

Figure 4.19 shows how is the efficiency affected by the surface recombination velocity (SRV) at the front surface. We observe that increasing the SRV induces an efficiency drop in all devices, patterned, unpatterned and bulk. An increase in SRV from 100 to 1000 for the flat surface results in a decrease in efficiency of about 1% absolute. With texturing and therefore extra surface, the decrease in efficiency for the patterned thin films is about twice as much. Again, this can be explained by the fact that the surface area to volume ratio for a 1 μm silicon membrane is very large and the surface recombination dominates.

τ=500 μs

	SRV=100 cm/s			SRV=1000 cm/s		
	V_{oc} (V)	J_{sc} (mA/cm^2)	η (%)	V_{oc} (V)	J_{sc} (mA/cm^2)	η (%)
Unpatterned	0.744	40.2	25.5	0.722	40.2	24.5
HUD Holes	0.743	43.01	27.3	0.714	43.0	26.0
HUD Netw.	0.739	43.1	27.1	0.700	43.1	25.5
Spinodal	0.744	43.3	27.4	0.708	43.3	25.9

SRV=100 cm/s

	τ=500 μs			τ=5000 μs		
	V_{oc} (V)	J_{sc} (mA/cm^2)	η (%)	V_{oc} (V)	J_{sc} (mA/cm^2)	η (%)
Unpatterned	0.744	40.2	25.5	0.753	40.3	26.1
HUD Holes	0.743	43.01	27.3	0.751	43.1	27.8
HUD Netw.	0.739	43.1	27.1	0.745	43.4	27.9
Spinodal	0.744	43.3	27.4	0.745	43.2	27.6

TABLE 4.7: Results of PC1D simulations for a 200 μm Silicon solar cell. For comparison an SRV of 100 cm/s and bulk lifetime of 500 and 5000 μs (top), and bulk lifetime of 500 μs and SRV of 100 and 1000 cm/s (bottom) are displayed in the same table.

Table 4.7 summarizes the solar cell performance in a bulk Si cell for two extreme cases of bulk lifetime (0.5 and 5 ms) and SRV (100 and 1000 cm/s). For the rest of the electronic parameters, we have used the values listed in Table 4.5. For the sake of comparison, we have also considered the same light trapping and enhanced surface area given by the different nanopattern designs. Because of the small effect of SRV to the total efficiency in bulk Si, the V_{OC} is the same (within two decimal spaces) for all the designs.

Figure 4.20 shows V_{oc} and efficiency as a function of thickness. V_{oc} first increases with increasing thickness and after approximately 10 microns it decreases constantly due to more recombination mechanisms in bulk material. However, efficiency increases in the first part rapidly and around 30 microns flattens out to a relatively constant value. This increase in efficiency is mostly caused by an increased Jsc which in turn is the result of more light absorption in bulk material.

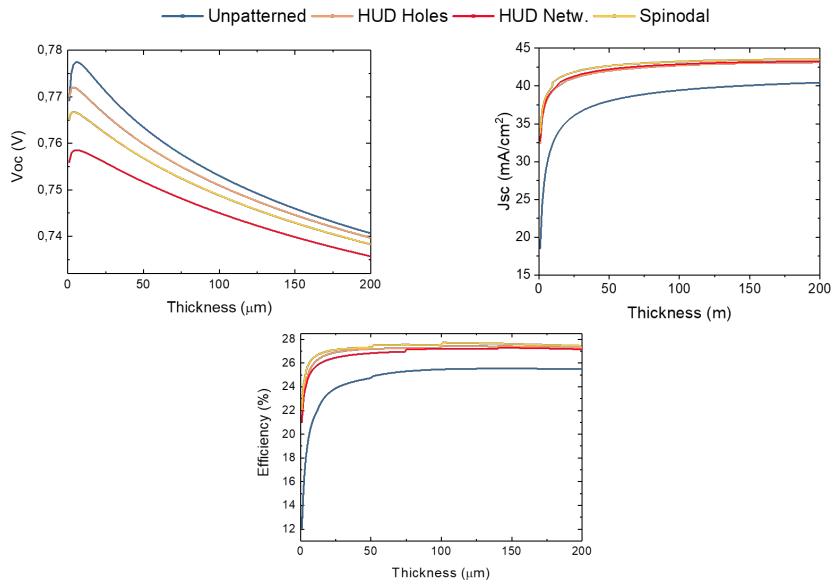

FIGURE 4.20: Open-circuit voltage V_{oc}, short-circuit current density J_{sc} and solar cell efficiency for p-type silicon with the four different surface texturing plotted against thickness.

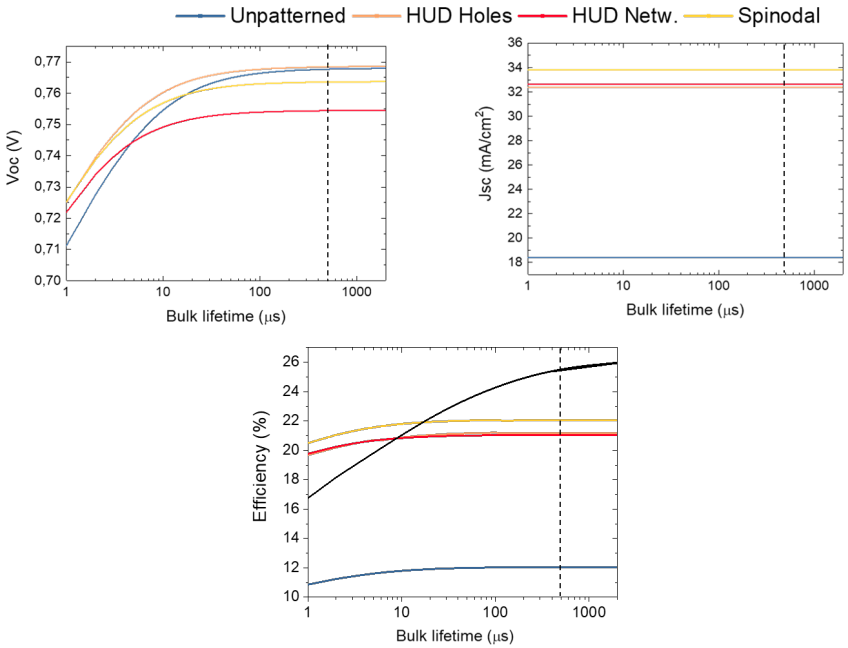

FIGURE 4.18: Efficiency plotted against the logarithm of bulk recombination lifetime for the four different structures. The efficiency plot also contains efficiency of bulk 200 μm silicon as reference (black line).

CHAPTER 5

Combining 1D and 2D waveguiding in Ultrathin GaAs NW/Si Tandem Solar Cell

As an effective means to surpass the detailed balance efficiency limit, tandem solar cells have been successfully designed and used for years. However, there are still economical and design set-backs hampering the terrestrial implementation of tandem solar cells. Introducing high efficiency, thin Si-based tandem cells that are flexible in design (shape and curvature) will be the next major step towards integrating highly efficient solar cells into fashionable designs of today's buildings and technologies. In this Chapter we present an optically coupled tandem cell which consists of a GaAs nanowire (NW) array on a 2 μm-thick Si film as top and bottom cells, respectively. By performing FDTD simulations we show that coupling the incident light to guided modes of the 1D wires not only boosts the absorption in the wires, but also efficiently transfers the below bandgap photons to the Si bottom cell. Due to diffraction by the NW array the momentum of the transmitted light is matched to that of guided modes of the 2D Si thin film. Consequently, infrared light is up to four times more efficiently trapped in the Si bottom cell compared to when the film is not covered by the NWs.

5.1 Introduction

In Chapters 3 and 4 we have proposed two new concepts for thin, lightweight and high efficiency PV, which will make solar cells more suitable to be integrated in urban landscapes and would largely contribute to solving the global warming threat that we are facing today. Despite great potential of tailored nanostructuring for large absorption in such devices, their efficiency is still limited by the detailed balance (i.e. thermodynamic) limit. While stacking of solar cells with different characteristic bandgaps is the most common strategy to surpass the detailed balance efficiency limit, such tandem devices are typically heavy weight, rigid and costly.

A fascinating strategy to potentially reduce both cost and rigidity is to combine thin film Si PV (few micrometers in thickness) with semiconductor NW solar cells. The mechanical flexibility and resilience of micrometer thin cells introduces their adaptability to curved surfaces as well as the use of new potentially lighter encapsulation materials. As previously mentioned in Chapter 2, the small footprint of the NWs breaks the lattice mismatch restriction so that any material combination is possible, including III-V/Si [186–193]. Also, the needle-like morphology of NWs results into a superior light absorption per volume with respect to their thin film counterparts [40, 72, 79, 80, 96, 194–196], which provides a path to save expensive and non-abundant elements such as indium or gallium. Experimental NW ensemble solar cells have shown similar extraordinary increase in conversion efficiencies as in hybrid perovskite-based PV.

Silicon is a highly desirable component in any tandem design thanks to the mature understanding of its optical and electronic properties as well as its widely available fabrication technologies. As mentioned in Chapter 4, downscaling Si to few micrometers in thickness compromises the solar cell performance due to the poor Si absorption of infrared light and requires light management strategies. Resonant nanostructures [197, 198], diffraction gratings [199–201] and hyperuniform designs have been proposed to improve light management in <10 μm-thin silicon single junction cells. So far, no strategies have been proposed specifically for tandem designs. Although the combination of III-V semiconductor NWs with bulk Si as tandem cells has been studied both theoretically [202–207] and experimentally

[208, 209], the dramatic absorption loss in <10 μm-thin Si films in this type of tandem cells and the possible solutions are yet to be studied.

In this Chapter we demonstrate that optically coupled systems consisting of nanostructures and thin films in a tandem fashion can improve the overall solar cell performance beyond that of uncoupled counterparts. Similar to 4 we make use of k-space engineering, but this time for a tandem geometry. Here, we show that light scattering in NW arrays can be smartly tuned to match the momentum of guided modes in the bottom cell. This way, the top cell provides two functionalities for the tandem device: 1) The GaAs NWs absorb the light so efficiently that filling only 10% of the volume is enough to have about the same fundamental PV efficiency limit as in a bulk GaAs cell, and 2) the grating effect of the NW array allows to couple the transmitted light to the guided modes of a 2 μm-thin Si slab, which quadruples light absorption in the Si cell.

5.2 Results and Discussion

Here, we present a combination of two waveguiding effects in NW-thin film tandem architectures. This concept combines the photonic properties of nanoscale semiconductors, the grating effect in ordered arrays with fabrication on low-cost silicon substrates. Here we go beyond coupling to the fundamental hybrid HE guided mode in vertically standing NWs to maximize light absorption and PV performance in NW-based solar cells (see Chapters 2 and 3). We now take additional advantage of the NW array configuration of the top cell as a grating coupler of sub-bandgap photons and funnel this light towards the thin bottom cell (See figure 5.1a). From now on, we will address the spectral range from 875 nm (bandgap of GaAs) to 1200 nm as NIR.

As a proof of concept, we have considered a periodic 2D square array of GaAs NWs on top of a 2 μm-thick Si cell (see figure 5.1b), but the design principles apply to any combination of materials. The rear surface of the coupled system is covered with 200 nm silver as a back-reflector and possible back-contact. Since our focus is the optical properties proof of principle, we first only consider a GaAs NW array directly on top of a Si film

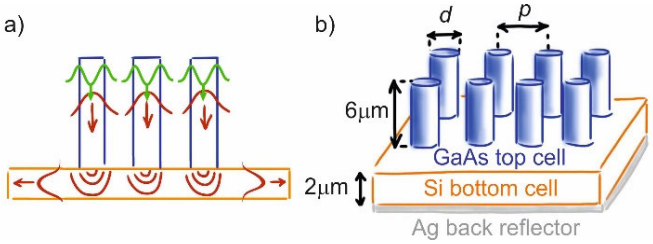

FIGURE 5.1: a) Schematic representation of the combined 1D-2D waveguiding in the NW-thin film tandem solar cell. The NW geometry ensures the efficient coupling of a plane wave coupling to guided modes of the 1D waveguide NW. The interference between all scattered light generates an interference pattern at the bottom cell. This light will be coupled to 2D waveguide modes of the Si thin film. b) The geometry of our tandem cell, consisting of a square array of 6 μm long GaAs NWs on a 2 μm Si slab. The 4T tandem cell is covered with 200 nm Ag at the back. Geometries can have different GaAs filling fractions by varying the diameter (d) and pitch distance (p).

for simplicity and to ensure an optimum optical coupling between the two cells. Then, we address the potential losses that occur when considering a more realistic device structure.

Figure 5.2, shows the simulated absorption and forward scattering cross-section of a single GaAs NW for different diameters. We have considered the light flux that is transmitted towards the lower half space of the simulation area as forward scattering. Both types of spectra show strong peaks in absorption/scattering that are ruled by the coupling to the NW guided modes, HE, the order of which is marked by a star (HE11), triangle (HE12), square (HE13) and circle (HE14). The position of the peaks shifts to longer wavelengths with diameter. In general, the best sunlight absorption is given by NWs with diameters, for which the peak in absorption related to the fundamental HE11 guided mode is close to the material's bandgap (diameter of 140 nm in GaAs). At larger diameters, efficient coupling to the HE11 mode occurs at wavelengths longer than that of the bandgap. Consequently the overall absorption decreases in favor of scattering. At even larger diameters, wavelengths close to the bangdap efficiently couples to higher order HE modes, resulting into both strong absorption and scattering (see for instance the spectra for the diameter of 500 nm).

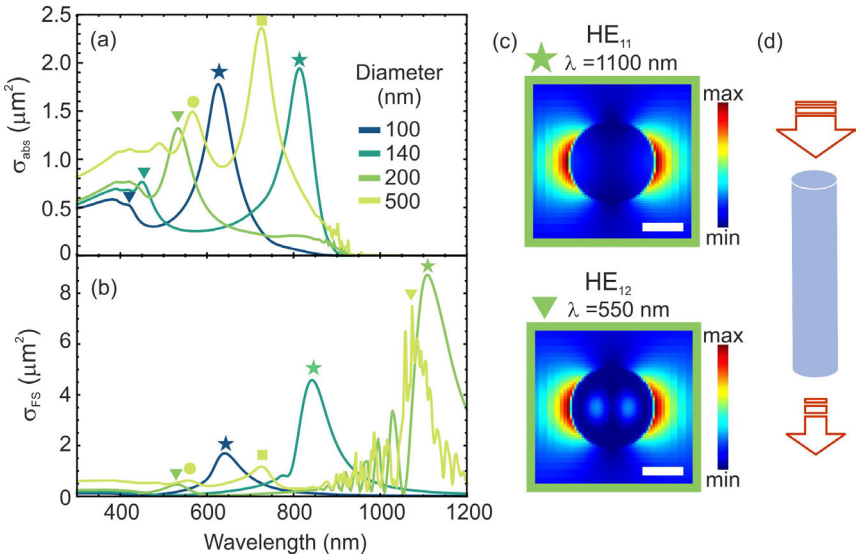

FIGURE 5.2: Absorption (a) and forward scattering (b) cross-section of a single GaAs NW of 6 μm in length and various diameters. The peaks in absorption/forward scattering result from incoming light coupling to waveguiding modes of the NW, represented by different symbols according to the guided mode order. c) Field intensity distribution in the axial cross-section of a NW of 200 nm in diameter at two different wavelengths, that highlight the coupling into the HE11 and HE12 guided modes. Scale bar is 100 nm. d) Schematic representation of the simulation, where a plane wave is travelling along the main axis of the NW.

In the particular case of GaAs NWs with diameters of 200 and 500 nm a strong scattering peak related to the first and second order HE mode, respectively, lies in the 1000-1200 nm spectral range. In this wavelength range, which is right at the Si bandgap edge (∼1100 nm), the light is efficiently scattered forward by the GaAs NWs to the Si film underneath, which can be very beneficial to the Si bottom cell.

In order to better quantify this effect in the tandem structure we have integrated the simulated absorption spectra of the NW array and Si film in the complete device design with the solar spectrum, and estimate the short circuit current (J_{sc}^{GaAs}) for each sub-cell (see Methods section). Figure 5.3a shows J_{sc}^{GaAs} of the NW array as a function of NW diameter. Different colours correspond to different NW pitch distances from 314 to 800 nm.

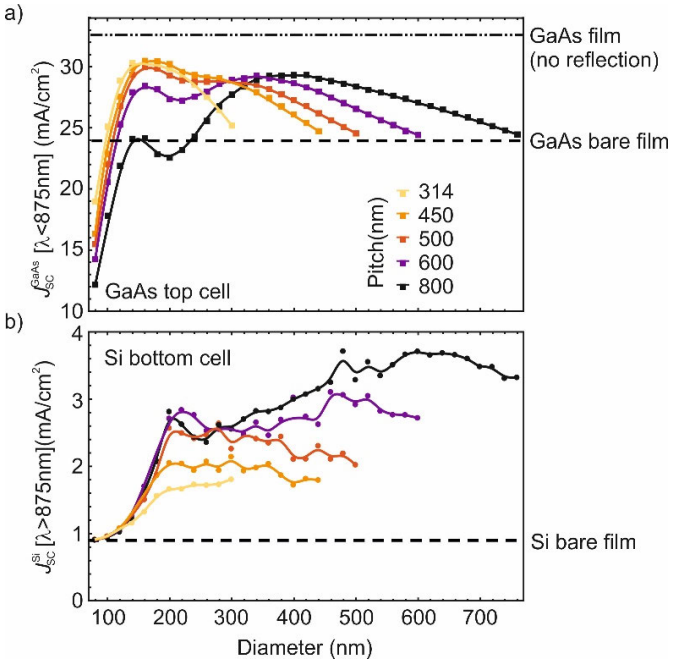

FIGURE 5.3: Short circuit current (J_{sc}) of GaAs NW array (length: 6 μm) as a function of diameter, for pitch distances of 314, 450, 500, 600 and 800 nm. b) Short circuit current in the Si film calculated for wavelengths longer than 875 nm, as a function of the GaAs NW array geometry. Arrays with pitch distances of 314, 450, 500, 600 and 800 nm are shown in different colours. The different lines correspond to the expected current densities of the cases as explained in the text.

In accordance to previous works [49], J_{sc}^{GaAs} rapidly increases with the NW diameter followed by a decrease when the diameter increases beyond 150 nm. For pitch distances 500, 600, and in particular 800 nm, the absorption increases again at large diameters, as expected from the fact that a peak in absorption occurs near the bandgap due to light coupling into higher order guided modes. It is worth noting that, in all the arrays the ultimate absorption is less than that in a 6 μm-thick GaAs film and when the filling fraction is above $\sim$0.2 (for instance, diameter of 160 nm for pitch distance 314 nm and diameter 400 nm for pitch distance 800 nm) the J_{sc}^{GaAs} decreases regardless of individual NW geometry. We attribute this loss in absorption due to increased reflectivity (see SI for more details) arising from the increased refractive index contrast at the Air/GaAs interface [210].

Now we turn to the light absorption in the Si bottom cell. To highlight the optical effects of the top cell on the bottom one, figure 5.3b shows the J_{sc}^{Si} calculated from integrating the solar spectrum and the simulated Si absorption spectra only for energies below that of the bandgap of GaAs (i.e. $\lambda > 875$ nm). We plot the result as a function of GaAs NW diameter. Because in this wavelength range GaAs is transparent, changes in J_{sc}^{Si} ($\lambda > 875$ nm) for different NW array geometries must arise from the optical coupling of the two systems together. Different colours in the graph correspond to the different periodicities of the NW array.

In all the arrays studied here, J_{sc}^{Si} ($\lambda > 875$ nm) is the same for the smallest NWs and it matches with the short circuit current for the same wavelength range of a free-standing Si film with a Ag back-reflector (0.9 mA/cm^2), which is represented by a horizontal dashed line in figure 5.3b. This value is one order of magnitude smaller than what is attainable in bulk Si (9.8 mA/cm^2), if zero reflection is assumed. Interestingly, increasing the NW diameter rapidly increases the NIR-related current in Si, which in most cases it surpasses the expected current for the 2 μm thick Si on Ag if reflection is considered to be 0 (dash-dotted line in figure 5.3b). This is only true for diameters smaller than 200 nm, at which point the growth of J_{sc}^{Si} ($\lambda > 875$ nm) with NW diameter is smaller. In the more sparse arrays, this change in the growth of the current at a diameter of 200 nm even results into a peak. A second peak is also discerned at diameters around 500-600 nm. The highest calculated J_{sc}^{Si} ($\lambda > 875$ nm) in the 2 μm thick Si is $\sim$3.7 mA/cm^2, which represents almost 40% of the bulk reflection-less limit. The anti-reflection properties of the array cannot explain this trend, given that it is mostly ruled by the filling fraction instead of the NW diameter, and it detriments at filling fractions beyond 20%.

The fact that the NIR-related current is increased up to a factor 4 with respect to the bare Si film by incorporating a NW array top cell is a significant light trapping scheme that is obtained "for free" when using a nanostructured top cell. To confirm this link, we focus on the absorption spectrum in the Si film for the wavelength range between 875 nm and 1200 nm, figure 5.4a. The dashed curve shows the absorption in a reference Si thin film in air (same thickness and with a Ag back-reflector), in which the Fabry-Pérot resonances are present. The solid curve shows the absorption of the same Si film with a top GaAs NW array of d=200 nm and p=800 nm. As compared

to the bare film, additional sharp absorption peaks arise. We explain these sharp peaks as resonant coupling of light to the 2D waveguiding modes of the Si film, enabled by the coherent interference of scattered light by the NWs in the periodic array.

As in standard gratings, the scattered light from each NW coherently interferes and gives rise to a diffraction pattern. The in-plane momentum of the diffracted light ($k^{diff}_{[mn]} = \left(\frac{2\pi}{p}\right)\sqrt{m^2+n^2}$ where p is the pitch distance and m and n are the diffraction orders in the two orthogonal in-plane directions) can be beyond the light cone in air enabling the diffracted light to couple into guided modes of the Si film. As a consequence, the effective optical mean path under such conditions is strongly enhanced and results into an increased short circuit current. Opposite to standard diffraction grating solutions in PV [211], in our design the brightness or intensity of the diffracted light by the NW array is strongly dependent on the NW diameter (see SI). The effect proposed here is similar to light trapping strategies in thin film absorbers with the use of periodic arrays of metal or semiconductor resonators at either the front or rear-surfaces [127, 212].

For completeness, we plot the dispersion relation of the TE and TM guided modes of 2 μm Si film in figure 5.4b (in blue and red, respectively). For the wavelength range of interest (875-1200 nm) the mode propagation constant (β) lies within the range of $\sim$7 to 20 rad/μ. The modal calculations were done numerically by considering a 2 μm thick Si film sandwiched between Ag and a dielectric of refractive index 1.45. The latter is a fair approximation to the refractive index of the NW-air ensemble in this wavelength range. The wavevectors for *[mn]* grating orders of a periodic NW array with pitch distance of 800 nm are displayed in horizontal solid black lines. As expected, the intersections between grating orders and guided modes coincide at the same wavelength where the absorption peaks occur. For clarity, not all intersections are shown. This highlights that the increase in Si absorption is not only affected by efficient forward scattering from each NWs, but is also strongly determined by whether or not the momentum of the transmitted light is matched to the 2D guided modes of the thin Si film. Further proof is given by the cross-sectional field energy distribution in the whole device structure for a wavelength where the momentum is matched (top and bottom plots in figure 5.4c). For comparison, we also

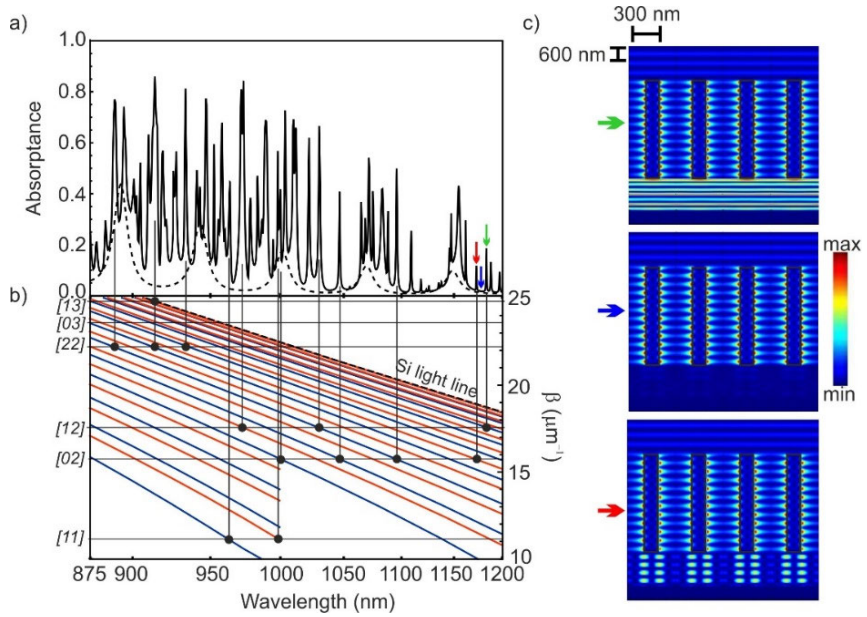

FIGURE 5.4: a) Absorption spectra of the Si film without (dashed) and with (solid) the NW array on top in the NIR spectral range, for which GaAs is transparent. The NW array parameters are 800 nm pitch distance and 200 nm in diameter. b) Dispersion curves for TE and TM guided modes of a 2 μm Si slab, in red and blue respectively. The horizontal lines show the grating orders of a 2D periodic array with a 800 nm period. [mn] refer to the diffraction orders. Vertical lines are to highlight some intersections of the guided modes with the diffraction orders. c) Field distribution in a transverse cross-section of the full device for three different wavelengths, marked in the spectrum by arrows. The field profile at the peaks in absorption (green and red) match well with the excitation of the 7^{th} order TE and 4^{th} order TM guided modes in Si, respectively.

include the field energy profile under non-matching conditions (middle plot). The increased photocurrent in Si due to diffraction-enabled coupling to guided modes also explains the strong dependence on pitch distance of the largest attainable $J_{SC}^{Si}(\lambda > 875\,nm)$ in figure 5.3b. This means that the top GaAs NW array is not only active as a part of the solar cell, but also contributes to light trapping in the bottom Si cell.

To estimate the efficiency of the NW arrays to trap NIR photons in Si, we have calculated the ultimate $J_{SC}^{Si}(\lambda > 875\,nm)$ for a 2 μm Si film accord-

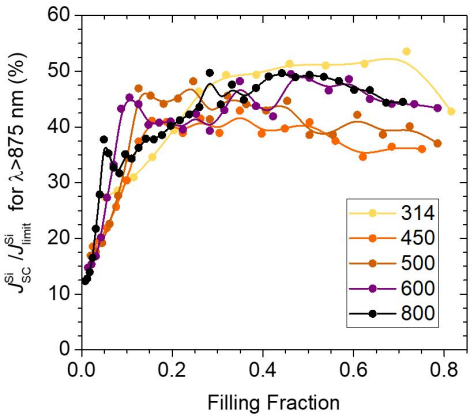

FIGURE 5.5: Light trapping efficiency in the Si film as a function of the NW array filling fraction for arrays with different pitch distances. The efficiency is obtained by normalising the short circuit current in Si by that calculated considering the $4n^2\pi(p/\lambda)^2\alpha$ absorption limit.

ing to the Yablonovitch limit, which makes use of geometric optics and lambertian texturing by considering a $4n^2$ enhancement of the absorption [213]. Within this framework, the ultimate current is 6 mA/cm^2, which results into a light trapping efficiency of 62% in the best case by using our design. While the Lambertian limit is commonly used in the community as a reference, its validity has been debated when considering nanostructures [214–217]. In particular, Yu et al. [218],found that a more accurate limit in a periodic grating whose periodicity (p) is smaller than the wavelength, considers the absorption to be enhanced by a factor $4n^2\pi(p/\lambda)^2$. This means that the ultimate light trapping of the NW array top cell is determined by the pitch distance. figure 5.5 represents the light trapping efficiency in the Si film as a function of array filling fraction through the normalisation of the current by the periodicity-dependent limit. Interestingly, all the configurations have a similar trend in efficiency with ultimate values around 50%.

Last, we comment on the detailed balance conversion efficiency of our tandem design. Detailed balance only considers radiative losses, which is in practice not attainable due to high surface or Auger recombinations. While the former is particularly true in GaAs NWs, Auger recombination

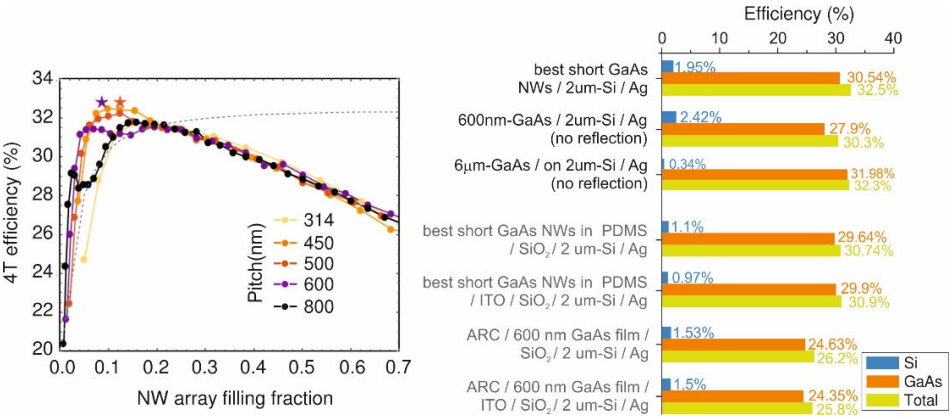

FIGURE 5.6: Left: Detailed balance conversion efficiency of the 4T GaAs NW-Si film tandem cell as a function of GaAs array filling fraction. The NWs are 6 μm long and the Si is 2 μm thick. An Ag reflector is considered on the rear side. Different colours correspond to different pitch distances of the NW array. Stars show the total efficiency achieved by considering the NWs to be of 12 μm in length. The grey dashed line is the calculated 4T conversion efficiency of a GaAs equivalent film on 2 μm thick Si tandem, where the thickness of the GaAs film is such that it contains the same amount of material as in the array. Right: Summary of top, bottom and total cell efficiencies for our best performing designs along with the thin film and bulk equivalents. The geometry of the best short NWs is d=160 nm, p= 450 nm. Realistic designs are labelled in grey. ARC refers to anti-reflective coating based on a 100 nm tick dielectric of n=1.5.

limits the Silicon PV efficiency to ~94% of the detailed balance value in thin films [219]. Consequently, the efficiencies calculated here are thus slightly higher than what can be achieved in practice but it is a good figure of merit to compare the different tandem geometries.

The left plot in figure 5.6 is the four-terminal (4T) tandem conversion efficiency in the radiative limit as a function of GaAs NW array filling fraction, calculated as described in the methods section. The footprint of the GaAs array is tuned by changing both the diameter (d) and pitch distance (p) of the NW array. Different colours gather all data from same periodicities. We highlight two main observations in this plot in accordance to what has been described so far: 1) the maximum reachable efficiency strongly depends on the array geometry, and 2) after 20% of the surface being covered by GaAs the efficiency is independent of geometry and is

limited by reflection. The grey dashed plot depicts the 4T efficiency of the film-equivalent GaAs-Si tandem, where the GaAs array is transformed into a film that contains the same amount of material. In this case, the efficiency is calculated by considering a double pass of the light and no reflection (see the SI for more details). In general, the highest PV efficiencies achieved in our calculations for the ultra-thin tandem are when the top NW cell has a filling fraction around 5-15%. This is interesting when compared to the highest efficiency in the film-equivalent, where the more material the higher the PV efficiency. The best obtained efficiency based on our ultra-thin NW/thin film design is ∼32.5% for an array with p=450 nm and d=160 nm (i.e. only ∼10% of the surface is covered by NWs). Despite this value being larger than the 30.3% obtained for its film-equivalent and just slightly higher than the 32.3% obtained in the case where the GaAs cell is a compact 6 μm-thick film on the 2 μmSi/Ag bottom cell, it does not represent the best light trapping conditions in the bottom cell. According to figure 5.3b, d$>$ 200 nm and large p are best.

Arrays with larger pitch distances do not absorb all above bandgap photons. Thus, we have also calculated the total conversion efficiency by considering longer NWs (i.e., 12 μm) with d=200 nm for a couple of pitch distance conditions. The resulting PV efficiency is represented by stars of corresponding colours in the left plot of figure 5.6. Now, the total conversion efficiency is increased to 32.8% and is virtually the same in both cases. We have summarized all the best efficiencies along with the contributions from each cell in a chart in figure 5.6. While our design reaches efficiency values that are still well below the detailed balance limit for the bulk GaAs/Si tandem (38.7%), it over-performs the film-equivalent solution. The use of a hexagonal array configuration may improve the light absorption in the GaAs array, and thus the total efficiency. An even better solution might be the use of hyperuniform arrays with correlated disorder, where a continuous range of scattered momenta can be also tailored [129, 132, 220] as discussed in more detail in Chapter 4.

We have focused so far on the ultimate light absorption and detailed balance efficiency limit of the NW-Si coupled system, where the NW array is surrounded by air and a 4T configuration was assumed to avoid current matching conditions between top and bottom cells. In a realistic 4T device,

an intermediate contact and an insulating layer must exist between the two cells and the NWs will most likely be embedded in a polymer support that planarizes the top surface. To illustrate this effects, we have also performed simulations by considering the NW array being supported by a PDMS matrix on a 100 nm-thick Indium Tin Oxide (ITO) as transparent contact and a 100 nm-thick SiO_2 layer as insulator. In the case of the thin film equivalent, we have also incorporated a standard anti-reflective coating (ARC) based on a 100 nm-thick dielectric of refractive index 1.5. In the realistic device design, the ultimate detailed balance efficiency is higher if the GaAs is shaped in the form of NWs (30.9 vs 25.8%), but overall lower than the idealistic case (32.5%). By comparing the efficiency numbers with those obtained in a realistic configuration without the ITO layer, one can see that most of the loss comes from NIR absorption at the ITO (see SI for more details). This is not unexpected and highlights the need for new transparent conductive materials as intermediate and top contacts that are photonically inactive.

5.3 Conclusions

In conclusion, we have introduced a tandem design for GaAs NWs on μm-thick Si, in which the 1D waveguiding and scattering in GaAs NWs are combined with 2D waveguiding in Si film. While high order HE modes in the NWs maximizes above GaAs bandgap photon absorption, lower order modes efficiently forward scatter NIR light to the Si bottom cell. Coherent interference between the NW scatterers creates a diffraction pattern, the momentum of which enables to increase the optical path in the Si film. While the interwire distance determines the number of resonances in the absorption spectrum of Si, the NW diameter determines the coupling strength and hence the redistribution of energy in the Si thin film. We proved the concept of waveguiding combination, and our design can lead to achieve 62% of the Yablonovitch absorption limit of the bottom Si cell. We believe that with better engineering of the k-space of the NW array, e.g. hyperuniform designs, the absorption in both top and bottom cell can be increased even further.

5.4 Materials and Methods

In all calculations, the absorption spectra are obtained from FDTD simulations by using Lumerical software package. Computationally expensive FDTD simulations are done on the super computer LISA from SurfSara. The source in all the simulations is a broadband plane wave covering the wavelengths between 300 nm and 1200 nm. Complex refractive indices of the materials are taken by fitting polynomial functions to experimental data from Palik [221]. In the SI, the calculated absorption with the fitted values and a broadband source is compared to that obtained when using the exact numbers in a frequency sweep.

The unit cell of all absorption simulations consist of one GaAs NW standing on a 2 μ-thick silicon film covered by a 200 nm thick Ag film underneath as a mirror and rear contact. Both substrates extend through the boundaries of the FDTD simulation area. The top and bottom boundaries are chosen to be Perfectly Matched Layers (PML) to guarantee total absorption of light and to prevent parasitic reflections from the top and bottom boundaries. For the simulations of NW arrays, the side boundaries are chosen to be periodic, resulting into a square array. For the simulations in which absorption and forward scattering cross-sections are calculated for a single NW, a total field scattered field (TFST) configuration is used and the side boundaries are chosen to be PMLs. TFST is a predefined source in Lumerical which separates the scattered field from total field.

In order to calculate the conversion efficiency of our designed tandem cell, we use detailed balance principle in the radiative limit, namely only radiative recombination of photoexcited charge is taken into account as loss. This assumption will turn into ultimate thermodynamic efficiency limits, which is still far from real devices due to losses at contacts and the large non-radiative recombination rates, particularly relevant in NWs [222–225]. We have obtained the maximum conversion efficiency by calculating the electrical power as a function of bias voltage normalized by the incident power from the sun per unit surface area [$\eta = V \cdot J(V)/P_{solar}$]. The characteristic J-V curve of each cell is plotted by subtracting the dark current

from the photogenerated current $[J(V) = J_{dark}(V) - J_{ph}]$. In the radiative limit, the bias dependent dark currents were calculated by:

$$J^i_{dark}(V) = \int_{200\,nm}^{4000\,nm} e \cdot em^i(\lambda).b^i_e(\lambda, \mu)d\lambda, \tag{5.1}$$

where e is the elementary charge, $\mu = eV$ is the electrochemical potential of the electron-hole pair, and i refers to either the GaAs-NW array or Si film. The electrochemical potential is assumed constant over the whole sub-cell structure. Due to reciprocity, the photon emission and absorption rates of the cell are equal, thus $em(\lambda) = abs(\lambda)$ The absorption spectra, were obtained from the FDTD simulations, where normal incidence on the cell was considered. $b_e(\lambda, \mu)$ is the radiative emission rate per unit wavelength, described as

$$b_e(\lambda, \mu) = F_c \frac{2\pi}{\lambda^4} \left[\frac{1}{(e^{\frac{hc/\lambda - \mu}{k_B * T}}) - 1} \right] \tag{5.2}$$

where c is the speed of light, k_B is the Boltzman's constant, T is the temperature in Kelvin and h is Planck's constant. F_c is a geometry factor that highlights the emission profile of the cell. Despite it has been previously shown that the absorption in NW arrays is virtually constant up to angles ~75 degrees [42, 226], directional light emission (thus also light absorption) has been shown in sparse InP NW arrays (2 μm pitch) [227]. Such directivity has been predicted to lead to about 20 mV increase in the V_{OC} [228].Given the small effect, isotropic light emission towards the both upper and lower hemispheres was considered for simplicity in the NW array $(F_c = 4\pi)$ and only to the upper hemisphere in the thin film,$(F_c = 2\pi)$.

As explained in Chapter 3, the photogenerated current (J_{ph}) of each cell is calculated by plugging the AM1.5G solar spectrum $[N_{ph}(\lambda)]$ and the wavelength dependent absorption $[abs(\lambda)]$ in Eq. 3.1. We have used the limits of 300 nm to ∞ in this case to calculate the total photocurrent. Neglecting series or shunt resistance losses makes the short circuit current J_{SC} (i.e. current at $V = 0$) and J_{ph} to be the same. The maximum efficiency is given by $\frac{d}{dV}[J(V)V] = 0$. The four terminal (4T) efficiency is calculated by adding the efficiencies of the top and bottom cells, without any restrictions on matching currents or voltages.

5.5 Supplementary Information

5.5.1 Refractive Index Fitting Sanity Check

In FDTD simulations with a broadband source, the complex refractive index of the materials is fit to multi-component complex function. To ensure that the absorption with the fitted refractive index is properly representing that for the real values, we compare two sets of simulations for one design case (NW array with pitch distance of 444 nm and a pillar diameter of 180 nm, on a 2-μm Si film on 200 nm Ag). In the first simulation we divided the source wavelength into three parts: from 300 nm to 830 nm, from 800 nm to 930 nm, and from 900 nm to 1200 nm, with a resolution of 0.5 nm. By doing so we made sure to achieve a good fit to match experimental values of real and imaginary parts of refractive indices. We combined these three wavelength areas to cover the whole range. The absorption spectrum from this simulation is shown in black in figure 5.7. In the second simulation we performed a frequency sweep for our simulations with 1 nm wavelength step, meaning that the source was changed from a broadband source to a single frequency source, effectively increasing the computational time by a factor of 190. The absorption spectrum can be seen in red. Due to the good agreement between the two spectra we chose the first approach for all the other simulations presented in this thesis.

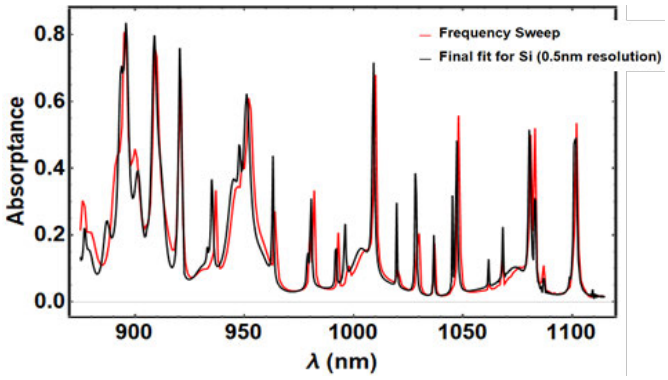

FIGURE 5.7: Comparison of the NIR absorption spectra of the Si film when calculated using a fit to the Si optical parameters and broadband sources with respect to the experimental values and monochromatic light.

5.5.2 Reflectivity Data

Figure 5.8 is the reflectance for the tandem structure (GaAs/Si/Ag) as a function of NW pitch distance and diameter. The reflectance has been calculated for the integrated spectrum of wavelengths <875 nm, in order to avoid the long wavelength light that may not be absorbed by the Si film.

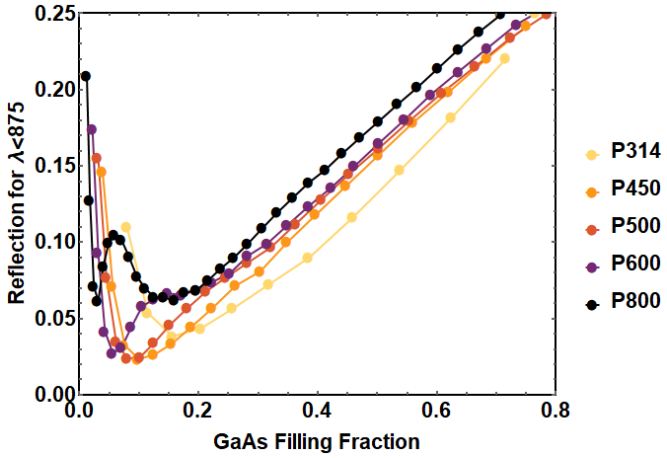

FIGURE 5.8: Simulated reflectance in the visible spectral range for the Tandem device as a function of NW array filling fraction.

5.5.3 Si Light Absorption Spectra as a Function of GaAs NW Diameter for p=314nm

Figure 5.9 shows the absorption in Si thin film for 900< λ (nm)<1125 for a NW array with a pitch distance of 314 nm, and diameters of 80, 100, 140, 160, 180 and 200 nm. The sharp absorption peaks are present in all spectra at the exact same wavelength, but their intensity increases with NW diameter. This confirms that the peaks are rising from diffracted light entering Si slab from the NW array (namely, the wave vector or wavelength of the diffracted light only depends on the periodicity of the array). Second, the Fabry-Pérot (FP) peaks are apparent even in the case with largest diameters, arising from multiple reflections from the zero-order diffracted light. Note that the period of FP peaks in the cases of diameters 180 and 200 nm NWs

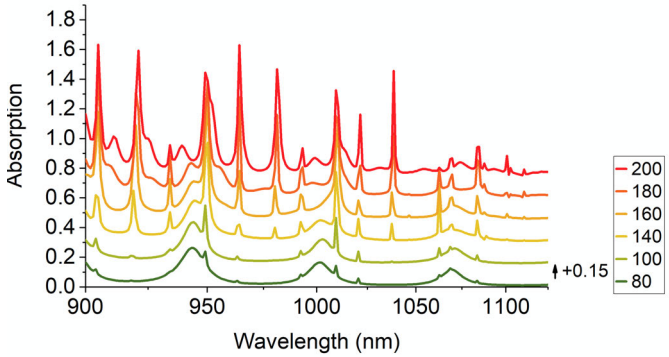

FIGURE 5.9: Absorption in Si thin film for NIR range for a NW array with a pitch distance of 314 nm, and various diameters (indicated by the legend in nanometers). Spectra are vertically shifted by 0.15 for clarity

seems to be smaller. This effect results from the fact that packed arrays on top of Si form the effective thickness of the dielectric slab to be larger which results in smaller periodicity of the FP peaks.

5.5.4 Thin Film-Equivalent Absorption Calculations

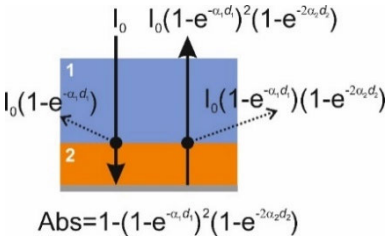

FIGURE 5.10: Schematic representation of how is the double pass absorption being calculated for the thin film equivalent tandem designs

As shown in figure 5.10, the absorption calculation for the thin film equivalent of the tandem design has been done using the Beer-Lambert law and neglecting reflection. In order to consider a realistic case, we assume the transmitted light from GaAs top cell to have a double pass in Si bottom cell, and then the remained transmitted light to pass through GaAs once more.

5.5.5 NIR Absorption in ITO

The detrimental effects of the ITO/SiO_2 inter-layers in a realistic device configuration for the NIR absorption in Si mostly comes from the absorption in the ITO (figure 5.11).

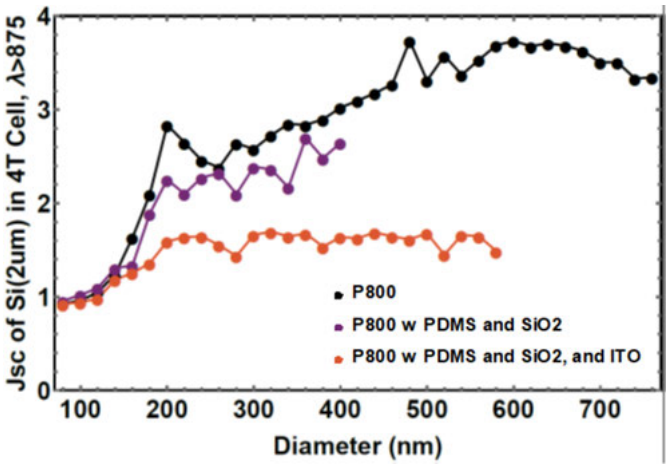

FIGURE 5.11: Calculated NIR-related short circuit current in Si for: GaAs NWs/2μm-Si/Ag (black), GaAs NWs in PDMS/SiO_2/2μmm-Si/Ag (purple) and GaAs NWs in PDMS/ITO/SiO2/2μmm-Si/Ag (orange)

Summary

Although some experts believe that the energy transition from fossil fuels to renewables is inevitable, others argue that the recent momentum in solar technology (and other renewables) does not guarantee this transition. On the one hand, the current global exponential growth is a clear trend and there are impressive local examples in which renewable energies have successfully replaced fossil fuels. On the other hand the current global share of solar energy in our energy consumption is still very low and both faster production of Photovoltaic (PV) modules and more installations are necessary. At the same time, public knowledge and education on renewables heavily depend on politicians' views and stands. To tackle these issues, we can get help from artistic approaches to form an un-biased and reliable bridge between the energy sector and society. At the same time, alongside with public acceptance of new technologies cost is one of the key driving factors in energy transitions. Building-Integrated Photovoltaics (BIPV) are part of smart spatial solutions to integrate solar cells into our societies, which is of extreme importance. Especially for countries like the Netherlands, with many densely populated regions, in order to protect the landscape it is crucial to integrate sustainable energy solutions into already-built areas. There are already many solutions to create integrable PV that are colourful, semi-transparent or flexible, however, there is still a major gap in power conversion efficiency compared to state of the art solar cells. This thesis introduces nanophotonic concepts that can bridge this gap. We focus on the built-in light management properties in semiconductor nanowires (NWs) to provide new concepts in PV, from colourful to flexible and high efficiency, either in single junction or tandem solar cells.

In **Chapter 2**, we focus on understanding the optical properties of one of the most effective nanostructures to capture, guide and efficiently absorb the light: Vertically standing semiconductor NW. We start by explaining light-coupling into waveguiding modes of the NWs which is the reason behind the uniquely high absorption cross section in these nanostrustures. Then, we evaluate the length-dependent absorption efficiency (defined as absorption cross section divided by geometrical cross section of the

NWs) obtained from Finite Difference Time Domain (FDTD) simulations by considering a modified Beer-Lambert law. We find that two exponential terms are required to explain NW's light absorption, one with a short range nature ($< 1\mu$m) and one with a long range nature (few tenths of microns). In the experimental section of this Chapter we perform fluorescent confocal microscopy measurements on long ($\sim 9\mu$m) GaAs NW arrays as means to visualize the light distribution around the NWs and thus the length-dependent absorption cross-section. The obtained energy density data cube shows a consistent dome-shaped shadow around each NW consistent with the length dependent absorption cross-section. We study the wavelength dependence of the shadow shape. By comparing off-axis fluorescence cross-sectional images with simulated 3D absorption cross-section of the NW array, we can better compare the cross-section geometry change with wavelength. Surprisingly, we find that the experimentally measured 3D absorption cross-section with fluorescence microscopy is explained by only considering the long range component from the modified Beer-Lambert law.

In **Chapter 3**, we explore in detail the potential of semiconductor NW-based solar cells as a powerful and tunable in design approach for wavelength-selective semi-transparent (ST) solar cells for BIPV. FDTD simulations of periodic arrays of vertically standing semiconductor NWs of three common PV materials (GaAs, InP, and Si) embedded in transparent polymer confirm that by changing diameter and periodicity one can engineer the absorption and transmission spectra of a solar cell to provide a broad range of bright colours, semi-transparency and high absorption. We explain the interesting relation between photocurrent (J_{ph}) and Average Visible Transmittance (AVT) for different array geometries by looking into their corresponding absorption spectra. From simulations under various illumination conditions (angle and spectrum), we find that the colour appearance is quite robust to spectral and small angle changes. For angles larger than $\sim 20^{\circ}$, the arrays show a more abrupt change in colour likely arising from the excitation of Mie resonance modes allowed by the off-axis illumination. Throughout the whole span of illumination angles, the expected photocurrent varies by $\pm 10\%$. Besides, we find opposite trends in J_{ph}/AVT versus incidence angle for different array geometries. It appears that only the NW arrays that show symmetric absorption spectra around

the visible spectral range at normal incidence, tilting the illumination is beneficial for the PV performance. In the experimental section, we test the fabrication feasibility of NW-polymer composites by embedding GaAs NW arrays in PDMS, peeling them off and transferring them to a clean cover glass. Two sets of arrays with average AVT around 20 and 50%, with purple, blue and green colours for each are demonstrated. We compare the transmission spectra and perceived transmitted colours to those expected from geometrical considerations. We also demonstrate optical images of these NW-polymer composites under angled incidence, ranging from 5 to 45 degrees. As predicted by theory, we observe two main regimes: from normal incidence up to 20-30° the colours are kept similar, and for larger angles the colour appearance of the arrays changes. Based on our results, and given the fact that high PV efficiencies have already been demonstrated in opaque NW arrays, this work highlights the potential of such nanostructures as new efficient solutions for BIPV.

In **Chapter 4**, we focus on ultrathin, high efficiency and flexible Si solar cells as another photonic-based solution to minimize the compromise of high conversion efficiency for aesthetics in solar cells. In this Chapter we present a new family of surface texturing, based on correlated disordered hyperuniform patterns, capable of efficiently coupling the incident spectrum into the silicon slab optical modes. We use three different texture designs that offer broadband isotropic light trapping with a characteristic ring-like signature which is measured in the k-space using a Fourier microscope in reflection mode. We fabricated these textures on a suspended Si membrane and experimentally demonstrated 66.5% solar light absorption in free-standing 1 μm c-Si layers. The absorption equivalent photocurrent derived from our measurements is 26.3 mA/cm^2, which is far above the highest found in literature for Si of similar thickness. Taking into account state-of-the-art values of Si electronic properties and IBC device design, we estimate realistic PV efficiency above 21% for a 1 μm-thick c-Si cell, which represents a breakthrough toward flexible, light-weight c-Si PV.

In **Chapter 5**, we study a promising tandem solution for flexible Si PV with high efficiency. Here we combine the unique light waveguiding and absorption in vertically standing NWs with k-space engineering given by

their arrangement into arrays to increase absorption in an ultra-thin tandem cell beyond the bulk limits. To do so, we design an optically coupled tandem cell which consists of a GaAs nanowire array on a 2 μm-thick Si film as top and bottom cells, respectively. From FDTD simulations we show that in thick GaAs NWs high order waveguiding modes can maximize above GaAs bandgap photon absorption, at the same time that lower order modes efficiently forward scatter Near-infrared light to the Si bottom cell. Coherent interference between the nanowire scatterers creates a diffraction pattern, the momentum of which increases the optical path in the Si film. While the interwire distance determines the number of resonances in the absorption spectrum of Si, the nanowire diameter determines the coupling strength and hence the redistribution of energy in the Si thin film. Consequently, infrared light is up to four times more efficiently trapped in the Si bottom cell compared to when the film is not covered by the nanowires.

In summary, this thesis provides new solutions for integrable PV by exploiting nanophotonic principles in nanoscale architectures. It shows a high degree of control over the absorption/transmission spectrum by using optical waveguiding in either nanowires or thin films. The photonic and design concepts presented here combined with highly-performing PV materials make the intersection between high-efficiency, flexibility, colour-tunability and transparency closer to reality.

Samenvatting

Hoewel sommige experts geloven dat de energietransitie van fossiele brandstoffen naar duurzame energie onvermijdelijk is, beargumenteren anderen dat deze transitie niet wordt gegarandeerd door het huidige momentum in zonne-energie (en duurzame alternatieven). Aan de ene kant, ondanks de exponentiele groei en indrukwekkende lokale voorbeelden, is het huidige wereldwijde aandeel van zonne-energie in onze energie consumptie laag en zijn zowel hogere productie van modules als een groter aantal installaties nodig. Aan de andere kant is publieke kennis en gewaarwording over duurzame energie afhankelijk van de positie van politici. Om deze problemen aan te pakken kan gebruik worden gemaakt van een artistieke benadering om een onbevooroordeelde en betrouwbare brug te slaan tussen de energie-sector en de maatschappij. Tegelijk met maatschappelijke acceptatie zijn de kosten een drijvende kracht in energie transities. Building-Integrated-Photovoltaics (BIPV) zijn deel van een familie slimme ruimtelijke oplossingen om zonnecellen te integreren in onze maatschappij. Vooral in een land als Nederland, met veel dichtbebouwde regio's, is het cruciaal om duurzame energiebronnen te integreren in bestaande bouw om het landschap te beschermen. Er zijn al veel bestaande oplossingen om geïntegreerde zonnecellen te maken die kleurrijk, semi-transparant of flexibel zijn, er is echter nog een groot verschil in efficiëntie. Deze thesis introduceert nanofotonische concepten om dit gat te overbruggen. Wij richten ons op de ingebouwde licht-management eigenschappen in halfgeleider nanodraden om nieuwe concepten voor zonnecellen te introduceren, van kleurrijk, tot flexibel en hoog efficiënt, en zowel in enkele junctie als in tandem zonnecellen.

In **hoofdstuk 2**, richten wij ons op het begrijpen van de optische eigenschappen van één van de meest effectieve nanostructuren om licht te vangen, te leiden en te absorberen: verticaal staande halfgeleider nanodraden. We beginnen met het toelichten van de koppeling van licht in waveguide modi in deze nanostructuren. Hierna onderzoeken we de lengteafhankelijke absorptie efficiëntie (gedefinieerd als de absorptie dwarsdoorsnede gedeeld door de geometrische dwarsdoorsnede van de nanodraden)

door middel van finite-difference time-domain (FDTD) simulaties, gebruikmakend van een aangepaste vorm van de wet van Beer-Lambert. Hieruit blijkt dat dat er twee exponentiële termen nodig zijn om de lichtabsorptie van de nanodraden te beschrijven, één met een korte afstand aard ($< 1\mu$m), en één met een lange afstand aard (enkele tientallen micron). In het experimentele deel van dit hoofdstuk gebruiken we confocale fluorescentiemicroscopie op reeksen lange ($\sim 9\mu$m) galliumarsenide (GaAs) nanodraden om de licht-distributie rond de nanodraden en daarmee de lengte-afhankelijk absorptie dwarsdoorsnede te visualiseren. De verkregen data van de energiedichtheid laat consequent een koepelvormige schaduw rond elke nanodraad zien, consistent met de lengte-afhankelijke absorptie dwarsdoorsnede. We bestuderen ook de golflengte-afhankelijkheid van de schaduwvorm. Door off-axis fluorescentie dwarsdoorsnede afbeeldingen te vergelijken met de gesimuleerde 3D absorptie dwarsdoorsnede van de nanodraad reeks kunnen we de dwarsdoorsnede geometrie beter met de golflengte beter vergelijken. Verrassend genoeg blijkt dat de met fluorescentiemicroscopie experimenteel gemeten 3D absorptie dwarsdoorsnede kan worden verklaard door alleen de lange afstand component van de wet van Beer-Lambert te beschouwen.

In **hoofdstuk 3**, verkennen we de potentie van zonnecellen gebaseerd op halfgeleider nanodraden als methode voor het ontwerpen van golflengteselectieve semi-transparante zonnecellen voor BIPV. FDTD simulaties van periodieke reeksen van verticale halfgeleider draden van drie veelvoorkomende fotovoltaïsche materialen (GaAs, InP, en Si) ingebed in een transparant polymeer bevestigen dat de absorptie en transmissie spectra van een zonnecel kunnen worden afgestemd door de diameter en periodiciteit van de draden te veranderen, en zo een groot bereik van felle kleuren, semitransparantie en hoge absorptie te verkrijgen. We verklaren de interessante relatie tussen fotostroom en de Average Visible Transmittance (AVT) voor verschillende geometrieën van de reeksen nanodraden door te kijken naar de corresponderende absorptie spectra. Uit simulaties met verschillende belichtingscondities (invalshoek en spectrum) blijkt dat de kleurweergave robuust is ten opzichte van kleine hoekveranderingen en het spectrum. Voor invalshoeken groter dan $\sim 20^\circ$ tonen de reeksen een meer abrupte verandering in kleur, welke waarschijnlijk wordt veroorzaakt door de excitatie van Mie resonantie modi, toegestaan door off-axis belichting. Over het hele bereik van invalshoeken varieert de verwachtte fotostroom met $\pm 10\%$.

Daarnaast observeren we tegenstelde trends in J_{ph}/AVT als functie van de invalshoek voor verschillende geometrieën van de reeksen. Het blijkt dat het kantelen van de belichting alleen voordelig is voor de efficiëntie van de zonnecel voor nanodraad reeksen die in het zichtbare bereik, bij normale belichting, symmetrische absorptiespectra hebben. In het experimentele deel testen we de haalbaarheid van het fabriceren van nanodraad-polymeer composieten door GaAs nanodraad reeksen in te bedden in PDMS, deze eraf te halen, en op een schoon dekglas te plaatsen. Hiermee demonstreren we de fabricage van twee sets van paarse, blauwe, en groene reeksen met een gemiddelde AVT rond respectievelijk 20 en 50%. We vergelijken de transmissie spectra en de kleurperceptie met de verwachting vanuit geometrische overwegingen. We laten ook optische afbeeldingen van deze nanodraad-polymeer composieten vanuit verschillende invalshoeken zien, van 5 tot 45 graden. Zoals voorspeld door de theorie observeren we twee regimes: van de normaal tot 20-30° zijn de kleuren behouden, maar voor grotere hoeken veranderd het voorkomen van de kleur. Deze resultaten, en het feit dat hoge fotovoltaïsche efficiënties al zijn gedemonstreerd in ondoorzichtige reeksen nanodraden, benadrukken de potentie van zulke nanostructuren als nieuwe en efficiënte oplossing voor BIPV.

In **hoofdstuk 4**, richten we ons op ultradunne, hoog efficiënte, en flexibele Si zonnecellen als nog een fotonische oplossing om het compromis tussen hoge efficiëntie en esthetiek in zonnecellen te minimaliseren. In dit hoofdstuk presenteren we een nieuwe familie van oppervlaktetextuur gebaseerd op gecorreleerde wanordelijke hyperuniforme patronen, die geschikt zijn om het invallende lichtspectrum efficiënt in de optische modi van het silicium te koppelen. We beschouwen drie verschillende ontwerpen voor de textuur die resulteren in breedband en isotroop invangen van licht met een karakteristieke ring-achtige signatuur die wordt gemeten in de k-ruimte met een Fourier microscoop in reflectie. We fabriceren deze texturen op een vrijstaand Si membraan en demonstreren experimenteel 66.5% zonlicht absorptie in 1 μm vrijstaande lagen c-Si. The absorptie equivalente fotostroom is 26.3 mA/cm^2 in onze metingen, wat ver boven de hoogste waarde uit de literatuur is voor Si van vergelijkbare dikte. Rekening houdend met state-of-the-art waarden voor de elektronische eigenschappen van Si en IBC ontwerpen schatten we een realistische fotovoltaïsche efficiency boven 21% voor een 1μm-dikke c-Si cel, wat een doorbraak betekent richting flexibele en lichtgewicht c-Si zonnecellen.

In **hoofdstuk 5**, bestuderen we een veelbelovende tandem oplossing voor flexibele Si zonnecellen met hoge efficiëntie. We combineren de unieke licht golfgeleiding en absorptie in verticale nanodraden met het ontwerpen van de k-ruimte bepaald door hun opstelling in reeksen, om de absorptie in een ultradunne tandem cel te verhogen boven de bulk limieten. Om dit te doen ontwerpen we een optisch gekoppelde tandem cel die bestaat uit een GaAs nanodraad reeks op een 2 μm-thick Si film als top en bodem cel, respectievelijk. Met FDTD simulaties tonen we aan dat in dikke GaAs nanodraden hogere orde modi van golfgeleiding de foton absorptie boven de bandkloof maximaliseren, terwijl tegelijkertijd lagere orde modi efficiënt nabij-infrarood licht naar de Si bodem cel verstrooien. Coherente interferentie tussen de nanodraad verstrooiers creëert een diffractie patroon, waarvan de golfvector resulteert in een langer optisch pad in de Si film. Hoewel de afstand tussen de draden het aantal resonanties in het absorptiespectrum van Si bepaald, bepaald de diameter van de draden de koppelingssterkte en daarmee de herverdeling van energie in de Si dunne film. Hierdoor wordt infrarood licht tot vier keer efficiënter gevangen in de Si bodem cel, vergelijken met een film die niet is bedekt met de nanodraden.

Samenvattend biedt dit proefschrift nieuwe oplossing voor integreerbare zonnecellen door gebruik te maken van nanofotonische principes in nanoschaal architecturen. Hieruit blijkt een hoge mate van controle over het absorptie/transmissie spectrum door het gebruik van optische golfgeleiding in nanodraden of dunne films. De hier gepresenteerde principes van fotonica en ontwerp, samen met hoog presterende fotovoltaïsche materialen, brengen ons dichter bij de combinatie van hoge efficiëntie, flexibiliteit, afstembare kleur en transparantie in een enkele zonnecel.

Bibliography

[1] Bruce Usher. *Renewable Energy*. Columbia University Press, 2019.

[2] *Snapshot of global PV 2021: https://iea-pvps.org/wp-content/uploads/20-21/04/IEA_PVPS_Snapshot_2021-V3.pdf*.

[3] Erik C. Garnett et al. "Photonics for Photovoltaics: Advances and Opportunities." In: *ACS Photonics* (2020).

[4] Varun Sivaram. *Taming the Sun*. The MIT Press, 2018.

[5] David Carroll. *Australian town powered 100% by solar PV and battery*.

[6] Ralph Diermann. *PV can cover almost half of typical office buildings' electricity demand*.

[7] *Land Art Generator: http://landartgenerator.org/project.html*.

[8] Kunta Yoshikawa et al. "Silicon heterojunction solar cell with interdigitated back contacts for a photoconversion efficiency over 26%." In: *Nature Energy* 2.5 (2017).

[9] Matthew S. Branham et al. "15.7% Efficient 10-μm-Thick Crystalline Silicon Solar Cells Using Periodic Nanostructures." In: *Advanced Materials* 27.13 (2015), pp. 2182–2188.

[10] Hung Ling Chen et al. "A 19.9%-efficient ultrathin solar cell based on a 205-nm-thick GaAs absorber and a silver nanostructured back mirror." In: *Nature Energy* 4.9 (2019), pp. 761–767.

[11] B. Vermang et al. "Employing Si solar cell technology to increase efficiency of ultra-thin Cu(In,Ga)Se2 solar cells." In: *Progress in Photovoltaics: Research and Applications* 22.10 (2014), pp. 1023–1029.

[12] Jason Svarc. *Most efficient solar panels*. 2021.

[13] Christopher J. Traverse et al. "Emergence of highly transparent photovoltaics for distributed applications." In: *Nature Energy* 2.11 (2017), pp. 849–860.

[14] Verena Neder, Stefan L. Luxembourg, and Albert Polman. "Efficient colored silicon solar modules using integrated resonant dielectric nanoscatterers." In: *Applied Physics Letters* 111.7 (2017).

[15] Justin Henrie et al. "Electronic color charts for dielectric films on silicon." In: *Optics Express* 12.7 (2004), p. 1464.

[16] Yu Liu and Tomoyuki Miyamoto. "Optical wireless power transmission characteristics of surface appearance controlled solar cells using visible colour filters." In: *The Journal of Engineering* 2021.1 (2021), pp. 19–24.

[17] Nils Neugebohrn et al. "Multifunctional metal oxide electrodes: Colour for thin film solar cells." In: *Thin Solid Films* 685 (2019), pp. 131–135.

[18] Minghua Li et al. "Realization of colored multicrystalline silicon solar cells with SiO2/SiNx:H double layer antireflection coatings." In: *International Journal of Photoenergy* (2013).

[19] Evan Franklin et al. "Sliver solar cells: High-efficiency, low-cost PV technology." In: *Advances in OptoElectronics* (2007).

[20] Nandar Lynn, Lipi Mohanty, and Stephen Wittkopf. "Color rendering properties of semi-transparent thin-film PV modules." In: *Building and Environment* 54 (2012), pp. 148–158.

[21] Giles E. Eperon et al. "Neutral Color Semitransparent Microstructured Perovskite Solar Cells." In: *ACS Nano* 8.1 (2014), pp. 591–598.

[22] Malkeshkumar Patel et al. "Excitonic metal oxide heterojunction (NiO/ZnO) solar cells for all-transparent module integration." In: *Solar Energy Materials and Solar Cells* 170 (2017), pp. 246–253.

[23] Dianyi Liu, Chenchen Yang, and Richard R. Lunt. "Halide Perovskites for Selective Ultraviolet-Harvesting Transparent Photovoltaics." In: *Joule* 2.9 (2018), pp. 1827–1837.

[24] Yi Hong Chen et al. "Microcavity-embedded, colour-tuneable, transparent organic solar cells." In: *Advanced Materials* 26.7 (2014), pp. 1129–1134.

[25] Mushfika Baishakhi Upama et al. "Low-temperature processed efficient and colourful semitransparent perovskite solar cells for building integration and tandem applications." In: *Organic Electronics* 65 (2019), pp. 401–411.

[26] Xiao Luo et al. "Quantum-Cutting Luminescent Solar Concentrators Using Ytterbium-Doped Perovskite Nanocrystals." In: *Nano Letters* 19.1 (2019), pp. 338–341.

[27] Yimu Zhao et al. "Near-infrared harvesting transparent luminescent solar concentrators." In: *Advanced Optical Materials* 2.7 (2014), pp. 606–611.

[28] Chenchen Yang et al. "High-Performance Near-Infrared Harvesting Transparent Luminescent Solar Concentrators." In: *Advanced Optical Materials* 8.8 (2020).

[29] Raquel Rondão et al. "High-Performance Near-Infrared Luminescent Solar Concentrators." In: *ACS Applied Materials and Interfaces* 9.14 (2017), pp. 12540–12546.

[30] Jun Ho Yum et al. "Blue-coloured highly efficient dye-sensitized solar cells by implementing the diketopyrrolopyrrole chromophore." In: *Scientific Reports* 3 (2013), pp. 1–8.

[31] Samuel De Sousa et al. "Tuning visible-light absorption properties of Ru-diacetylide complexes: Simple access to colorful efficient dyes for DSSCs." In: *Journal of Materials Chemistry A* 3.35 (2015), pp. 18256–18264.

[32] Yang Chen et al. "Semiconductor nanowire array for transparent photovoltaic applications." In: *Applied Physics Letters* 118.19 (2021).

[33] Zhenpeng Li et al. "Transparent and Colored Solar Photovoltaics for Building Integration." In: *Solar RRL* 5.3 (2021).

[34] Dick Van Dam. "Nanowire Photonics for Photovoltaics." PhD thesis. 2016.

[35] Josef A. Czaban, David A. Thompson, and Ray R. LaPierre. "GaAs core-shell nanowires for photovoltaic applications." In: *Nano Letters* 9.1 (2009), pp. 148–154.

[36] Bozhi Tian et al. "Coaxial silicon nanowires as solar cells and nanoelectronic power sources." In: *Nature* 449.7164 (2007), pp. 885–889.

[37] Michael D. Kelzenberg et al. "Photovoltaic measurements in single-nanowire silicon solar cells." In: *Nano Letters* 8.2 (2008), pp. 710–714.

[38] Erik C. Garnett and Peidong Yang. "Silicon nanowire radial p-n junction solar cells." In: *Journal of the American Chemical Society* 130.29 (2008), pp. 9224–9225.

[39] Hajime Goto et al. "Growth of core-shell inP nanowires for photovoltaic application by selective-area metal organic vapor phase epitaxy." In: *Applied Physics Express* 2.3 (2009).

[40] Peter Krogstrup et al. "Single-nanowire solar cells beyond the Shockley–Queisser limit." In: *Nature Photonics* 7.4 (2013), pp. 306–310.

[41] Erik Garnett and Peidong Yang. "Light trapping in silicon nanowire solar cells." In: *Nano Letters* 10.3 (2010), pp. 1082–1087.

[42] N. Anttu and H. Q. Xu. "Coupling of light into nanowire arrays and subsequent absorption." In: *Journal of Nanoscience and Nanotechnology* 10.11 (2010), pp. 7183–7187.

[43] Marcel A. Verheijen et al. "Growth kinetics of heterostructured GaP-GaAs nanowires." In: *Journal of the American Chemical Society* 128.4 (2006), pp. 1353–1359.

[44] Premila Mohan, Junichi Motohisa, and Takashi Fukui. "Fabrication of InPInAsInP core-multishell heterostructure nanowires by selective area metalorganic vapor phase epitaxy." In: *Applied Physics Letters* 88.13 (2006), pp. 1–4.

[45] Magnus Heurlin et al. "Axial InP nanowire tandem junction grown on a silicon substrate." In: *Nano Letters* 11.5 (2011), pp. 2028–2031.

[46] G. E. Cirlin et al. "Photovoltaic properties of p-Doped GaAs nanowire arrays grown on n-Type GaAs(111)B substrate." In: *Nanoscale Research Letters* 5.2 (2010), pp. 360–363.

[47] Giacomo Mariani et al. "Patterned radial GaAs nanopillar solar cells." In: *Nano Letters* 11.6 (2011), pp. 2490–2494.

[48] Giacomo Mariani et al. "GaAs nanopillar-array solar cells employing in situ surface passivation." In: *Nature Communications* 4 (2013).

[49] Maoqing Yao et al. "GaAs nanowire array solar cells with axial p-i-n junctions." In: *Nano Letters* 14.6 (2014), pp. 3293–3303.

[50] Ingvar Aberg et al. "A GaAs nanowire array solar cell with 15.3% efficiency at 1 sun." In: *IEEE Journal of Photovoltaics* 6.1 (2016), pp. 185–190.

[51] Takashi Fukui et al. "Position-controlled III-V compound semiconductor nanowire solar cells by selective-area metal-organic vapor phase epitaxy." In: *Ambio* 41 (2012), pp. 119–124.

[52] Mays El-Dairi and Robert James House. *Optic nerve hypoplasia*. 2019.

[53] Gaute Otnes et al. "Understanding InP Nanowire Array Solar Cell Performance by Nanoprobe-Enabled Single Nanowire Measurements." In: *Nano Letters* 18.5 (2018), pp. 3038–3046.

[54] Dick Van Dam et al. "High-Efficiency Nanowire Solar Cells with Omnidirectionally Enhanced Absorption Due to Self-Aligned Indium-Tin-Oxide Mie Scatterers." In: *ACS Nano* 10.12 (2016), pp. 11414–11419.

[55] Vidur Raj et al. "High-efficiency solar cells from extremely low minority carrier lifetime substrates using radial junction nanowire architecture." In: *ACS Nano* 13.10 (2019), pp. 12015–12023.

[56] Keiichi Haraguchi et al. "GaAs p-n junction formed in quantum wire crystals." In: *Applied Physics Letters* 60.6 (1992), pp. 745–747.

[57] Yijing Wu, Haoquan Yan, and Peidong Yang. "Semiconductor Nanowire Array: Potential Substrates for Photocatalysis and Photovoltaics." In: *Topics in Catalysis* 19.2 (2002), pp. 197–202.

[58] L. Tsakalakos et al. "Silicon nanowire solar cells." In: *Applied Physics Letters* 91.23 (2007), pp. 1–4.

[59] Albert Polman et al. "Photovoltaic materials: Present efficiencies and future challenges." In: *Science* 352.6283 (2016), p. 307.

[60] Vidur Raj et al. "Design Principles for Fabrication of InP-Based Radial Junction Nanowire Solar Cells Using an Electron Selective Contact." In: *IEEE J. Photovoltaics* 9.4 (2019), pp. 980–991.

[61] Jos E M Haverkort et al. "Fundamentals of the nanowire solar cell : Optimization of the open circuit voltage." In: *Applied Physics Reviews* 031106 (2018).

[62] Martin A. Green et al. "Solar cell efficiency tables (Version 53)." In: *Progress in Photovoltaics: Research and Applications* 27.1 (2019), pp. 3–12.

[63] Alexander Dorodnyy et al. "Efficient Multiterminal Spectrum Splitting via a Nanowire Array Solar Cell." In: *ACS Photonics* 2.9 (2015), pp. 1284–1288.

[64] N. Tavakoli and E. Alarcon-Llado. "Combining 1D and 2D waveguiding in an ultrathin GaAs NW/Si tandem solar cell." In: *Optics Express* 27.12 (2019).

[65] Oliver Hayden, Ritesh Agarwal, and Charles M. Lieber. "Nanoscale avalanche photodiodes for highly sensitive and spatially resolved photon detection." In: *Nature Materials* 5.5 (2006), pp. 352–356.

[66] C. Soci et al. "ZnO Nanowire UV Photodetectors with High Internal Gain." In: *Nano Letters* 7.4 (2007), pp. 1003–1009.

[67] Wenjin Luo et al. "Room-Temperature Single-Photon Detector Based on Single Nanowire." In: *Nano Letters* 18.9 (2018), pp. 5439–5445.

[68] Michael H. Huang. "Room-Temperature Ultraviolet Nanowire Nanolasers." In: *Science* 292.5523 (2001), pp. 1897–1899.

[69] Dhruv Saxena et al. "Optically pumped room-temperature GaAs nanowire lasers." In: *Nature Photonics* 7.12 (2013), pp. 963–968.

[70] Zhiyong Fan et al. "Large-scale, heterogeneous integration of nanowire arrays for image sensor circuitry." In: *PNAS* 105.32 (2008), pp. 11066–11070.

[71] Grzegorz Grzela, Djamila Hourlier, and Jaime Gómez Rivas. "Polarization-dependent light extinction in ensembles of polydisperse vertical semiconductor nanowires: A Mie scattering effective medium." In: *Physical Review B* 86 (4 2012), p. 045305.

[72] Grzegorz Grzela et al. "Nanowire antenna absorption probed with time-reversed fourier microscopy." In: *Nano Letters* 14.6 (2014).

[73] Yaoguang Ma et al. "Semiconductor nanowire lasers." In: *Advances in Optics and Photonics* 5.3 (2013), pp. 216–273.

[74] Allan W. Snyder and J. D. Love. *Optical waveguide theory*. Chapman and Hall, 1983, p. 734.

[75] Katherine T. Fountaine, W. Whitney, and Harry a Atwater. "Resonant absorption in semiconductor nanowires and nanowire arrays: Relating leaky waveguide modes to Bloch photonic crystal modes." In: *Journal of Applied Physics* 116 (2014), p. 153106.

[76] Linyou Cao et al. "Engineering light absorption in semiconductor nanowire devices." In: *Nature Materials* 8.8 (2009), pp. 643–647.

[77] Grzegorz Grzela. "Directional Light Emission and Absorption by Semiconductor Nanowires." PhD thesis. 2013.

[78] Anne-Line Henneghien et al. "Simulation of waveguiding and emitting properties of semiconductor nanowires with hexagonal or circular sections." In: *Journal of the Optical Society of America B* 26.12 (2009), pp. 2396–2403.

[79] Rune Frederiksen et al. "Visual Understanding of Light Absorption and Waveguiding in Standing Nanowires with 3D Fluorescence Confocal Microscopy." In: *ACS Photonics* 4 (2017), p. 2235.

[80] M. Heiss et al. "III-V nanowire arrays: Growth and light interaction." In: *Nanotechnology* 25.1 (2014).

[81] J van de Groep and A Polman. "Designing dielectric resonators on substrates: Combining magnetic and electric resonances." In: *Optics Express* 21.22 (2013), pp. 26285–26302.

[82] Nicklas Anttu et al. "Absorption of light in InP nanowire arrays." In: *Nano Research* 7.6 (2014), pp. 816–823.

[83] Nicklas Anttu et al. "Absorption and transmission of light in III-V nanowire arrays for tandem solar cell applications." In: *Nanotechnology* 28.20 (2017), p. 205203.

[84] Eric Johlin et al. "Super-resolution imaging of light–matter interactions near single semiconductor nanowires." In: *Nature Communications* 7.1 (2016), p. 13950.

[85] Damiano Verardo et al. "Nanowires for Biosensing: Lightguiding of Fluorescence as a Function of Diameter and Wavelength." In: *Nano Letters* 18.8 (2018), pp. 4796–4802.

[86] Shinya Inoué. "Foundations of Confocal Scanned Imaging in Light Microscopy." In: *Pawley J. (eds) Handbook Of Biological Confocal Microscopy*. Springer, 2006.

[87] *Energiemaatregelen: https://www.cultureelerfgoed.nl/onderwerpen/energie-en-landschap/zonne-en-windenergie*.

[88] P Eiffert and G J Kiss. *Building-Integrated Photovoltaic Designs for Commercial and Institutional Structures A Sourcebook for Architects*. Diane Publishing Co., 2000.

[89] Ondrej Filip et al. "Food versus fuel: An updated and expanded evidence." In: *Energy Economics* 82 (2019), pp. 152–166.

[90] Osbel Almora et al. "Device Performance of Emerging Photovoltaic Materials (Version 1)." In: *Advanced Energy Materials* 11.11 (2021), p. 2002774.

[91] Richard R. Lunt. "Theoretical limits for visibly transparent photovoltaics." In: *Applied Physics Letters* 101.4 (2012), p. 43902.

[92] Viktor V. Brus et al. "Solution-Processed Semitransparent Organic Photovoltaics: From Molecular Design to Device Performance." In: *Advanced Materials* 31.30 (2019), p. 1900904.

[93] Stav Rahmany and Lioz Etgar. "Semitransparent Perovskite Solar Cells." In: *ACS Energy Lett.* 5.5 (2020), pp. 1519–1531.

[94] Biao Shi et al. "Semitransparent Perovskite Solar Cells: From Materials and Devices to Applications." In: *Advanced Materials* 32.3 (2020), p. 1806474.

[95] J. Sun and J. J. Jasieniak. "Semi-transparent solar cells." In: *Journal of Physics D: Applied Physics* 50.9 (2017), p. 093001.

[96] Nicklas Anttu and H Q Xu. "Efficient light management in vertical nanowire arrays for photovoltaics." In: *Optics express* 21 Suppl 3 (2013), A558–75.

[97] Jesper Wallentin et al. "InP nanowire array solar cells achieving 13.8% efficiency by exceeding the ray optics limit." In: *Science (New York, N.Y.)* 339.6123 (2013), pp. 1057–60.

[98] Hyunsung Park and Kenneth B. Crozier. "Multispectral imaging with vertical silicon nanowires." In: *Scientific Reports* 3 (2013), pp. 1–6.

[99] Michael D Kelzenberg et al. "Enhanced absorption and carrier collection in Si wire arrays for photovoltaic applications." In: *Nature materials* 9.3 (2010), pp. 239–44.

[100] Zhiyong Fan et al. "Three-dimensional nanopillar-array photovoltaics on low-cost and flexible substrates." In: *Nature Materials* 8.8 (2009), pp. 648–53.

[101] Baomin Wang and Paul W Leu. "Tunable and selective resonant absorption in vertical nanowires." In: *Optics Letters* 37.18 (2012), pp. 3756–3758.

[102] Sudha Mokkapati et al. "Optical design of nanowire absorbers for wavelength selective photodetectors." In: *Scientific Reports* 5 (2015), p. 15339.

[103] Phillip M Wu et al. "Colorful InAs Nanowire Arrays : From Strong to Weak Absorption." In: *Nano Letters* 12 (2012), p. 1990.

[104] Yang Chen, Mats-Erik Pistol, and Nicklas Anttu. "Design for strong absorption in a nanowire array tandem solar cell." In: *Scientific Reports* 6.1 (2016), p. 32349.

[105] Sung Bum Kang et al. "Stretchable and colorless freestanding microwire arrays for transparent solar cells with flexibility." In: *Light: Science and Applications* 8.1 (2019).

[106] Chenchen Yang et al. "How to Accurately Report Transparent Solar Cells." In: *Joule* 3.8 (2019), pp. 1803–1809.

[107] Pilar Espinet-Gonzalez et al. "Radiation Tolerant Nanowire Array Solar Cells." In: *ACS Nano* 13.11 (2019), pp. 12860–12869.

[108] Zhiqin Zhong et al. "Efficiency enhancement of axial junction InP single nanowire solar cells by dielectric coating." In: *Nano Energy* 28 (2016), pp. 106–114.

[109] P Fisette. "Windows: Understanding Energy Efficient Performance." In: *University of Massachusetts* (2003).

[110] *Colour Matching Functions: http://cvrl.ioo.ucl.ac.uk/cmfs.htm*.

[111] Omid Madani Ghahfarokhi et al. "Performance of GaAs Nanowire Array Solar Cells for Varying Incidence Angles." In: *IEEE Journal of Photovoltaics* 6.6 (2016), pp. 1502–1508.

[112] E.D. Palik. *Handbook of optical constants of solids*. 1998.

[113] Zhe Liu et al. "Revisiting thin silicon for photovoltaics: a technoeconomic perspective." In: *Energy & Environmental Science* 13 (1 2020), pp. 12–23.

[114] Alexander I. Fedorchenko, An Bang Wang, and Henry H. Cheng. "Thickness dependence of nanofilm elastic modulus." In: *Applied Physics Letters* 94.15 (2009), p. 152111.

[115] Shuang Wang et al. "Large-area free-standing ultrathin single-crystal silicon as processable materials." In: *Nano Letters* 13.9 (2013), pp. 4393–4398.

[116] Jae Hoon Bong et al. "A quantitative strain analysis of a flexible single-crystalline silicon membrane." In: *Applied Physics Letters* 110.3 (2017), p. 033105.

[117] Armin Richter, Martin Hermle, and Stefan W. Glunz. "Reassessment of the limiting efficiency for crystalline silicon solar cells." In: *IEEE Journal of Photovoltaics* 3.4 (2013), pp. 1184–1191.

[118] Piotr Kowalczewski and Lucio Claudio Andreani. "Towards the efficiency limits of silicon solar cells: How thin is too thin?" In: *Solar Energy Materials and Solar Cells* 143 (2015), pp. 260–268.

[119] Albert Polman and Harry A. Atwater. "Photonic design principles for ultrahigh-efficiency photovoltaics." In: *Nature Materials* 11.3 (2012), pp. 174–177.

[120] Ragip A. Pala et al. "Design of plasmonic thin-film solar cells with broadband absorption enhancements." In: *Advanced Materials* 21.34 (2009), pp. 3504–3509.

[121] Peng Yu et al. "Giant optical pathlength enhancement in plasmonic thin film solar cells using core-shell nanoparticles." In: *Journal of Physics D: Applied Physics* 51.29 (2018), p. 295106.

[122] Waseem Raja et al. "Broadband absorption enhancement in plasmonic nanoshells-based ultrathin microcrystalline-Si solar cells." In: *Scientific Reports* 6.1 (2016), p. 24539.

[123] Vivian E. Ferry et al. "Plasmonic Nanostructure Design for Efficient Light Coupling into Solar Cells." In: *Nano Letters* 8.12 (2008), pp. 4391–4397.

[124] Hung-Ling Chen et al. "A 19.9%-efficient ultrathin solar cell based on a 205-nm-thick GaAs absorber and a silver nanostructured back mirror." In: *Nature Energy* 4.9 (2019), pp. 761–767.

[125] Guillaume Gomard et al. "Two-dimensional photonic crystal for absorption enhancement in hydrogenated amorphous silicon thin film solar cells." In: *Journal of Applied Physics* 108.12 (2010), p. 123102.

[126] Corsin Battaglia et al. "Light Trapping in Solar Cells: Can Periodic Beat Random?" In: *ACS Nano* 6.3 (2012), pp. 2790–2797.

[127] Guanchao Yin et al. "Optoelectronic Enhancement of Ultrathin CuIn 1 – x Ga x Se 2 Solar Cells by Nanophotonic Contacts." In: *Advanced optical Materials* 5 (2017), p. 1600637.

[128] K. Jäger et al. "A scattering model for nano-textured interfaces and its application in opto-electrical simulations of thin-film silicon solar cells." In: *Journal of Applied Physics* 111.8 (2012), p. 083108.

[129] Emiliano R. Martins et al. "Deterministic quasi-random nanostructures for photon control." In: *Nature Communications* 4 (2013), pp. 1–7.

[130] Kevin Vynck et al. "Photon management in two-dimensional disordered media." In: *Nature Materials* 11.12 (2012), pp. 1017–1022.

[131] Ardavan Oskooi et al. "Partially disordered photonic-crystal thin films for enhanced and robust photovoltaics." In: *Applied Physics Letters* 100.18 (2012), p. 181110.

[132] Vivian E. Ferry et al. "Optimized spatial correlations for broadband light trapping nanopatterns in high efficiency ultrathin film a-Si:H solar cells." In: *Nano Letters* 11.10 (2011), pp. 4239–4245.

[133] Claire Van Lare et al. "Dielectric Scattering Patterns for Efficient Light Trapping in Thin-Film Solar Cells." In: *Nano Letters* 15.8 (2015), pp. 4846–4852.

[134] Shuangcheng Yu et al. "Design of Non-Deterministic Quasi-random Nanophotonic Structures Using Fourier Space Representations." En. In: *Scientific Reports* 7.1 (2017), p. 3752.

[135] Filippo Pratesi et al. "Disordered photonic structures for light harvesting in solar cells." en. In: *Optics Express* 21.S3 (2013), A460.

[136] Radwanul H. Siddique et al. "Bioinspired phase-separated disordered nanostructures for thin photovoltaic absorbers." In: *Science Advances* 3.10 (2017), e1700232.

[137] Angelo Bozzola, Marco Liscidini, and Lucio Claudio Andreani. "Broadband light trapping with disordered photonic structures in thin-film silicon solar cells." In: *Progress in Photovoltaics: Research and Applications* 22.12 (2014), pp. 1237–1245.

[138] Jacob Trevino et al. "Plasmonic-photonic arrays with aperiodic spiral order for ultra-thin film solar cells." en. In: *Optics Express* 20.S3 (2012), A418.

[139] Salvatore Torquato and Frank H. Stillinger. "Local density fluctuations, hyperuniformity, and order metrics." In: *Physical Review E* 68.4 (2003), p. 041113.

[140] Obioma U. Uche, Frank H. Stillinger, and Salvatore Torquato. "Constraints on collective density variables: Two dimensions." In: *Physical Review E* 70 (4 2004), p. 046122.

[141] Robert D. Batten, Frank H. Stillinger, and Salvatore Torquato. "Classical disordered ground states: Super-ideal gases and stealth and equi-luminous materials." In: *Journal of Applied Physics* 104.3 (2008), p. 33504.

[142] Marta Castro-Lopez et al. "Reciprocal space engineering with hyperuniform gold disordered surfaces." In: *APL Photonics* 2.6 (2017).

[143] Andrea Gabrielli et al. *Statistical Physics for Cosmic Structures*. en. Berlin Heidelberg: Springer-Verlag, 2005.

[144] G Zhang, F Martelli, and S Torquato. "The structure factor of primes." In: *Journal of Physics A: Mathematical and Theoretical* 51.11 (2018), p. 115001.

[145] Qun-Li Lei and Ran Ni. "Hydrodynamics of random-organizing hyperuniform fluids." en. In: *Proceedings of the National Academy of Sciences* 116.46 (2019), pp. 22983–22989.

[146] Fausto Martelli et al. "Large-Scale Structure and Hyperuniformity of Amorphous Ices." In: *Physical Review Letters* 119 (13 2017), p. 136002.

[147] Jikai Wang, J. M. Schwarz, and Joseph D. Paulsen. "Hyperuniformity with no fine tuning in sheared sedimenting suspensions." en. In: *Nature Communications* 9.1 (2018), pp. 1–7.

[148] Luis S. Froufe-Pérez et al. "Band gap formation and Anderson localization in disordered photonic materials with structural correlations." en. In: *Proceedings of the National Academy of Sciences* 114.36 (2017), pp. 9570–9574.

[149] Joshua Ricouvier et al. "Optimizing Hyperuniformity in Self-Assembled Bidisperse Emulsions." In: *Physical Review Letters* 119 (20 2017), p. 208001.

[150] Marian Florescu, Salvatore Torquato, and Paul J. Steinhardt. "Designer disordered materials with large, complete photonic band gaps." en. In: *PNAS* 106.49 (2009), pp. 20658–20663.

[151] Luis S. Froufe-Pérez et al. "The Role of Short-Range Order and Hyperuniformity in the Formation of Band Gaps in Disordered Photonic Materials." In: *Physical Review Letters* 117.5 (2016). arXiv: 1602.01002.

[152] Samuel Tsitrin et al. "Unfolding the band structure of non-crystalline photonic band gap materials." In: *Scientific Reports* 5 (2015), p. 13301.

[153] O. Leseur, R. Pierrat, and R. Carminati. "High-density hyperuniform materials can be transparent." In: *Optica* 3.7 (2016), pp. 763–767.

[154] S. Gorsky et al. "Engineered hyperuniformity for directional light extraction." In: *APL Photonics* 4.11 (2019), p. 110801.

[155] Milan M. Milošević et al. "Hyperuniform disordered waveguides and devices for near infrared silicon photonics." en. In: *Scientific Reports* 9.1 (2019), pp. 1–11.

[156] Weining Man et al. "Isotropic band gaps and freeform waveguides observed in hyperuniform disordered photonic solids." en. In: *PNAS* 110.40 (2013), pp. 15886–15891.

[157] Timothy Amoah and Marian Florescu. "High-Q optical cavities in hyperuniform disordered materials." In: *Physical Review B* 91.2 (2015), p. 020201.

[158] Tian Ma et al. "3D Printed Hollow-Core Terahertz Optical Waveguides with Hyperuniform Disordered Dielectric Reflectors." en. In: *Advanced Optical Materials* 4.12 (2016), pp. 2085–2094.

[159] Wen Zhou et al. "Hyperuniform disordered photonic bandgap polarizers." In: *Journal of Applied Physics* 126.11 (2019), p. 113106.

[160] Helen Ghiradella. "Light and color on the wing: structural colors in butterflies and moths." In: *Applied Optics* 30.24 (1991), p. 3492.

[161] Timo Gissibl et al. "Refractive index measurements of photo-resists for three-dimensional direct laser writing." In: *Optical Materials Express* 7.7 (2017), p. 2293.

[162] Sander A. Mann et al. "Quantifying losses and thermodynamic limits in nanophotonic solar cells." In: *Nature Nanotechnology* 11.12 (2016), pp. 1071–1075.

[163] Sander A. Mann et al. "Integrating Sphere Microscopy for Direct Absorption Measurements of Single Nanostructures." In: *ACS Nano* 11.2 (2017), pp. 1412–1418.

[164] Valérie Depauw et al. "Sunlight-thin nanophotonic monocrystalline silicon solar cells." In: *Nano Futures* 1.2 (2017), p. 021001.

[165] Angelo Bozzola, Marco Liscidini, and Lucio Claudio Andreani. "Broadband light trapping with disordered photonic structures in thin-film silicon solar cells." en. In: *Prog. Photovolt: Res. Appl.* 22.12 (2014), pp. 1237–1245.

[166] Juntao Li et al. "Spatial resolution effect of light coupling structures." In: *Scientific Reports* 5 (2015), p. 18500.

[167] Miroslav Hejna, Paul J. Steinhardt, and Salvatore Torquato. "Nearly hyperuniform network models of amorphous silicon." In: *Physical Review B* 87.24 (2013), p. 245204.

[168] A. Hinke Schokker and A. Femius Koenderink. "Lasing at the band edges of plasmonic lattices." In: *Physical Review B* 90.15 (Oct. 2014), p. 155452.

[169] M. Teubner. "Level Surfaces of Gaussian Random Fields and Microemulsions." en. In: *EPL* 14.5 (1991), p. 403.

[170] Zheng Ma and Salvatore Torquato. "Random scalar fields and hyperuniformity." en. In: *Journal of Applied Physics* 121.24 (2017), p. 244904.

[171] Kunta Yoshikawa et al. "Silicon heterojunction solar cell with interdigitated back contacts for a photoconversion efficiency over 26%." In: *Nature Energy* 2.5 (2017), pp. 1–8.

[172] Sangmoo Jeong, Michael D. McGehee, and Yi Cui. "All-back-contact ultra-thin silicon nanocone solar cells with 13.7% power conversion efficiency." In: *Nature Communications* 4.1 (2013), pp. 1–7.

[173] Andrea Tomasi et al. "Simple processing of back-contacted silicon heterojunction solar cells using selective-area crystalline growth." In: *Nature Energy* 2.5 (2017), pp. 1–8.

[174] Hitoshi Sai et al. "Impact of silicon wafer thickness on photovoltaic performance of crystalline silicon heterojunction solar cells." In: *Japan Society of Applied Physics* 57.8 (2018).

[175] B. Bläsi et al. "Large area patterning using interference and nanoimprint lithography." In: *SPIE Proceedings Volume 9888, Micro-Optics* (2016). Ed. by Hugo Thienpont et al., pp. 80–88.

[176] Yidenekachew J. Donie et al. "Light trapping in thin film silicon solar cells via phase separated disordered nanopillars." In: *Nanoscale* 10 (2018), pp. 6651–6659.

[177] Peter M. Piechulla et al. "Fabrication of Nearly-Hyperuniform Substrates by Tailored Disorder for Photonic Applications." In: *Advanced Optical Materials* 6.7 (2018), pp. 1–10.

[178] Marco Salvalaglio et al. *Hyperuniform monocrystalline structures by spinodal solid-state dewetting*. 2019.

[179] M A Verschuuren et al. "Nanoscale spatial limitations of large-area substrate conformal imprint lithography." In: *Nanotechnology* 30.34 (2019), p. 345301.

[180] Ardavan F. Oskooi et al. "Meep: A flexible free-software package for electromagnetic simulations by the FDTD method." In: *Computer Physics Communications* 181.3 (2010), pp. 687–702.

[181] Edward Y. Wang et al. "Optimum design of antireflection coating for silicon solar cells." In: *10th IEEE Photovoltaic Specialists Conference.* (1974).

[182] Edward D. Palik, ed. *Handbook of optical constants of solids II*. Boston: Academic Press, 1991.

[183] Zongfu Yu, Aaswath Raman, and Shanhui Fan. "Fundamental limit of nanophotonic light trapping in solar cells." en. In: *PNAS* 107.41 (2010), pp. 17491–17496.

[184] Martin A. Green. "Lambertian light trapping in textured solar cells and light-emitting diodes: analytical solutions." en. In: *Prog. Photovolt: Res. Appl.* 10.4 (2002), pp. 235–241.

[185] Zhe Liu et al. "Revisiting thin silicon for photovoltaics: a technoeconomic perspective." In: *Energy & Environmental Science* (2020).

[186] Frank Glas. "Critical dimensions for the plastic relaxation of strained axial heterostructures in free-standing nanowires." In: *Physical Review B - Condensed Matter and Materials Physics* 74.12 (2006), pp. 2–5.

[187] Eleonora Russo-Averchi et al. "Suppression of three dimensional twinning for a 100% yield of vertical GaAs nanowires on silicon." In: *Nanoscale* 4.5 (2012), pp. 1486–90.

[188] Thomas Mårtensson et al. "Epitaxial III-V nanowires on silicon." In: *Nano Letters* 4.10 (2004), pp. 1987–1990.

[189] Hyunseok Kim et al. "Monolithically Integrated InGaAs Nanowires on 3D Structured Silicon-on-Insulator as a New Platform for Full Optical Links." In: *Nano Letters* 16.3 (2016), pp. 1833–1839.

[190] Peter Krogstrup et al. "Structural phase control in self-catalyzed growth of GaAs nanowires on silicon (111)." In: *Nano Letters* 10.11 (2010), pp. 4475–4482.

[191] Mattias Borg et al. "Vertical III-V nanowire device integration on Si(100)." In: *Nano letters* 14.4 (2014), pp. 1914–20.

[192] Linus C. Chuang et al. "Critical diameter for III-V nanowires grown on lattice-mismatched substrates." In: *Applied Physics Letters* 90.4 (2007), pp. 2005–2008.

[193] C. Colombo et al. "Ga-assisted catalyst-free growth mechanism of GaAs nanowires by molecular beam epitaxy." In: *Physical Review B* 77.15 (2008), p. 155326.

[194] Lu Hu and Gang Chen. "Analysis of optical absorption in silicon nanowire arrays for photovoltaic applications." In: *Nano letters* 7.11 (2007), pp. 3249–52.

[195] Katherine T Fountaine, Christian G Kendall, and Harry A Atwater. "Near-unity broadband absorption designs for semiconducting nanowire arrays via localized radial mode excitation." In: *Optics Express* 22 (2014), A930.

[196] Ningfeng Huang, Chenxi Lin, and Michelle L Povinelli. "Broadband absorption of semiconductor nanowire arrays for photovoltaic applications." In: *Journal of Optics* 14.2 (2012), p. 024004.

[197] Inho Kim et al. "Silicon nanodisk array design for effective light trapping in ultrathin c-Si." In: *Optics Express* 22.S6 (2014), A1431.

[198] Chenxi Lin, Luis Javier Martínez, and Michelle L. Povinelli. "Experimental broadband absorption enhancement in silicon nanohole structures with optimized complex unit cells." In: *Optics Express* 21.S5 (2013), A872.

[199] Christos Trompoukis et al. "Photonic assisted light trapping integrated in ultrathin crystalline silicon solar cells by nanoimprint lithography." In: *Applied Physics Letters* 101.10 (2012), pp. 1–5.

[200] Alexandre Gaucher et al. "Ultrathin Epitaxial Silicon Solar Cells with Inverted Nanopyramid Arrays for Efficient Light Trapping." In: *Nano Letters* 16.9 (2016), pp. 5358–5364.

[201] Ken Xingze Wang et al. "Absorption Enhancement in Ultrathin Crystalline Silicon Solar Cells with Antireflection and Light-Trapping Nanocone Gratings." In: *Nano letters* 12 (2012), p. 1616.

[202] Long Wen et al. "Theoretical consideration of III – V nanowire / Si triple-junction solar cells." In: *Nanotechnology* 23 (2012), p. 505202.

[203] Y Wang et al. "Design High-Efficiency III – V Nanowire / Si Two-Junction Solar Cell." In: *Nanoscale Research Letters* 10 (2015), p. 269.

[204] R R LaPierre. "Theoretical conversion efficiency of a two-junction III-V nanowire on Si solar cell." In: *Journal of Applied Physics* 110.1 (2011), p. 014310.

[205] Abdennacer Benali et al. "Optical simulation of multijunction solar cells based on III-V nanowires on silicon." In: *Energy Procedia* 60.May (2014), pp. 109–115.

[206] Y Chen et al. "Optical analysis of a III-V-nanowire-array-on-Si dual junction solar cell." In: *Optics Express* 25.16 (2017), pp. 3293–3303.

[207] Ningfeng Huang et al. "Limiting efficiencies of tandem solar cells consisting of III-V nanowire arrays on silicon Limiting efficiencies of tandem solar cells consisting of III-V nanowire arrays on silicon." In: *Journal of Applied Physics* 064321 (2013).

[208] Maoqing Yao et al. "Tandem Solar Cells Using GaAs Nanowires on Si: Design, Fabrication, and Observation of Voltage Addition." In: *Nano Letters* 15 (2015), p. 7217.

[209] B Wood et al. "GaAsP nanowire-on-Si tandem solar cell." In: *Journal of Photonics for Energy* 7 (2017), p. 042502.

[210] Chenxi Lin, Ningfeng Huang, and Michelle L Povinelli. "Effect of aperiodicity on the broadband reflection of silicon nanorod structures for photovoltaics." In: *Optics express* 20.1 (2012), pp. 125–132.

[211] A. Mellor et al. "Upper limits to absorption enhancement in thick solar cells using diffraction gratings." In: *Progress in Photovoltaics: Research and Applications* 19 (2011), p. 676.

[212] S. Mokkapati et al. "Designing periodic arrays of metal nanoparticles for light-trapping applications in solar cells." In: *Applied Physics Letters* 95.5 (2009), pp. 93–96.

[213] Eli Yablonovitch. "Statistical ray optics." In: *Journal of the Optical Society of America* 72.7 (1982), pp. 899–907.

[214] Tom Markvart. "Beyond the Yablonovitch limit: Trapping light by frequency shift." In: *Applied Physics Letters* 98.7 (2011), pp. 7–9.

[215] Ardavan Oskooi, Yoshinori Tanaka, and Susumu Noda. "Tandem photonic-crystal thin films surpassing Lambertian light-trapping limit over broad bandwidth and angular range." In: *Applied Physics Letters* 104.9 (2014).

[216] Joydeep Bhattacharya et al. "A photonic-plasmonic structure for enhancing light absorption in thin film solar cells." In: *Applied Physics Letters* 99.13 (2011), pp. 2009–2012.

[217] Sang Eon Han and Gang Chen. "Toward the Lambertian Limit of Light Trapping in Thin Nanostructured Silicon Solar Cells." In: *Nano Letters* 10.11 (2010), pp. 4692–4696.

[218] Zongfu Yu, Aaswath Raman, and Shanhui Fan. "Fundamental limit of light trapping in grating structures." In: *Optics express* 18 (2010), pp. 366–380.

[219] Mark J Kerr, Andres Cuevas, and Patrick Campbell. "Limiting Efficiency of Crystalline Silicon Solar Cells Due to Coulomb-Enhanced Auger Recombination." In: *Progress in Photovoltaics: Research and Applications* 104 (2003), pp. 97–104.

[220] C Carlson and S. Hughes. "Disordered nanophotonic surfaces for enhanced light collection in semiconductor solar cells." In: *Journal of the Optical Society of America B* 35.5 (2018), pp. 1093–1104.

[221] E. D. Palik. *Handbook of optical constants of solids*. Academic Press, 1998.

[222] Nicklas Anttu. "Physics and design for 20 % and 25 % efficiency nanowire array solar cells." In: *Nanotechnology* 30 (2018), p. 7.

[223] S Mann et al. "Quantifying losses and thermodynamic limits in nanophotonic solar cells." In: *Nature nanotechnology* (2016).

[224] N Tajik et al. "Sulfur passivation and contact methods for GaAs nanowire solar cells." In: *Nanotechnology* 22.22 (2011).

[225] a. C. E. Chia and R R LaPierre. "Electrostatic model of radial pn junction nanowires." In: *Journal of Applied Physics* 114.7 (2013), p. 074317.

[226] Nicklas Anttu. "Shockley-queisser detailed balance efficiency limit for nanowire solar cells." In: *ACS Photonics* 2.3 (2015), pp. 446–453.

[227] Dick Van Dam et al. "Directional and Polarized Emission from Nanowire Arrays." In: *Nano Letters* 15.7 (2015), pp. 4557–4563.

[228] Sander A Mann et al. "Opportunities and Limitations for Nanophotonic Structures To Exceed the Shockley-Queisser Limit." In: *ACS Nano* 10 (2016), p. 8620.

List of Publications

- Nasim Tavakoli, Ilya Kolpakov, Jos Haverkort, Esther Alarcon-Llado, "Probing length-dependent absorption in vertically standing Nanowires with confocal fluorescence microscopy", *in preparation* (**Chapter 2**)

  Author contributions: N.T. performed the optical simulations, confocal measurements, data analysis and writing the manuscript. I.K. fabricated the NW samples with supervision of J.H.. N.T. and E.A.L. designed the experiments.

- Nasim Tavakoli, Wonjong Kim, Tom Veeken, Dominique Poorten, Lucas Güniat, Alok Rudra, Anna Fontcuberta i Morral, and Esther Alarcon-Llado. "Coloured and Semi-Transparent Nanowire-based Solar Cells for Building Integrated Photovoltaics".
  Preprint at http://arxiv.org/abs/2107.09465 (2021) (**Chapter 3**)

  Author contributions: N.T. conducted the optical simulations, data analysis and writing the manuscript. W.K., L.G., and A.R. grew the NW array samples at EPFL. N.T. and D.P. performed the PDMS embedding and lift-off. T.V. performed transmission measurements on NW-PDMS composites. N.T., E.A.L. and A.F.M. designed the experiments.

- Nasim Tavakoli, Richard J. Spalding, Alexander Lambertz, Pepijn Koppejan, Georgios Gkantzounis, Chenglong Wan, Ruslan Röhrich, Evgenia Kontoleta, A. Femius Koenderink, Riccardo Sapienza, Marian Florescu, and Esther Alarcon-Llado. "Over 65% sunlight absorption in a 1 μm Si slab with hyperuniform texture".
  Preprint at https://www.researchsquare.com/article/rs-69198/v1, DOI: 10.21203/rs.3.rs-69198/v1 (2020). (**Chapter 4**)

  Author contributions: R.J.S., G.G. C.W. and M.F. carried out the HUD optimisation and optical simulations. N.T. did the sample fabrication. N.T., E.K. and R. R. performed the optical characterisation and processed the experimental data. P.K. performed the PC1D simulations.

E.A.L., R.S., M.F. and A.F.K. were involved in planning and supervision of the work. All authors contributed to writing the manuscript.

- Nasim Tavakoli, and Esther Alarcon-Llado. "Combining 1D and 2D waveguiding in an ultrathin GaAs NW/Si tandem solar cell." Optics express 27, A909 (2019). (**Chapter 5**)

  Author contributions: N.T. performed the optical simulations and data analysis. E.A.L. directed the project. N.T. and E.A.L. wrote the manuscript.

Acknowledgment

First and foremost, I would like to thank my wonderful supervisor. Esther, I don't even know where to start and how to express my immense gratitude for having had you by my side in the past (almost) five years. You are not only a great scientist, but also a beautiful soul and an incredibly supportive and empathic leader. Thanks to you, I never felt alone in the past few years, even when I went through many different challenges. Your office door was always open to discuss scientific (or non-scientific) issues, and you were always available on zoom to help solve any problems (even when you were on holidays). Watching your great success in science while owning your femininity was incredibly inspiring to me as another woman in science, and observing the way you keep learning and growing alongside your team helped further develop the scientific spirit in me. You will always be a role model for me. Thank you for trusting me as one of the first members of your group, and thank you for all the scientific excitement and all the love you spread. I will keep all of our beautiful moments in my heart as I leave AMOLF, and I will always look back at them fondly. Next, I would like to thank Albert, my dear co-promoter. Albert, you are another perfect example of a brilliant scientific mind combined with a wonderfully kind and supportive soul. I feel extremely lucky to have you as my co-promoter and also as the leader of LMPV. You teach not only great science but also encourage team-spirit and friendship among all students and group leaders. The community culture that you established and maintained at LMPV (and nanophotonics) is unique and heart-warming. Thank you for showing us all how much more fulfilling it is to view one another as comrades to grow with instead of competitors to surpass. You are the shining soul of LMPV! I would also like to thank the other wonderful nanophotonics group leaders, Femius, Bruno, Erik, and Said. Femius, you are a wonderful teacher and a passionate scientist. Thank you for all the lively discussions at the colloquia and the poster sessions, and thank you for the great collaboration we had. Bruno, I admire your level of social activity, from twitter to sustainability activities. Thank you for setting such a good example for an active scientist. Erik, I learned a lot from you during nanophotonics colloquia and posters.

Thank you for your original and difficult questions, which always helped me look at the problem from a different perspective. Said, your Persian side shines through so much that we quickly connected after you joined AMOLF as a group leader. I will never forget the great fun of practicing Persian at the Language Café, dancing at Veldhoven and PhD parties, and our random encounters at AMOLF, which mostly led to deep conversations. Thank you for your openness and friendliness, and thank you for all the nice talks and good advice. And of course there are other group leaders at AMOLF, each with their own unique brilliant minds and fascinating research ideas. I would like to thank them all for making AMOLF so diverse yet harmonic. I would especially like to thank Bas, for combining art and science and turning AMOLF into a cool science museum on our Open Days, and Wim, for the cool and artistic science and his incredibly vibrant presence at AMOLF.

I would like to acknowledge Huib and Paula, directors of AMOLF, for taking such good care of our beloved scientific community. Especially in difficult times like Corona, maintaining our second home both safe and running has been a very big challenge that you overcame with grace. Thank you both for your love and dedication.

I would also like to thank the Doctorate Committee, prof. dr. H. Zhang, prof. dr. W.C. Sinke, prof. dr. E.C. Garnett, prof. dr. M.A. Loi, and prof. dr. A. Fontcuberta i Morral for accepting the invitation and for their time and effort to read this thesis in detail. I look forward to our scientific discussions.

Esther has an exceptional talent in choosing remarkable, talented people who are all unique in their different characteristics but all have one thing in common: They are all team-players. They are sociable, friendly, helpful and supportive. I enjoyed countless lunches, coffee breaks, outings, and meetings with these amazing people. Mark, my dear co-PhD, you were the only fixed member of 3DPV when I arrived, and I feel beyond lucky for having you as the person welcoming me into the group. Your help and support made it so much easier for me to land in my new position, and your kind and modest personality gave me space to be who I am. Thank you for being such a safe place for me at the beginning, and a great friend from then on. Thanks for all your typical sarcastic comments at the lunch breaks

and all the good questions and scientific inputs during the group meetings and discussions. Your easy-going attitude, when confronted with little conflicts, made the group dynamics chill and relaxed. Thanks for being the unique person that you are. Marco, your unique Italian/Columbian personality was a wonderful addition to the group. You are a wonderful scientist with an amazingly caring and loving heart. Thank you for having looked after everyone in the group at all times. For noticing when someone was silent for too long and asking a question directed to them to make sure the group is always inclusive. Thank you for all the funny stories you told us about your parents and little Luca, and thank you for all the amusing discussions you had with Mark at every single lunch break. You are always a 3DPV member in my mind. Yorick, I am still in shock from that day you broke the speed limit in hyper bowling! And I still don't get why you were the only other 3DPV member at many parties I was invited to. But you are not only sporty and fun. You are a beautiful combination of smart, humble, friendly and helpful too. And you have been a valuable member of our group. Thank you for always volunteering to take care of anything that comes up and to always be there to help everyone. I will miss bumping into you on a daily basis. Daphne, your cheerfulness, transparency in how you feel, proactivity, and ambition is very refreshing to be around. I really enjoyed hanging out and talking to you in my last months at AMOLF! we skipped past the small-talk and were already talking about personal experiences the first time we had dinner together. I hope you always stay the unique person that you are! Jelena, your enthusiasm and dedication, together with your fun and kind personality, was a wonderful addition to our group. Carles, you stayed only for few months after I joined in the group but that was more than enough time for us to become great friends. Your Catalan warmth helped me feel at home right after I moved from Spain to the Netherlands. Ilya, your calm way of telling spooky stories (and your cute voluminous curly hair) added a special flavour to our group's dynamics. Thank you for being so passionate and responsible, this made our collaboration experience very enjoyable. Also, thank you for sending me the friendliest samples I've ever received: Ones that said hi to me under SEM. Laura, I remember right after my talk at AMOLF's interview day, you came to me to make sure I'm not too stressed, and that is my first memory of your super friendly vibe. Thank you for all the talking and laughing and dancing (under the rain) together, which I always

look back at with a big smile. Rosa R, apart from all the fun moments at AMOLF, it was amazing to go to a contemporary dance course with you. Thank you for all the lightness and energy you radiate. Suzan, your super chill way of going through life was very interesting to observe. Thank you for the time we spent together, and for adding Luna to my life. We will always be connected through her. I would also like to thank all the Bachelor and Master students for whom I was the daily supervisor. Alexis, Dominique, Pepijn, and Alex, it was an absolute pleasure to work with you all. Alexis, thank you for being such a wonderful first student that I supervised during my PhD. Dominique, your patience and persistence through all the membrane-breakings was inspiring, and your skills in data and sample management were the basis for the BIPV paper. Thank you for all the hard work and also the sweet friendship we built over those months. Pepijn, your positive vibe and hard work was a great combination that made our pipet electrochemistry sessions much more fun. Thank you for your persistence and your always-present smile. Alex, you must be some kind of super-human! It always amazes me to see how much passion and excitement and care and friendliness and fun and knowledge and hard work can fit into a single human being. Working with you was a true pleasure. Thank you for continuing the beautiful HUD project and for bringing large area ultrathin HUD-patterned PV into life. I'm very happy you are staying at AMOLF and I will get to hang out with you even more. Juliane, although we mostly interacted over zoom, I still enjoyed your cheerful vibe, brilliant jokes, and beautiful scientific mind. I would also like to thank the other members of 3DPV throughout these years, Giovanni, Jose, Rosa, Merlinde, Jim, Jos, Blaise, and Mees, for the good quality scientific interactions, fantastic vibe, and positive energy of our beautiful little group.

AMOLF is this delightful science heaven where many amazing people are busy keeping it up and running. It is because of these people that I never had to worry about anything beyond the usual challenges of my projects. I would like to thank the admirable technical staff I had the pleasure of working together with. Dion, thank you for being the technical genius that you are, coming up with all sorts of simple to complicated solutions to any problem we brought to you. Daniel, thank you for joining our group with so much enthusiasm, actively participating during the group meetings, and for being there to help all the time. Starting a new job during Covid

was tough, but you managed to quickly be part of the 3DPV family and excel at your job. Marko, we don't seem that group-connected on paper, but I cannot count how many hundred times I called you with different technical issues. And all those times, you picked up the phone with your typical -sarcastic but kind- tone asking me what I need this time. And then you showed up to solve my problem a few minutes later. Thank you for all your help and all the brightness you bring into AMOLF. It's always great to bump into you at the coffee machine, or in Flevopark together with Leo. Bob and Dimitry, you two have been the joyful soul of the clean-room since the day I remember. Bob, thank you for the incredibly cheerful yet professional and high-quality trainings. There were times that I called you 5 times a day to check every detail of my fabrications with you, and you were always there to help. You are a delight to be around and so much fun to hang out with (the funny video of Luna styling your hair still cracks me up). Thank you for all your guidance inside the clean-room and for the lovely friendship outside. Dimitry, you fabricated my first hyperuniform structures with such perfection that I still look up to you as "The Fabrication Master"! Thank you for sharing your knowledge and time with me, and thank you for turning the clean-room into a little party anytime you had the chance to. Igor, from the moment you joined the clean-room, it was as if you always belonged to this joyful and knowledgeable family. And you settled in very quickly too. Only a couple of weeks after your arrival you were giving SEM training to the newcomers. Thank you for your calm and helpful presence. Hans, Marc, Hinco, Niels, Wessel, and other technical support staff thank you for keeping AMOLF up and running with such enthusiasm.

The support at AMOLF is not limited to the technical staff. There are tens of people to whom I owe the quality of my daily life at AMOLF. Thank you Juliette and Ad, for your radiant smile and warm welcome every morning and your kindness in the many email interactions we had throughout these years. Thank you, Wouter, for the incredible support you provided me, especially during Covid. Thank you for all the meetings and calls, for thinking together with me how to best solve whatever issue I was facing at that time, and for making them happen. You make a wonderful head of HR. Thank you, Reshma and Linda, for your understanding and for helping me with housing. Thank you, Olivier and Sharlene, for waiting long on the IND line for me to find answers to the questions we had. Thank

you, Petra, for your endless passion for science and communication, and for all the nice and open conversations we had. ICT was another department I was blessed to receive support from. Thank you, Carl, for your constant care and support for my supercomputer issues. Wiebe, thank you for your kind and welcoming presence every time I entered ICT department, for your warm smile, and for your friendly support. Rutger, thank you for your patience and skilled presence at ICT. I would also like to thank the one and only Clyde. Your unique character is missed whenever you are not around. Thank you for taking care of many things around AMOLF with a big smile and bright presence. Henk-Jan, Iliya, Grace, Erny, Jeroen, Angela, Sebastiaan, Ilja, Henriëtte, Teressa, Karelia and other support staff, thank you all, for making my time at AMOLF so much more enjoyable with your presence.

Scientific collaborations with interesting people with bright minds and different points of view is one of the most precious aspects of science which I admire. During my PhD I had the chance to work with many of these great people. Ruslan and Femius, thank you for your valuable time, knowledge, trainings and for the interesting discussions we had. Jenny, the time spent in the lab with you was both very fruitful and fun. Marian and Riccardo, thank you for your passion and dedication, your valuable contributions, and everything that I learned from you. Anna F., thank you for sharing your expertise, for the wonderful discussions, and for your joyful presence at conferences and video calls. Tom, thank you for sharing your time and expertise with me. Ilya, thank you for your professional responsibility and great samples. Alex, Stefan and Jelena, thank you for your time, passion, valuable knowledge and dedication to make HUD solar cells happen!

My dear paranymphs, Lucie and Susan, you know how much your wonderful friendship means to me. We have been by each other's sides through so much already, and I cannot imagine a better army to go to my defense with. I feel extremely honoured to have you two by my side on one of the most important days of my life. Lucie, you are a ray of sunshine radiating through AMOLF. I still remember how much I hoped to get closer to you the very first times we met. I mean, anyone would. Your beautiful, playful, and loving soul shines through your smiley eyes and your vibrant dance very quickly. But I also remember how much I was in awe of your super mature arguments and advice despite your young age. And you

have only amazed me more since then. You are a blessing in the lives of your friends and colleagues. Thank you for your beautiful friendship, for your loving presence all these years, and for being a pillar of "Home" for me, here in Amsterdam. Also, you're my favourite scientist. Susan, you are a strong and independent sweetheart. I remember how your direct way of speaking and joking intimidated me the first few times that I saw you. Little by little, however, I got to see the soft sparkly side of you. And how shiny and vibrant and sweet and cuddly and reliable and loving it was (and then I grew to appreciate –and even miss- your brutally honest jokes too). We found similarities that we couldn't find at first sight. And we influenced each other a bit too: I made you a little softer (when you needed to feel more), and you made me a little stronger (when I needed to go to war). You are not only a close friend of mine anymore; you are family to me. Thank you for your loving friendship, reliable strength, and damn-funny brutal jokes. You are fabulous!

AMOLF already did a fantastic job in gathering so many exciting people with unique, beautiful minds and souls in one place. All I had to do was invite them into my life, and so many of them accepted my humble invitation. And how blessed I feel for that. Verena, the joy I feel every time I am about to meet you is difficult to describe. There is a glowing lightness to your presence and the way you wander around in life. I admire how much you care about your principles and how open you are, at the same time, to different ideas and lifestyles. You, together with David, Clara, and now Aaron became part of my family. Thank you for the wonderful person that you are, and for being such a big part of my life. Lukas, what a beautiful journey we had! Being friends for many years already and yet only getting to really know each other during Covid. Having you as a caring neighbour, with your aromatic coffee and your freshly-made bread, made many of those strange Covid days not only bearable but enjoyable. Without your supportive and caring light my thesis-writing time would have been much darker than it was. Thank you for being there for me, and thank you for letting me see the colourful and lively soul that you are. Robin, who would have thought your one-time co-working invitation would get us here? You are one of my closest friends in the Netherlands now, and I couldn't be happier about that. I enjoyed getting to know you better, one dinner at a time (even if we had to rush out of your house to make it home before the curfews). Not only do I admire your easy-going

character, but I also appreciate your playful yet somehow innocent attitude. Thank you for the wonderful vegetarian dinners, 4-person Covid parties, your absolutely incredible pictures of the animals and their stories, and your caring and vibrant friendship. Jenny, I wish I met you regularly for dinner long before I eventually did. You were the most popular person at AMOLF since I entered that building. Everyone was in love with you and brightened up when talking about you. And oh, how right they were! You have the kindest heart I've ever felt and have the most beautiful and loud laughter anyone can imagine. You are light. Thank you for sharing your rays with us all. Magda, your warm and kind smile got my heart bound to you since the moment we first met. Even though we couldn't manage to meet as often as we would like to, I am still happy and grateful for our little dinners and short but precious interactions at AMOLF, and of course, the few beautiful yoga sessions that we shared. Your humble excellence in science still amazes me. Thank you for the beautiful human that you are. Giorgio, you are such a sweetheart. Your vibrant presence is enough for people at any party or gathering to become smiley and cheerful. No matter how busy you get, it still warms my heart that you live in Amsterdam, and I get to see you sometimes. Thanks for all the good memories, coffee, laughter, dance, hugs, and great friendship. Agustin, you feel like a soft-hearted and strong mountain to me. You are grounded and peaceful, no matter how strong the storm is. Thank you for your calm presence, your inviting hugs, your exciting parties, and your lovely friendship. Carolyn, my first memories of you are of you dancing and running around at AMOLF at different parties. That, alongside you being a great scientist, amazing cook, professional athlete, and the-cutest-house designer that I met, is what made you win "the perfect human" trophy in my mind. When I got to know you better, however, I could also see the vulnerabilities and imperfections which made you even more beautiful of a human and made me appreciate you even more. Tom, did you know that you were the first person outside of my group who actively welcomed me at AMOLF? You sat next to me at the Thursday coffee break, introduced yourself, and welcomed me while translating all of the Dutch parts of Huib's speech. Since then you have been a big part of my AMOLF life. You are a great friend and super responsible and helpful co-worker. I don't really know how you manage to find time to do the hundred things that you do, and be proficient at them all! We have hung out a lot and talked a

lot about everything all these years, but you still keep surprising me with new aspects of your personality. It's been a true pleasure to collaborate with you and to be your friend, and I feel grateful that AMOLF introduced you to me. I hope we stay in contact for many more years to come. Andrea, it was always nice to be around you and your warm and fun southern Italian energy. Dancing at the parties, Gangnam style trainings, directing Verena's movie, and little gossips here and there. Thanks for all the fun you spread. Chris, hanging out with you is always fun. You are a great pizza-designer, boulder-er, and Luna-carer. Thanks for the good vibe you always bring with you anywhere you go. Rene, crossing paths with you in the clean-room, at the coffee corner, or at Duwo was always enjoyable. Thank you for your enthusiasm about everything, for taking me along to Delft to get my samples ready, and for taking care of Luna anytime I suddenly needed to disappear. Ruslan, your unique combination of smart, kind, smiley, a bit shy but self-confident is very memorable. It was a lot of fun seeing you at the coffee corner (and in your office, every time I needed help with something). Your physics knowledge and coding skills, together with your fast way of solving problems were inspiring to witness. Thank you for all the fun memories, and the joy of collaborating with you. Mareike, your super warm smile that extends from your lips to your eyes and your whole face is heart-warming. It is always a joy to see you either at AMOLF or somehow inside or next to Duwo's elevator. We tried to make intentional plans which never worked out. Let's keep trying though! Marloes, your warm attitude and your fashionable style are the first things that come to my mind about you, and bring a smile to my face. I am happy you decided to stay for your PhD to keep sharing your sparkly vibe and loving presence with us at AMOLF. Mathijs, your very big smile was a match to mine at AMOLF. It was great to get to see you more and learn about your broad range of interests, from sports to improvisation acting. Your positive energy is contagious and inspiring. Bart, you were the most passionate and intelligent Persian language student I've ever had! (ok, I didn't have many, but you would have been *the number one* even if I had). Your Dutch olleke bolleke written in Farsi letters blew my mind and filled my heart with warmth. You also showed me cooking together over skype is possible and actually fun. Thank you for your beautiful mind and kind heart. Julia, your bright and vibrant character always puts me in a good mood, and the great scientific discussions we had were exciting and thought-provoking.

Thanks for spreading your energy and for the cheerful pictures and videos from your little chickens during Covid. Kevin, our friendship extended from AMOLF coffee corner to occasional yet very enjoyable dinners with Magda and Verena, and I'm very happy about that. Thank you for your kind heart (and harsh humor)! Christian D., hanging out with you, no matter at the coffee corner, borrels, random daily encounters or the poster sessions, was always delightful. Thank you for your sweet presence in my AMOLF daily life. Isabelle, thank you for always being so kind and supportive, especially toward other women. Your great strength together with your beautiful vulnerability was very inspiring for me to witness.

Office 2.54 has been a second home within AMOLF for me. I've had highs and lows, laughters and tears, which were shared with many amazing people who shared that space with me. Ilse and Sylvianne, with your presence the office became more vibrant and alive. Thank you for your bright energy and the sweetest spontaneous "26th" birthday we celebrated together. Ilse, I'll never forget the anticipation of getting into my office in the morning to find a letter on my monitor about fun facts of that day, for many weeks in a row. Even though you were not the best "loser" in our early morning competition, I still have all your letters, and I remember all our open and deep conversations. You live in your dream city now, but still every time we meet it feels like nothing has changed and it's as if we still see each other every day. Anastasia, I still remember the first day we said hi and introduced ourselves. The spark between us was instant. Your smile was as big as mine, and your passion for dance reminded me of mine. Thank you for taking me to dance events with you and giving me the courage to try dancing again (which, in the end, gave me the courage to join the Persian dance group in Berlin's cultural carnival). With you, I feel brave and free. Thank you for the unforgettable days in France with your beautiful family and friends, and thank you for your pure, supportive, and elevating friendship. Joost, you occupied our snack desk but quickly turned our office into "the fun office". Your passion and dedication, both in your scientific and little office projects (like the wheel of fortune), are very inspiring. Thank you for being such a great friend, for inviting me for the lovely Christmas time with your sweet family, and for being so exceptionally good at choosing the perfect gifts! You are missed in Amsterdam. Arno, you are so uniquely talented and kind. It was an honour, and loads of fun, to share an office with you. Thank you for lending

me all sorts of cables, for spontaneously thinking with me to find solutions to random problems, and for trying to coach the untalented me to pick simple locks. Eitan, my dear work friend, our similar cultural background (although difficult to believe) and matching sense of humour made it easy to quickly become (work)friends. However, various difficulties and on top of all Corona made your presence incredibly valuable to me. Seeing you in the office on AMOLF days was the best welcome gift I could imagine. Thank you for your super genuine character, which stems from your unique brutal honesty. And thank you for your hugs, support, and kind words when I needed them most. I am glad we upgraded to actual friends, which hopefully means I will always have you there to challenge me and receive my mean –yet kind- jokes with grace. I would also like to thank the rest of my officemates, Sevda, Tianyi, Linde, Olga, and Cristina. You all made my AMOLF home very warm and cosy.

During my first year at AMOLF, I joined "Quantsol" summer school in Austria. During this great time, I did not only grow scientifically but made lasting friendships. Verena, sharing a room for five nights and talking so much about our lives started our wonderful friendship. Rowshanak, meeting you at Quantsol was such an unexpected blessing. We connected so quickly that people thought we knew each other from before. What I didn't expect back then was to meet you again at NanoGe in Spain and spend the whole conference time with you and your crew. Your exceptional openness is so inspiring. Thank you for inviting me to Berlin to stay with you, and dance with you, and become close friends with you. I cherish our friendship and hope to be able to see you again very soon.

Language Café meant a lot to me. It was the first time I decided to be proactive and make a change when I saw the potential for improvement in my environment. And thanks to all the supporting people around me, it became possible. Thank you Floortje, for giving me the advice to find a partner to do this together, otherwise it would not have happened. Thank you, Hans, for recognising the energy and passion I put into this project and encouraging me multiple times to keep going when it wasn't going smoothly. And of course, thank you, Lukas, for saying yes to organising our beloved Language Café with me. Without your help and your unbeatable talent for planning and organising, it wouldn't have been possible for me to see the project in my head come to life. And thank you, Paula, for

recognising the effort of keeping the Language Café alive for 10 months at Sinterklaas day.

Another great extra-curriculum activity was joining the International Committee of the Works Council. Thank you Ramon and Jesse, for initiating the presence of international employees and for cultivating its potential for the first time. Thank you, Paula, and other Works council members, for changing the language of the meeting to English so that we could follow the discussions. I was very happy to, alongside Lucie and Harshal, help bridge the gap between international employees' needs and the management team of AMOLF.

AMOLF coffee breaks in the morning and after lunch were great opportunities to casually meet with numerous nice people with many of whom I share a lot of wonderful moments and memories outside of AMOLF. Hugo, Annemarie, Kelly, Hongyu, Harshal, Agata, Christina, Giada, Sophie, Sven, Ariane, Nick, Loreta, Dario, Cesare, Yuval, Benjamin, Moritz, Eliane, Luuk, Roel, Mario, Matthias, Nika, Imme, Jente, Xuan, Federica, and other lovely AMOLFers, thank you for being a big part of my day-to-day happiness in the past few years.

During my journey in Amsterdam I have also had many Iranian companions, for whom I feel blessed. Especially during the past two years when Covid kept me away from my family, many of you have been a trace of home for me: Speaking in Farsi, eating Iranian treats, dancing Iranian moves to Iranian music, and feeling closer to my culture. Parisa, your friendship was the first gift I got from AMOLF, and how precious it was to me. Your bright presence, your openness to talk about everything from fun and happiness to daily struggles, your warm hugs, and your kind support helped me immensely when I needed them most. You were home to me, when home was far out of my reach. Thank you for everything, for our beautiful friendship, for your uplifting and strong attitude, for always fighting for your rights and encourage me to do the same, for being so unapologetically you. You are such a beautiful human being, and I feel blessed to have you by my side and in my heart. Maryam, it's funny how we first participated in one of the Persian book-club evenings and then went for drinks, which led to us planning to go to the gym together for a while, which led to us traveling together! You are a great friend with a solid

sense of fashion, and the best travel buddy! Behnaz, I am very happy you reached out to me when you did, and I'm very happy we talked so much and got closer right away. You are strong, intelligent, ambitious, brave, so kind, and very real. I am impressed and very proud of you for the intense life that you're leading. You are wonderful! Fahimeh, your presence always brings peace to my heart and a smile to my face. You are undoubtedly one of the kindest and most caring people I have met, but on top of that, you are one of the strongest ones too. Your courage in making bold decisions and your strength in always showing up for yourself, your children, your family, and your friends is truly an inspiration. Najmeh, you are a great physicist and a beautiful woman, inside and out. You are brave and strong, and I am very proud of you for who you are and for who you are becoming. Samira, you were always bright and beautiful, but your evolution into this fierce woman that you're becoming is extra inspiring. I feel honoured to be your friend and witness your wonderful journey. You are amazing! Alireza, thank you for your friendship and support, for great Iranian dishes (and not-so-great Iranian shows), and for your kind hospitality, both when I was visiting Iran and when you moved to the Netherlands. Sadaf, thank you for starting the dance group, and for encouraging self-care among us all. Hoda, thank you for the wonderful time that we had and your kind and beautiful heart. Mahsa, you are a loving sister to me. I feel calm, at ease, understood, and taken care of when I'm with you. I am beyond happy to have you, Mohammad, Sahand, and your little one as my family here. I would also like to thank Marzieh F. and Hamid, Marjaneh and Sohrab, Aylar, Azad, Maziar, Sara and Leila, Faezeh, Marzi, and all the other wonderful Iranian friends I made during these years for their presence. And last but not least, thank you Mehdi, for everything that we shared together. For all the love and support, and everything that I learned from you. No matter what, you will always be a part of who I am, and I feel forever grateful for having had you in my life.

I have had teachers in my youth who have sparked the curiosity and passion for science in my mind. First, I want to thank my high school Physics teacher, Mr. Reza Zahabi, who ignited the love for Physics inside me. I would also like to thank my first-grade teacher, Mrs. Rezadoost, from whom I got my enthusiasm for reading and being friends with books, and also acknowledge Mrs. Asgari, who helped me feel at home at high school. Next, I would like to thank my university professors, Dr. Ghafouri, Dr.

Sepehri, Dr. Khosravi, Dr. Sepanji, and Mrs. Moini for passing on their knowledge, passion, and dedication.

Besides Amsterdam, I have lived in Tehran and Spain for years, and in Germany and Canada for a few months each. In each of these places I met amazing people and learned a lot from every single one of them. These beautiful people influenced me in different ways, which contributed to who I am today. I would like to thank them all, and even though I won't be able to name them all here, I would like to name a few: Newsha, you were my first ever close friend, and you will always have a special place in my heart. Our little adventures in school are my best memories from our uptight school time. Shaghayegh, with you I practiced to talk openly about everything and listen well. Thank you for our lovely friendship. Samin, with you I learned how to be so close to someone despite difference in opinions. We grew a lot together, and you will always be part of who I am. Saleh, you are one of those friends who I see not that often but I know will always be there. It's easy to talk to you, to laugh and joke with you, to travel with you, to have adventures with you, and to see you after a year and still feel the same connection. Salar, Farhad, Houman, Imen, Javaneh, Anoosheh, Mehrnoosh, and my other friends and classmates at Shahid Beheshti, thank you for all the good times, sad times, adventures, and everything we learned together. Without you I wouldn't be the person I am today. Ava, Saghi, Saleh, Alireza, Sanaz, Zahra Gh., Sadegh, Amir, Soran, Nikoo, Zahra B., Amirhossein, and all the other "Goorkhooneh" friends, thank you for all the fun chats, creative stories we made, games we played, and friendships we planted and nurtured together. Amin Y., thank you for the time in Vancouver. Thanks for showing us around and for sharing good food and fun experiences with us. Quim, Bruno, Victor, Sasha, Maria, Samaneh, Ehsan, and all the other lovely friends I made in Spain. I carry you in my heart everywhere I go, and I hope to meet you again soon somewhere in the world. Ali, Jonas, Daniel, Martin, and other nice friends I met in Germany, thank you for your hospitality and the fun time together.

Life in Amsterdam gave me another beautiful gift, and it was meeting my wonderful therapist. I would like to thank Rob, whose guidance and care changed my life, helped me become the person that I love more, and turned me into an advocate of "therapy is beneficial for absolutely

everyone"! Rob, thanks for deciding to become a therapist at the age of 50. Your beautiful soul and immense empathy make me feel more connected to the world as a whole. You've been an absolute blessing in my life, and you will always be loved and cherished in my heart. I would also like to thank and acknowledge my amazing career coach, Chiat, whose presence and help during Covid time was invaluable. Chiat, not only did you guide me through the dark days of Covid, but you also helped me find my passion for art and psychology again. I feel more alive and energised, thank you for all that.

Apart from wonderful friends and great colleagues, I would like to thank my family who keeps my heart warm and happy, even with the distance. First, my heart goes to my grandparents who may not be here with me today, but have always been present in my heart. Mamani, I wish I could enthusiastically pass by your little room to show you the first book I wrote. Your memories and your love will live inside me forever. And to the rest of my lovely family, who is always in my mind and my heart: My aunts and uncles, khaleh Shahin and Amu Bahman, Dayi Parviz and Maria, khaleh Mahin and Amu Hamid, khaleh Nahid and Amu Davood, Amme Gohar and Amme Nasrin, Amu Khalil and Amu Javad, Amme Pari, Amme Poori and Amme A'zam, and my lovely cousins, Termeh and Arman, Nazi, Reza and Maryam, Alireza and Mali, Taraneh, Elnaz and Ehsan, Delaram and Danial, Kati and Siamak, Farinaz and Houman, and my sweet little ones Parsa, Maryam, Hedyeh, Diba, Nafas, Saina and Raya. I would also like to acknowledge some wonderful friends of my family who have been there all my life and feel like family too. Dear Monir joon and Dr. Ghaheri, Shadi and Farid, Zari joon, mohandes Saad, Sayeh and Nasim, Shahla joon and mohandes Maraghechi, Siavash and Maryam, thank you for your constant love and warm presence in my life.

In the end, I would like to thank and acknowledge my beautiful and loving parents and my wonderful little sister, who mean the world to me. There is no one in the world that I would rather have sitting in the first row when I defend my thesis and (hopefully) celebrating this important milestone with me. Shabnami, every single day I ask myself how on earth did I get so lucky to have the most beautiful and radiant soul I've ever met as my little sister? The intensity of love I feel for you is difficult to describe. Thank you for spreading your inner light in our little home (in

the shape of constant hugs and keeping less than 1 meter distance) since the day you were born. Thank you for being such an amazing listener, the most fun partner in crime, and the most supportive and non-judgemental friend to me. Thank you for all the times you cheered with me when I felt on top of the world and to never giving up on me when I hit rock bottom. And thank you for dedicating all the time and energy it took for us to stay this close and connected despite the physical distance between us over the past ten years. This beautiful garden that we planted and nurtured together is a proof of real and healthy love to me, and keeps me motivated on days I lose faith in the world. Thank you for all of this, and many more gifts that you give me every day. Love you the most! Maman joon, Baba joon, you have been there for me every step of the way, every single day, since the day I was born. Mamani, I never forget you being there with me with your support, your midnight homemade fries when I was studying until late, and your freshly brewed tea and nice quick breakfast in the morning while I was running out the door to get to school or university on time. Babayi, I always remember the many times that I came to you with my school questions and you encouraged me to learn how to think for myself instead of how to take the taught path of solving single problems. Mamani, not only have I learned to be strong and fierce and ambitious and loving and caring from you, but you have also planted the love for art in me. Babayi, I got my passion for science, my passion for reading, and my passion for nature from you. Thank you for all those times you told me stories from your university days, from your book clubs and discussions, and showing me every tree, every flower, and every plant that you knew by heart during our hikes. My loves, a huge part of who I am comes from you, and how honoured and happy I am to have you as my parents. Thank you for everything. You are wonderful!